Universitat Autònoma
de Barcelona

Programa de Doctorado en Cirugía y Ciencias Morfológicas
Departamento de Cirugía
Facultad de Medicina

Multiplex Optical Detection System for Prosthetic Joint Infection Diagnosis

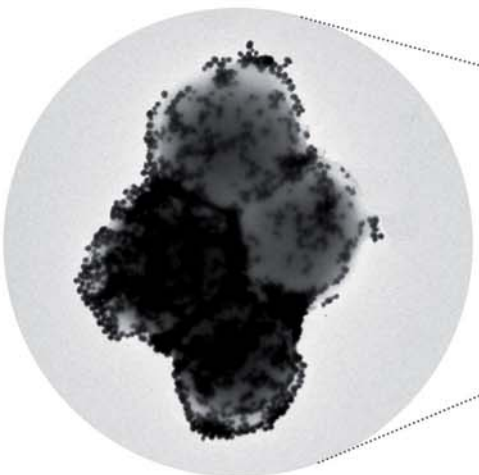

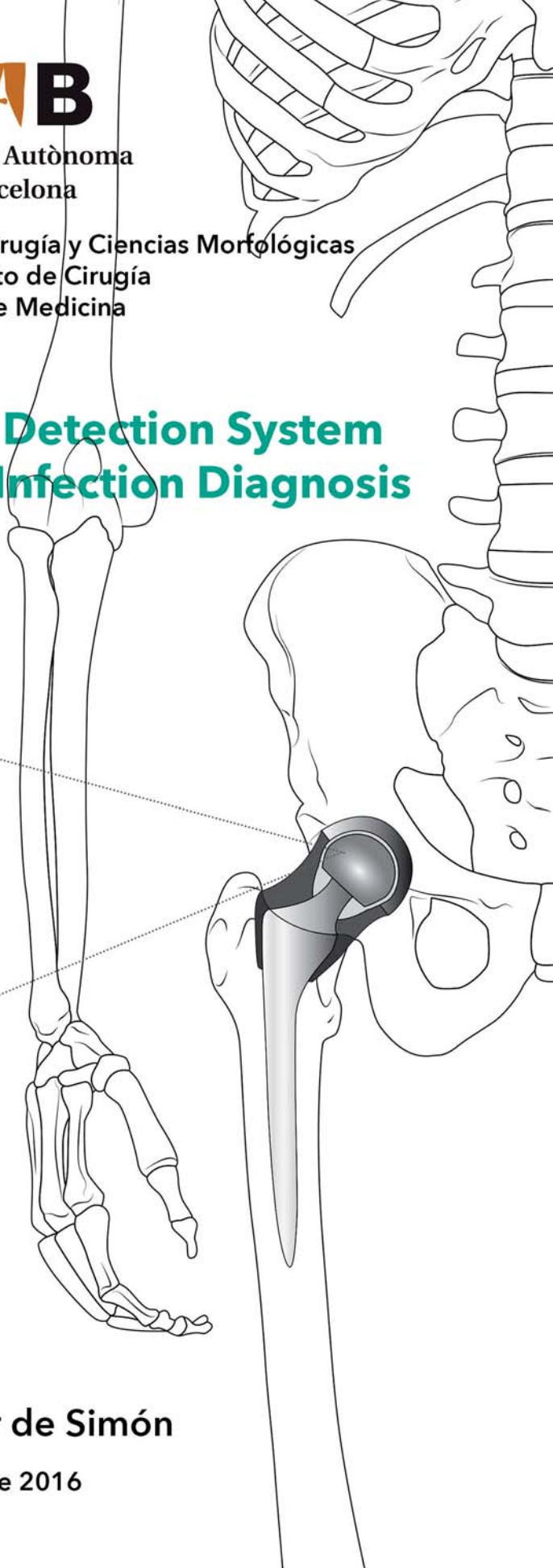

Bernat Mir de Simón

Octubre 2016

5 SERS Optimization using Polystyrene Beads as a Bacteria Model: The effect of Material and Nanoparticle size

5.1 Introduction

Almost 40 years after the initial discovery of the SERS phenomenon,[199] spectacular advances in the development of rationally designed metallic substrates with uniform, reproducible and optimized plasmonic response[200] have played a major role in the final translation of the analytical potential of SERS to biomedical applications.[21,22,143–145] Regarding the last, infections are of mounting medical and public concern and SERS encoded nanoparticles offer a ground-breaking advance in bacterial therapy and research. That advance is due to the substantial improvement with respect to the current methods for microorganism detection which suffer from intrinsic limitations related to selectivity, sensitivity, time-consuming procedures and technological shortcomings. The final aim of this thesis is the design of a device for multiplex detection of microorganisms in biological fluids for PJI diagnosis. For this purpose, different batches of plasmonic particles will be labelled. Each of them will have a different Raman reporter (characterized by its unique spectroscopic fingerprint and high Raman cross-section, see section 4) and then functionalized with specific bioreceptor yielding final SERS-encoded particles (or SERS-tags).[69] These bioreceptors (i.e., antibodies) will induce an specific agglutination of the SERS tags on the target microorganism membrane producing a drastic increase in the detected SERS signal due to the formation of optical hot-spots.

In order to achieve this goal and to further select the best nanomaterial and configuration, in this section polystyrene beads (PS) were used to emulate bacteria when the SERS tags agglutinate on the microorganism membrane. To this end, 3 μm diameter PS were homogenously coated with plasmonic nanoparticles. PS of 3 μm diameter were chosen because their size are similar to that of bacteria. These hybrid materials act as robust microscopic carriers of large ensembles of interparticle hot-spots concentrated in their external shell. The tens of thousands of nanoparticles anchored to the polymeric surface provide, in addition to high SERS activity via interparticle coupling, a highly averaged plasmonic response that

ensures great homogeneity within bead-to-bead Raman signal enhancing.[201–203] Thus, average SERS measurements can be performed at a very low bead concentration in suspension,[204] and single-bead analysis on a solid surface (micro set-up) is very straightforward and simple as the beads are plainly visible with a 50× objective. For these reasons, PS@NPs assembled nanostructures are the perfect tool to be used as a bacteria model. Besides, it is important to stress the extreme experimental flexibility offered by these supports. In fact, their intrinsic resistance against aggregation allows for the desired manipulations (i.e. centrifugations, redispersions, surface functionalization, changes in ionic strengths as well as solvents etc.) with no risk of perturbation of their SERS response.[201,204,205] On the other hand, as introduced in section 4, silica coating can be grown as an additional synthetic step on SERS-encoded NPs to further improve the colloidal stability for long periods of time and prevent the generation of hot-spots. However, PS@NPs assembled nanostructures take advantage of interparticle hot-spots concentrated in their external shell that produce strong SERS response and allow for single-bead analysis. Hence, silica shell on NPs is not the best option for the study of these types of nanostructures and therefore for the bacteria model.

Herein, the correlation between the size of quasi-spherical Au and Ag nanoparticle in suspension and the final optical property of their corresponding assemblies onto 3 μm polystyrene (PS) beads is systematically investigated. Colloids were synthesized via standard wet chemical methods using citrate as a stabilizing/reducing agent to yield nanoparticles with a similar surface chemistry (surface properties largely determine the adhesion of the nanoparticles onto the beads as well as the affinity of analytes for silver/gold). The SERS activity of each material was characterized by using thiophenol as a Raman label and some of the most common excitation wavelengths used nowadays in SERS spectroscopy (532 nm, 633 nm and 785 nm). The experimental results indicate that the size and composition of nanoparticles play a key role in tuning the SERS efficiency of the hybrid material at a given excitation wavelength. This provides valuable information for the selection of the appropriate SERS tags for the identification and quantification of bacteria in biological fluids.

5.2 Experimental section

5.2.1 Materials and methods

Silver nitrate (99.99%, $AgNO_3$), sodium chloride (≥99.99%, NaCl), trisodium citrate dehydrated (≥99.5 %, $C_6H_5Na_3O_7{\cdot}2H_2O$), L-ascorbic acid (≥99.0%, AA), magnesium sulfate (≥99.0%, $MgSO_4$), ethanol (99.5%, EtOH), benzenethiol (97%, BT), polystyrene beads (3 μm diameter, PS), tween 20 (≥99.5%, Tween® 20), Gold(III) chloride trihydrate (99.9 %, $HAuCl_4{\cdot}3H_2O$), polystyrenesulfonate (≥99.0%, MW = 1000000, PSS) and polyethylenimine branched (≥99.5%, Mw = 25000, PEI) were purchased from Sigma-Aldrich. All reactants were used without further purification. MilliQ water (18 MΩ cm^{-1}) was used in all aqueous solutions, and all the glassware and magnetic stirrers were cleaned with aqua regia and with a potassium hydroxide solution in isopropanol/water before all the experiments.

5.2.2 Synthesis of silver spherical nanoparticles of different sizes

To synthesize spherical-like silver nanoparticles (Ag NPs) with average diameters in the 40 to 120 nm range, a modified protocol based on the combination of previously reported approaches was used.[129,181,206] Briefly, 250 mL of Milli Q water were heated under vigorous stirring. A condenser was used to prevent solvent evaporation. Adequate amounts of aqueous solutions of $C_6H_5Na_3O_7{\cdot}2H_2O$ (0.1 M) and ascorbic acid (0.1 M) were consecutively added to the boiling water. After 1 minute, an aqueous solution of $AgNO_3$ (0.1 M) was injected into the reaction vessel under vigorous stirring. In some cases $MgSO_4$ was also used, and the $AgNO_3$ and the $MgSO_4$ aliquots were first premixed (stock solutions of $AgNO_3$ 0.1 M and $MgSO_4$ 0.1 M) and incubated at room temperature for 5 min before injection. The color of the solution quickly changed from colorless to yellow and gradually changed into orange or pale green depending on the nanoparticle size. Boiling was continued for 1 h under stirring to ensure the completeness of the reaction. The size of the Ag nanoparticles was

controlled by adjusting the concentrations of the different reactants. As a general trend, the size of Ag NPs increases by adding $MgSO_4$ and increasing its concentration. A similar trend is also observed when the ascorbic acid or the $AgNO_3$ were increased. Table 2 describes the concrete amount of reactants used in each synthesis whereas Figure 34 illustrates the histogram of Ag nanoparticle size distribution and representative TEM images of the dried colloids.

NP Diameter (nm)	39.3 ±6.0	48.9 ±8.7	55.6 ±4.6	70.4 ±7.6	92.5 ±7.7	121.4 ±17.9
H_2O (mL)	250	250	250	250	250	250
$C_6H_5Na_3O_7 \cdot 2H_2O$ 0.1 M (mL)	2.27	1.70	1.70	1.70	1.70	1.70
AA 0.1 M (mL)	0.249	0.249	0.249	0.249	0.275	0.30
$AgNO_3$ 0.1 M (µL)	744	744	496	496	2770	2900
$MgSO_4$ 0.1 M (µL)	-------	------	392	558	------	------
λ_{max} (nm)	400	410	432	440	449	498

Table 2. Detailed amounts of reactants used for each Ag colloids synthesis and the corresponding surface plasmon resonance maxima.

5.2.3 Synthesis of gold spherical nanoparticles of different sizes

The Au NPs were synthesized by a modification of the procedure shown in section 4.2.2. However, for this experiments the Au NPs were provided by the group of Prof. Victor Puntes. This strategy is shown as follows:

Small gold nanoparticles (Au NPs) of ~15 nm diameter were prepared according to the Turkevich-Frens preparation method.[76,120] Briefly, $HAuCl_4$ trihydrate (15 mg) was dissolved in milli-Q water (150 mL) and heated to boiling. An aqueous solution of $C_6H_5Na_3O_7 \cdot 2H_2O$ (1 %, 4.5 mL), previously warmed to ca. 70-75 °C was then quickly added, and the mixture was

refluxed for a further 30 minutes until the solution turned ruby red in color. The solution was then allowed to cool to room temperature under vigorous stirring for several hours

Large gold nanoparticles of ~55 nm, ~65 nm, ~100 nm and ~165 nm diameter were prepared by following the previously reported seeded growth method.[207] Briefly, a solution of 2.2 mM sodium citrate in Milli-Q water (150 mL) was heated with a heating mantle in a 250 mL three-necked round-bottomed flask for 15 min under vigorous stirring. A condenser was utilized to prevent the evaporation of the solvent. After boiling had commenced, 1 mL of $HAuCl_4$ (0.025 M) was injected. The color of the solution changed from yellow to bluish grey and then to soft pink in 10 min. The resulting particles are coated with negatively charged citrate ions and hence are well suspended in H_2O. Once the synthesis was finished the solution was cooled down to 90ºC and 1 ml of $HAuCl_4$ solution (0.025 M) was injected. After 30 min, 1 ml of $HAuCl_4$ solution (0.025 M) was injected again. After that, the sample was diluted by extracting 50 ml of sample and adding 45 ml of Milli-Q water and 5 ml of $C_6H_5Na_3O_7{\cdot}2H_2O$ 60 mM. This solution was then used as the seed solution (NPs diameter ~8.4 nm). This growing process was repeated six times to obtain particles of ~55 nm diameter, seven times to obtain particles of ~65 nm diameter, ten times to obtain particles of ~100 nm diameter, and thirteen times to obtain particles of ~165 nm diameter.

5.2.4 Assembly of PS@Au NPs/Ag NPs microbeads

Polystyrene microbeads of 3 μm diameter (0.5 mL of a 100 mg/mL suspension) were first wrapped with alternating polyelectrolyte monolayers using the layer-by-layer (LbL) electrostatic self-assembly protocol.[204,208,209] Four alternate layers of opposite charge were deposited: PSS, PEI, PSS, and, finally, PEI. Polystyrene microbeads (0.5 mL of a 100 mg/mL suspension) were added to 25 mL of a 2 mg/mL PSS aqueous solution containing 0.5 M NaCl. After 30 min of sonication and 2 h of agitation the PS microbeads were extensively washed with Milli-Q water and centrifuged (5800 rpm, 20 min). The same protocol (concentrations, elapsed times, and

washing protocol) was carried out for depositing subsequent layers of PEI, PSS and PEI polyelectrolytes. Finally, the PS beads were redispersed in 10 mL of Milli-Q water (final concentration of 5 mg/mL).

The adsorption of the particles onto the functionalized beads was carried out by adding 50 μL of PS beads (5 mg/mL) to 20 mL of Ag colloids ([Ag] = 0.15 mM) and 20 mL of Au colloids (0.1 mM). After 15 min of sonication, the PS@Ag and PS@Au beads were left under gentle shaking for two hours and then left to deposit overnight. The clear supernatant was removed and the process was repeated until reaching full bead saturation (i.e. when the supernatant remained visibly colored). The mixtures were washed first three times by means of centrifugation (3000 rpm, 30 min) and then three times by means of decantation with Milli-Q water. The beads were redispersed in 500 μL of milli-Q water (final PS bead concentration of 0.5 mg/mL).

5.2.5 SERS characterization

SERS characterization of Ag nanoparticles: 500 μL of each colloidal suspension was passivated by the addition of 30 μL of a 2% w/w aqueous solution of polyethylene glycol sorbitan monolaurate, a non-ionic surfactant (Tween® 20). This was done in order to prevent unwanted aggregation of the particles upon the addition of the Raman probe. Then, BT was added to a final concentration of 1×10^{-6} M and the samples were left aging overnight. Finally, the samples were centrifuged and redispersed in 60 μL of milli-Q water. The same functionalization protocol was applied for Au nanoparticles. However, the final BT concentration in the samples were 7×10^{-7} M before the final centrifugation step in this case. The chosen [NP]/[BT] ratio was carefully selected to afford a sub-monolayer coverage of the Raman probe on the metal surface. Thus, the SERS performance of the different colloids can be safely ascribed only to the individual nanoparticle properties whereas the number of BT molecules investigated remains constant and the uncontrolled formation of hot-spots in nanoparticle clusters is avoided.

SERS characterization of the PS@Ag and PS@Au beads: 100 µL of PS@Ag and PS@Au (0.5 mg/mL of PS beads) were mixed with 1 mL of an ethanolic solution of 10^{-3} M BT. After 2h aging, the beads were submitted to one centrifugation/washing cycle with ethanol and two centrifugation/wash cycles with milli-Q. The samples were finally redispersed in 100 µL of milli-Q water and investigated by SERS under the macro condition using a long working distance objective. For micro SERS measurements, 10 µL of the different samples of coated PS@Ag and PS@Au beads was deposited on a clean glass slide. Each sample was prepared at least twice under the same conditions, and at least 15 different beads were measured for each sample to ensure reproducibility.

5.2.6 Instrumentation

SERS experiments were conducted using a Renishaw InVia Reflex confocal microscope equipped with a 1200 grooves cm^{-1} grating for the NIR wavelengths, additional band-pass filter optics, and a CCD camera. Spectra were acquired using 532 nm, 633 nm and 785 nm laser excitations either in macro condition by focusing the laser on the sample with a long working distance objective or in micro set-up by using a 50× objective (N.A. 0.75). UV-vis spectra were recorded using a Thermo Scientific Evolution 201 UV-visible spectrophotometer. Environmental scanning electron microscopy (ESEM) was performed with a JEOL 6400 scanning electron microscope. Transmission electron microscopy (TEM) was performed with a JEOL JEM-1011 transmission electron microscope.

5.3 Results and Discussion

The preparation of the polystyrene beads decorated with Ag or Au nanoparticles (PS@Ag and PS@Au, respectively) was performed via the layer-by-layer assembly protocol, as previously described.[204] Negatively charged polystyrenesulfonate (PSS) and positively charged branched-polyethylenimine (PEI) were alternatively deposited onto PS beads of 3 µm diameter to form a final dense external layer of PEI. In a second step, significant excesses of the negatively charged Ag or Au colloids were

added and left to adhere via electrostatic interaction to the external positively charged PEI layer of the PS beads, thereby saturating the microparticle surfaces. Finally, the PS@nanoparticle structures were extensively washed to remove the unbound nanoparticles. All Ag and Au colloids were prepared via standard chemical methods using citrate and/or ascorbic acid as reducing agents and citrate as a stabilizing agent. The use of surfactants or polymers such as CTAB or PVP with a high affinity to the metal surfaces were carefully avoided as both of them would have dramatically altered the surface chemistry of the nanostructures, impacting their adhesion onto the PS surface as well as the accessibility of the Raman label to the metallic surface.[206,210]

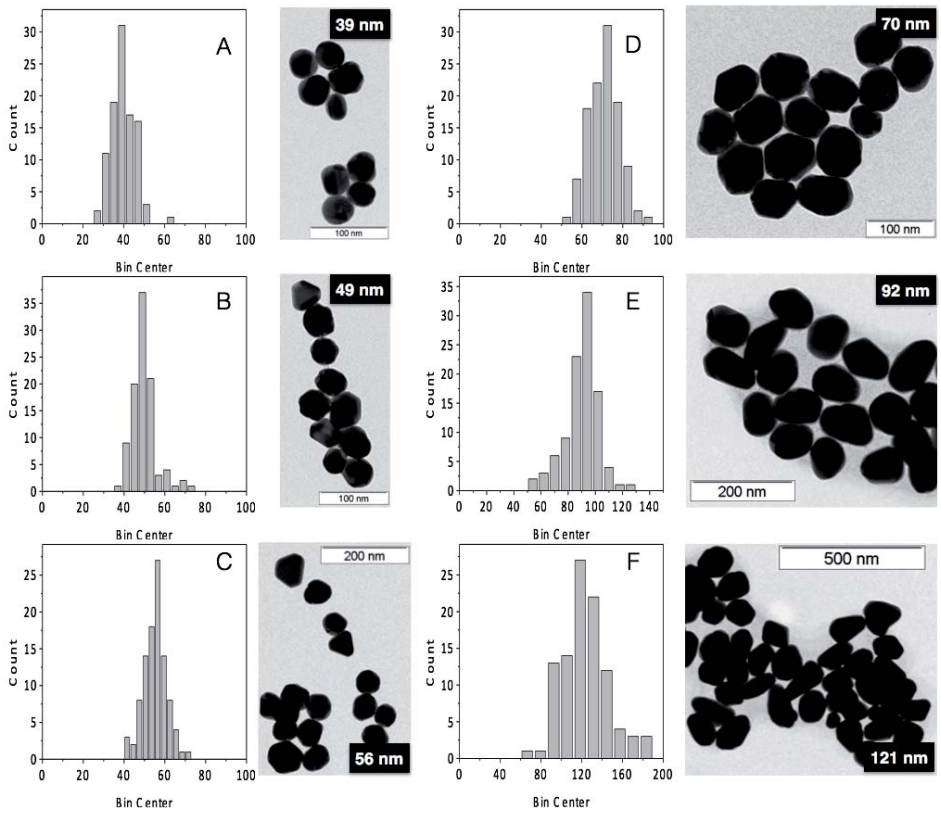

Figure 34. Histogram of Ag nanoparticle diameters and representative TEM image of the dried colloids. (A) Ag NPs of 39 nm diameter, (B) Ag NPs of 49 nm diameter, (C) Ag NPs of 56 nm diameter, (D) Ag NPs of 70 nm diameter, (E) Ag NPs of 92 nm diameter and (F) Ag NPs of 121 nm diameter.

Monodispersed quasi-spherical silver nanoparticles (Ag NPs) with average diameters of 39 nm, 49 nm, 56 nm, 70 nm, 92 nm and 121 nm were prepared using a modified protocol based on previously reported strategies.[129,181,206] Figure 34A-F shows representative TEM images of each colloid together with their size distribution histograms. The size of Ag NPs was controlled by adjusting the concentrations of the different reactants in milli-Q water (trisodium citrate, ascorbic acid, silver nitrate and magnesium sulfate), as reported in Table 2.

Figure 36A shows the normalized extinction spectra of the different Ag colloids in suspension. The spectra reveal the characteristic localized-surface plasmon resonances (LSPRs) of spherical silver nanoparticles centered in the UV spectral range, which progressively shift to the higher wavelengths and broaden when the average size increases. Thus, starting from the peak position around 400 nm, typical of the plasmon resonance of ~39 nm Ag NPs, it red-shifts to longer wavelengths, peaking at ~410 nm for Ag NPs with an average diameter of 49 nm. When Ag NPs size further increases, the main dipolar resonance band red-shifts and broadens, peaking at ~432 nm for Ag NPs with an average diameter of ~56 nm. Above this size, a new peak started to develop at shorter wavelengths, at ~390 nm, characteristic of the quadrupole component of the plasmon resonance for Ag NPs of 70 nm in diameter, which broadens and red-shifts to ~400 nm and ~ 412 nm as the the size increases to 92 nm and 121 nm respectively. This high-order LSPR mode reach a magnitude even higher than the dipolar resonance for nanoparticles of 121 nm in diameter.[211] In fact, as the nanoparticle size increases, light cannot polarize homogeneously and the field is no longer uniform throughout the NP, which results in the phase retardation effect. As a consequence, a red-shift and broadening of the dipolar resonance is observed in the larger particles along with the appearance of higher-order modes.[212,213].

The Raman enhancing ability of the different monodispersed colloidal suspensions was evaluated by adding BT as a Raman probe. BT is commonly used as a molecular probe for characterizing the SERS properties of plasmonic substrates. On the other hand, this is because its –

SH group shows a very high affinity toward noble metal surfaces, which leads to the formation of covalent sulfur-metal bonds. On the other hand, BT has also a high Raman cross-section and so provides intense SERS signals with a well-defined vibrational fingerprint. Previous to the addition of BT, the colloids were passivated with Tween 20, a nonionic surfactant. Differently to surfactants such as CTAB or PVP, Tween 20 simply physisorbes on the metallic surface to provide an effective steric protection that prevents the uncontrolled formation of nanoparticle clusters due to the adsorption of BT molecules perturbing colloidal stability.[214,215] For a meaningful comparison of the enhancing performance of colloids with different nanoparticle size and concentration (i.e. different silver surface areas available for BT adhesion), a fixed amount of Raman label was added to provide sub-monolayer coverage for the all investigated samples rather than saturating the metallic surfaces. In this way, the number of molecules contributing to the vibrational spectra is constant and, thus, to a first approximation the final SERS intensity is solely associated to the Raman signal enhancing properties of the different nanoparticles in suspension. The validity of this approximation also lies in the fact that the field enhancement over nanoparticles of spherical geometry shows relatively good uniformity.[211] Figure 36B illustrates the characteristic SERS spectra of BT on Ag colloids acquired at 532 nm, 633 nm and 785 nm excitation, respectively. The spectra are dominated by the intense ring breathing bands at ca. 999, 1023 and 1073 cm^{-1} (the last one coupled with νCS) and the CC stretching vibrations at ca. 1574 cm^{-1}.[216] The comparison of the different SERS efficiency provided by the Ag colloids is reported in Figure 36C. It is where the intensity of the BT band at 1073 cm^{-1} is plotted against the average nanoparticle size. It is known that for individual quasi-spherical nanoparticles, there is a qualitative connection between extinction and SERS enhancement[217] (whereas no correlation is observed for plasmonically interacting objects[217,218]). For Ag nanospheres, the most intense electromagnetic fields occur when laser excitation is centered at the LSPR maxima, even though the long tail distribution of the SERS enhancements allows to obtain large signal intensification in spectral regions where the plasmon resonances are very weak.[211,217] Thus, the red-

shift of the LSPRs maxima of Ag colloids toward the spectral position of the excitation sources by increasing the nanoparticle sizes is expected to improve the interaction of the external field with the plasmon resonances. On the other hand, LSPRs significantly broaden due to radiation losses when the NP size is increased above ca. 50 nm diameter.[211] Therefore, the optimal nanoparticle size that maximizes SERS enhancement is a compromise between these two opposite factors and depends, among others elements, on the excitation wavelength. This is clearly shown by the experimental data illustrated in Figure 36C which highlights how the optimum nanoparticle size approximately increases as the excitation source is shifted to longer wavelength, from 532 nm to 633 nm and finally to 785 nm.

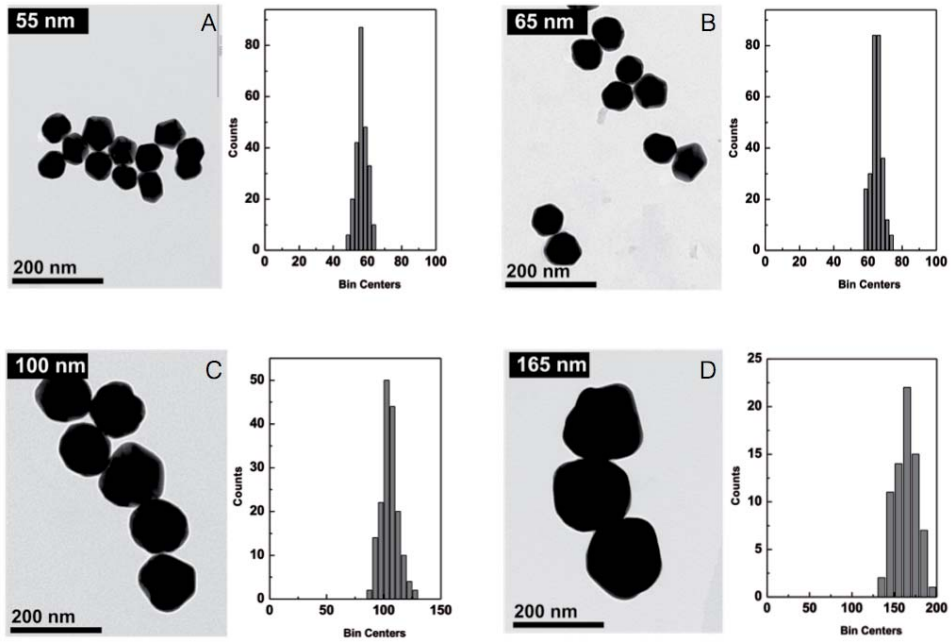

Figure 35. Histogram of Au nanoparticle diameters and representative TEM image of the dried colloids. (A) Au NPs of 55 nm diameter, (B) Au NPs of 65 nm diameter, (C) Au NPs of 100 nm diameter and (D) Au NPs of 165 nm diameter.

Highly monodispersed quasi-spherical citrate-stabilized gold nanoparticles of different average sizes (15, 55, 65, 100 and 165 nm) were produced following a seeded growth strategy based on the classical Turkevich/Frens reaction (Figure 35).[207] The normalized extinction spectra

of the corresponding colloidal suspensions are illustrated in Figure 37A, where the characteristic red-shift and broadening of the LSPR for larger nanoparticle diameters is observed.[211]

Differently to silver, quadrupolar resonance modes are only observed for a particle size above 100 nm,[213] as clearly revealed by the shoulder at shorter wavelengths appearing in the 165 nm gold colloids. Figure 37B shows the SERS spectra of BT on the Au (55nm) NPs suspensions upon excitation with 633 nm and 785 nm lasers. Due to the large optical absorption of gold at shorter wavelengths (< 600 nm),[211] no distinguishable SERS signal can be collected when illuminating gold nanoparticles with the 532 nm excitation source. As for silver nanoparticles, the Raman signal enhancing ability of the different monodispersed colloidal suspensions was evaluated by adding a sub-monolayer amount of BT molecules in the presence of Tween 20 as a stabilizing agent. The normalized SERS intensities of the ring breathing band at 1073 cm^{-1} are plotted against the average nanoparticle size in Figure 37C. It shows a marked increase in SERS activity upon enlarging the nanoparticle diameter up to a maximum of around 100 nm. This is consistent with previous experimental studies.[183,219] In fact, incrementing nanoparticle size causes a red-shift of the LSPR, whose maximum is tuned closer to the wavelengths of the excitation sources. However, for sizes larger than ca. 100 nm, the radiation damping becomes dominant,[211] significantly reducing the electromagnetic fields at the metallic surface. It can be observed by the poor enhancing performance of the 165 nm gold nanoparticles.

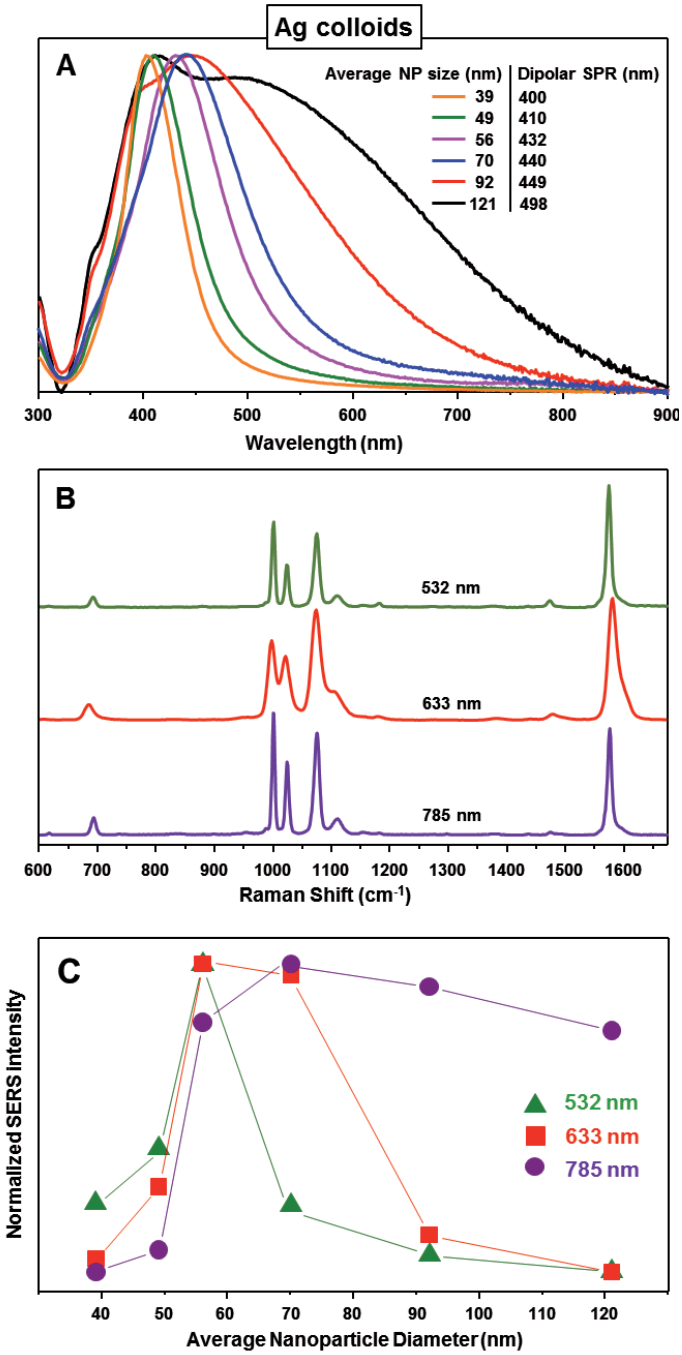

Figure 36. (A) Normalized extinction spectra of Ag colloids. (B) SERS spectra of BT on Ag(56nm) NPs colloids at 532 nm, 633 nm and 785 nm. (C) Normalized SERS intensities of the BT band at 1073 cm^{-1} on silver colloids at 532 nm, 633 nm and 785 nm for different nanoparticle sizes.

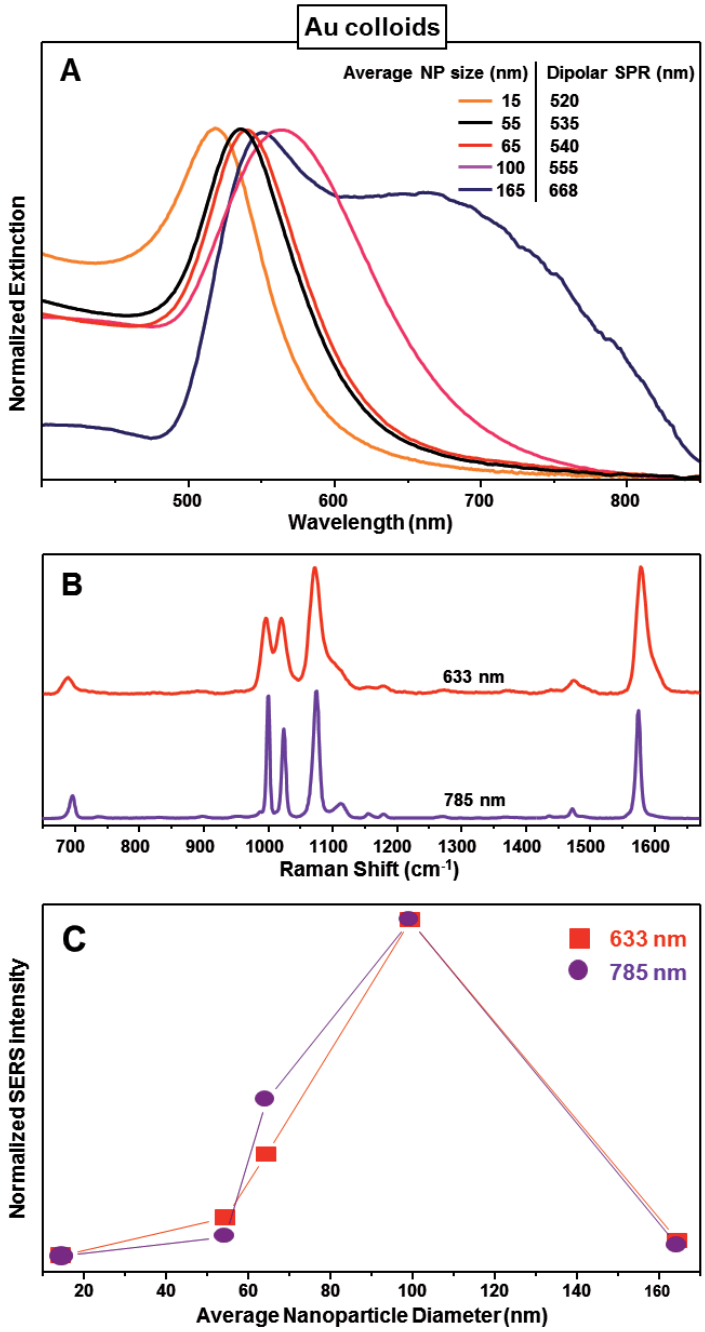

Figure 37. (A) Normalized extinction spectra of Au colloids. (B) SERS spectra of BT on Au(55nm) NPs colloids at 633 nm and 785 nm. (C) Normalized SERS intensities of the BT band at 1073 cm^{-1} on gold colloids at 633 nm and 785 nm for different nanoparticle sizes.

Silver and gold nanoparticles were then assembled onto the PS beads until surface saturation (Figure 38 and Figure 39). As a result, plasmonic coupling of the interacting metallic nanoparticles on the bead surface leads to a reshaping of the extinction spectra as well as alteration of the nanoparticle size-dependent pattern of the SERS response.[203]

The extinction spectra of the PS@Ag beads in suspension are shown in Figure 38A. First of all, it is important to notice how the PS core contributes to the overall spectra with a large scattering background that is characterized by a well-defined band centered at ca. 470 nm and a long tail at the longer wavelength. Nonetheless, it is possible to recognize two new contributions in the extinction profile of PS@Ag. There is one blue-shifted with respect to the PS feature at 470 nm and a second broader one in the ca. 500-580 nm range. The latter can be ascribed to the dipolar coupling between individual nanoparticle dipolar LSPRs whereas the resonances appearing at shorter wavelengths may be due to the poor/null plasmonically interacting single nanoparticles and/or the high-order interactions between single-sphere dipolar LSPRs.[211]

Similarly, the plasmonic interaction between closely spaced gold nanoparticles is revealed by the change of the extinction spectra (Figure 39). A significant red-shift of the plasmon resonances is observed, overlapping the large scattering background of the PS cores, as compared to the original LSPRs of the monodispersed colloids. It is worth noting that the PS@Au(165nm) suspension retains a significant number of unbound Au nanoparticles which were not possible to remove efficiently through the normal sedimentation protocol as for the other samples. This difficulty arises from the fact that the colloidal solution of large Au NPs naturally settles due to the gravitational force. Thus, the UV-Vis spectrum of PS@Au(165nm) may be significantly biased by the contribution of free gold nanoparticles.

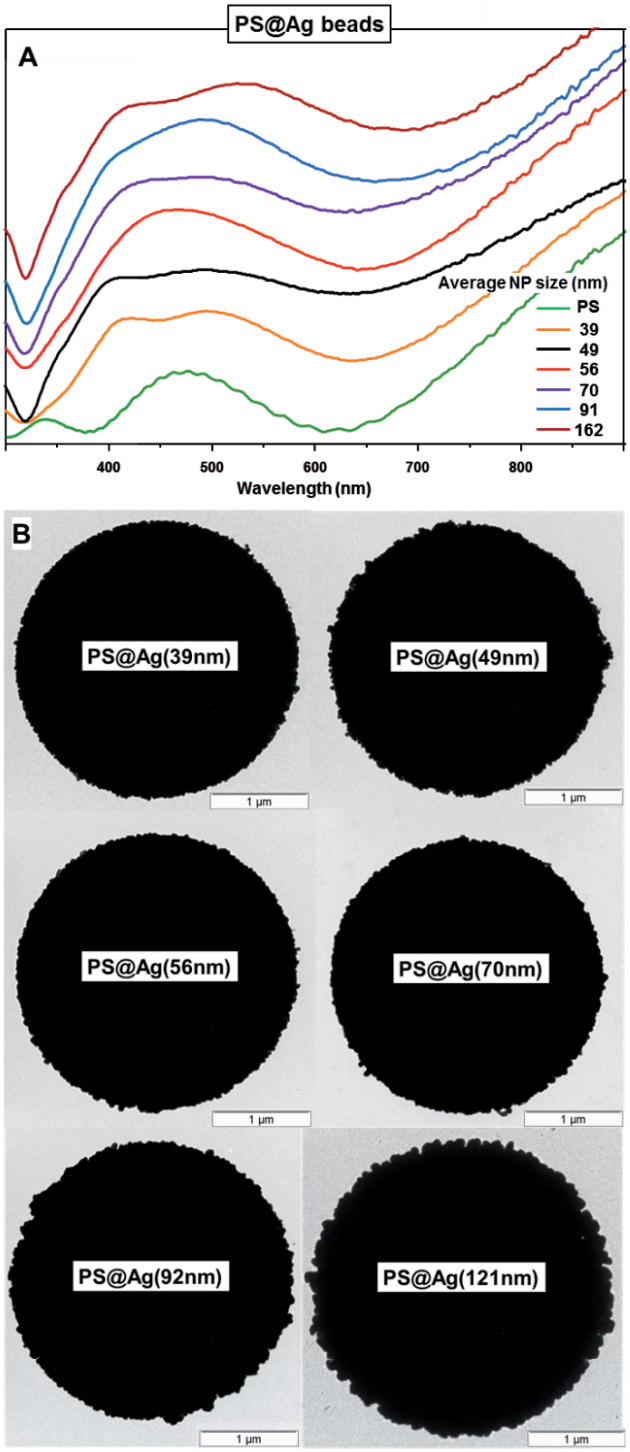

Figure 38. (A) Extinction spectra of PS@Ag composite materials in suspension (normalized and stacked). (B) Representative TEM images of PS@Ag beads.

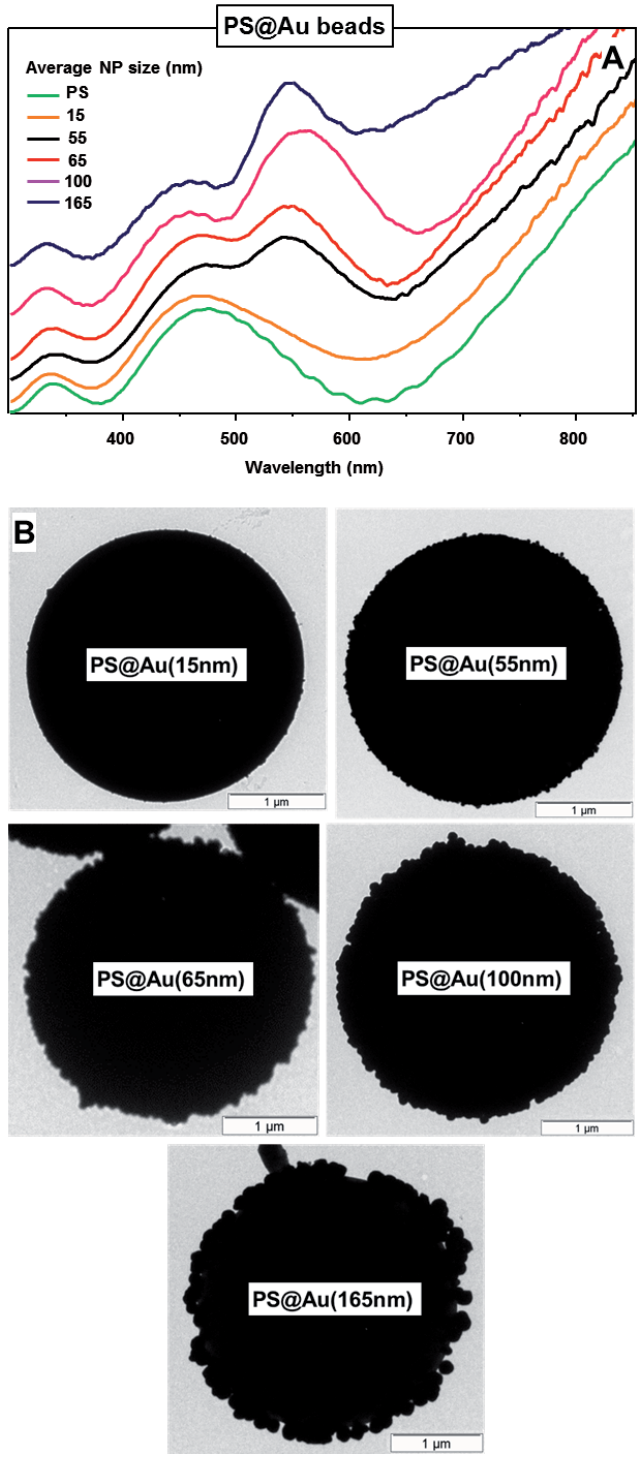

Figure 39. (A) Extinction spectra of PS@Au composite materials in suspension (normalized and stacked). (B) Representative TEM images of PS@Au beads.

Further on, the size-dependent profile at different excitation wavelengths of the normalized SERS intensity of PS@Ag and PS@Au samples (Figure 41A and B, respectively) was investigated. The illustrated data were obtained by averaging the SERS response of the beads in suspension that was investigated with a long working distance objective (macro set-up) and 15 different beads dried on a glass slide using a 50× objective (micro set-up). This averaging process was performed to minimize the contribution to the final results of experimental uncertainties associated with, for instance, the exact bead concentration in suspension after several centrifugations/washing cycles, the focusing of the laser spot on each beads etc. The SERS activity of the PS@Ag beads was tested by measuring the signal intensity of the BT band at 1073 cm^{-1}. In this case, the beads were fully saturated with the Raman label by exposing them to an excess BT in an ethanolic solution which implies that the number of BT molecules yielding the final SERS spectra differs from sample to sample. Thus, the results in terms of SERS intensities per 1 nm^2 of metallic surface available on the PS coated-bead were expressed to correct such variations. This estimation was performed by assuming a full monolayer coating of metallic nanoparticles on top of the PS surface. The results illustrated in Figure 41A highlight a drastic change in the size-dependent SERS performance of Ag nanoparticles when assembled on the surface beads as compared to their individual condition in suspension (Figure 36C). For green laser excitation, SERS activity decreases with the increase of nanoparticle size, whereas SERS performance reaches a maximum for Ag nanoparticles of 56 nm and ca. 56-70 nm, respectively, in the case of 633 nm and 785 nm. On the other hand, the averaged and normalized SERS values obtained for PS@Au composites are reported against the average nanoparticle diameter in Figure 41B. At both excitation wavelengths, the enhancing performance of the composite materials decreases according to the following order: PS@Au(55nm) > PS@Au(65nm) >> PS@Au(15nm) > PS@Au(100nm) > PS@Au(165nm).

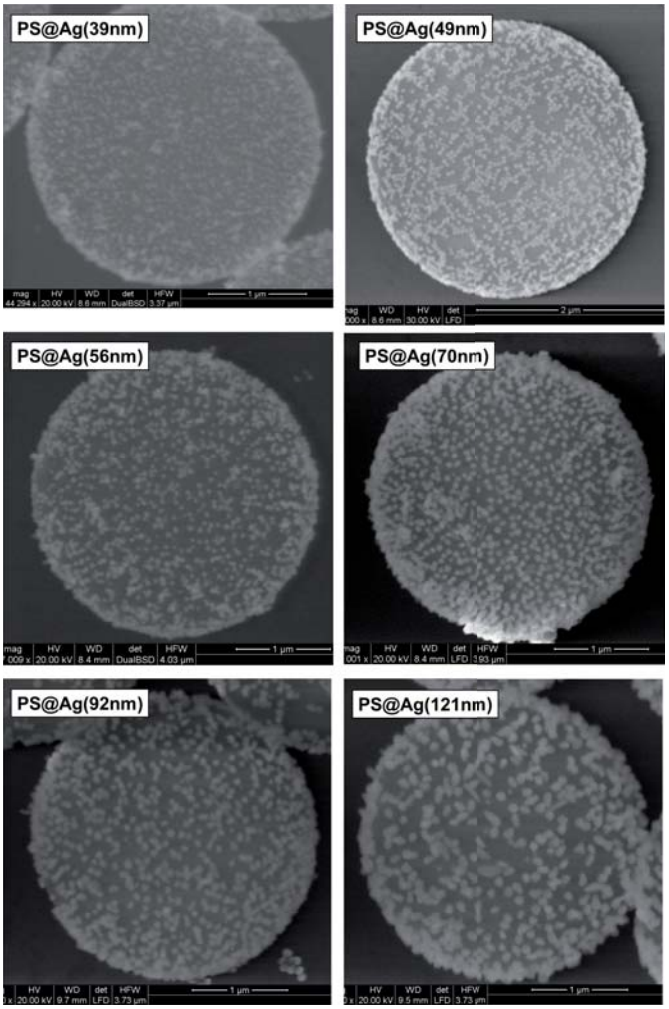

Figure 40. Representative ESEM images of PS@Ag composite beads.

Finally, in Figure 41C the relative SERS efficiency of PS@Au_{55} and PS@Ag(56nm) at the different excitation wavelengths was compared. A silver-based composite provides a much more efficient SERS substrate for shorter wavelengths whereas the enhancement performances of PS@Au_{55} beads become very similar to those of PS@Ag(56nm) at 785 nm. This is associated with the generation of interparticle gap-associated resonances, the most important ones for SERS, which are shifted beyond 600 nm. It is where the optical absorption of gold is low and both metals (Ag and Au) behave similarly.[211]

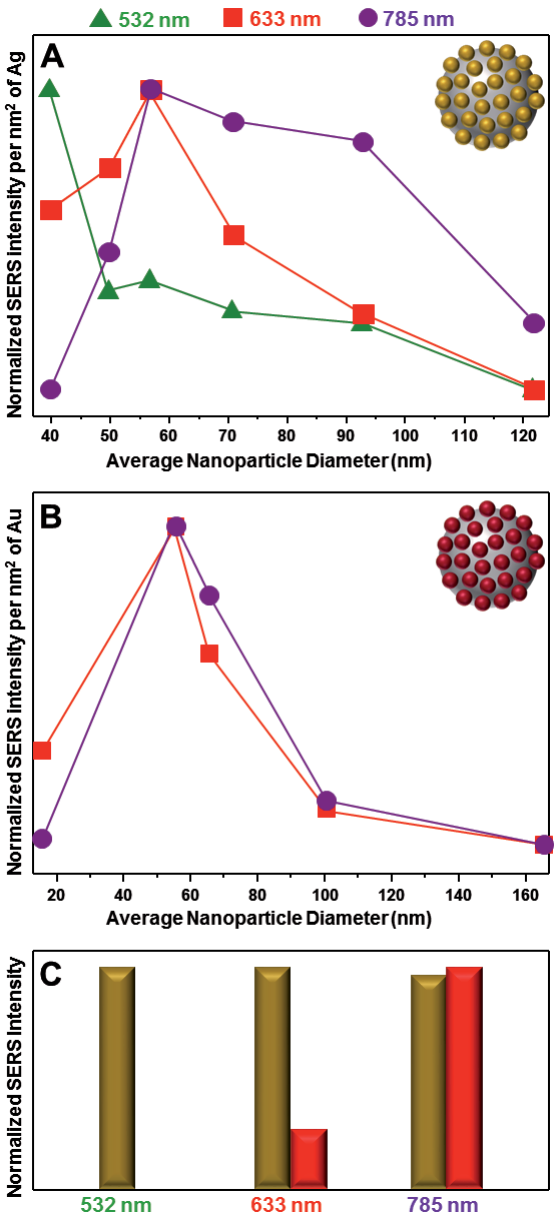

Figure 41. (A) Normalized SERS intensities of the BT band at 1073 cm^{-1} on PS@Ag at 532 nm, 633 nm and 785 nm respectively for different nanoparticle sizes. (B) Normalized SERS intensities of the BT band at 1073 cm^{-1} on PS@Au at 532 nm, 633 nm and 785 nm respectively for different nanoparticle size. (C) Relative SERS efficiency of PS@Au(55nm) and PS@Ag(56nm) at the three excitation wavelengths. In this case, for a specific excitation wavelength, the SERS measurements were performed under the same experimental conditions for both PS@Ag(56nm) and PS@Au(55nm). Subsequently, the recorded BT SERS intensities (peak height at 1073 cm^{-1}) were normalized to the maximum value.

5.4 Conclusions

In summary, a thorough investigation of the correlation between the size of quasi-spherical Ag and Au nanoparticles and the SERS efficiency of the corresponding composite hybrid materials was performed. These hybrid materials comprise a polystyrene micro-core and a dense external layer of interacting nanoparticles and were used as a bacteria model to simulate the SERS signal when a conjunction of SERS tags specifically agglutinate onto microorganism's membrane. Thiophenol was selected as an efficient Raman label for the SERS study. The results show how the enhancing ability of the PS@Ag/Au substrates are strongly determined by the size (and composition) of the individual nanoparticles, and the dependency on the selected excitation wavelength. In the case of PS@Ag composite microparticles, silver nanoparticles of ca. 39 nm, 56 nm and 56-70 nm yielded the most efficient substrates at the three investigated excitation wavelengths (532 nm, 633 nm and 785 nm, respectively). On the other hand, for PS@Au, gold nanoparticles of ca. 55 nm diameter resulted in the best choice for all laser sources. Relative to the nanoparticle composition, silver-based hybrid beads generated the most intense SERS signals when illuminated with the 532 nm and 633 nm lasers, whereas the SERS performances of PS@Au(55nm) and PS@Ag(56-70) are similar under the 785 nm excitation. Likewise, when adequate SERS tags agglutinate on the microorganism membrane the SERS signal should be dominated by the generation of interparticle-gap resonances and, for that reason, the size of the encoded nanoparticles also plays a key role as it affects to the number and efficiency of the hot-spots. Therefore, these findings offer important information for an appropriate selection of optimum SERS tags. Silver or gold nanospheres of 50-70 nm of diameter are a good start point for microorganism detection in real samples using a 785 nm excitation wavelength.

6 Ultrasensitive multiplex optical quantification of bacteria for PJI diagnosis

6.1 Introduction

While the number of joint arthroplasties being implanted has risen and will continue to do so,[4] the dynamics of the incidence of PJI are unclear. Using nation-wide in-patient sample (NIS) data, 2.0% of the total hip arthroplasties and 2.4% of the total knee arthroplasties become infected.[8] However, studies using more precise definitions for PJI have reported that the use of preoperative antimicrobial prophylaxis and a laminar air-flow surgical environment has reduced the risk of intraoperative infection to less than 1.0% after hip and shoulder replacement and to less than 2.0% after knee replacement.[9] On the other hand, other studies have reported an increasing incidence of PJI in hip and knee arthroplasties.[10,220] While it is unclear whether the incidence of PJI per person-joint-years is increasing or not, the absolute number cases will surely increase due to the increasing number of primary implantations being performed and the cumulative number of arthroplasties that remain in place.[221] The incidence of PJI may seem small but it causes great suffering (including death in 3 to 4% of the cases[40]) in those affected and has a real impact on the economy of healthcare systems. The overall cost to the American health care system to treat PJI was $566 million in 2009 and is projected to reach $1.62 billion in 2020.[220]

Besides the obvious economic benefits, a fast, accurate, and inexpensive diagnostic method thus promises to be a powerful tool for alleviating human suffering. Microbial culturing is still the most widespread technique for identifying the infectious agent. Unfortunately it requires 4-14 days to provide a conclusive diagnosis for common infections.[15] Understandably, a great deal of work has been devoted to developing alternative methods for fast identification of bacteria in suspected patients over the last three decades.[222] These methods include immunology-based approaches (e.g., enzyme-linked immunosorbent assay (ELISA), as well as fluorescence and radio immunoassays),[223] nucleic acid identification (e.g., polymerase chain reaction, PCR),[224] and, lately, spectrometry-based procedures (e.g., matrix-assisted laser desorption/ionization-time-of-flight,

MALDI-TOF, mass spectrometry).[225] Although generally faster than just sequential microbial culture, these techniques still require hours to days, depending on the pathogen. Additionally, immunological and nucleic-acid tests are expensive (around $200 each) and monoplex (one test per target microorganism), while MALDI-TOF still relies on microbial culturing to isolate pure colonies. As a consequence, a cocktail of broad-spectrum antibiotics is generally recommended to cover all potential pathogens until a conclusive identification is obtained. Apart from its inherent cost and adverse health effects, this indiscriminate use of antibiotics induces bacterial resistance,[18] which is a growing problem in modern pharmacopeia.[226] In addition to the use of antibiotics, surgical procedures are also required that include implant removal, spacer placement or amputation in the worst cases.[227] Despite recent advances in the rapid recognition of bacterial resistance, society clamors for the development of new diagnostic systems capable of providing fast, accurate, inexpensive, and if possible multiplexed identification of infectious agents in body fluids that will yield a rapid and guided treatment that avoids the use of spurious drugs.[228,229]

Recent advances in nanoscience, spectroscopy, magnetism, plasmonics, and microfluidics[224,230–234] have generated great expectations for the development of new approaches to bacteria characterization[235] and detection.[69,144,236–239] Unfortunately, the methods so far proposed are generally time consuming and only capable of exploring small sample volumes (~microliters) not relevant to the clinical diagnosis of PJI.[234,240] Moreover, they work exclusively for one a priori selected pathogen,[236,241] are not truly multiplex,[237] requiring from multiple external labels,[69] or rely on additional steps to record a suitable signal for identification.[144,234] This section reports a microorganism optical detection system (MODS) and demonstrate exhaustive pathogen identification through the rapid screening of large volumes of body-fluid (milliliters of blood or serum) for bacterial content, down to the detection of a single colony forming unit, as required by standard medical practice for the analysis of biological samples.[27] Specifically, the detection and quantification of bacteria in real time and in a multiplexed manner is achieved.

6.2 Experimental section

6.2.1 Materials and methods

Silver nitrate (99.99%, $AgNO_3$), trisodium citrate dehydrated (≥99.5 %, $C_6H_5Na_3O_7{\cdot}2H_2O$), L-ascorbic acid (≥99.0%, AA), magnesium sulfate (≥99.0%, $MgSO_4$), ethanol (99.5%, EtOH), 11-mercaptoundecanoic acid (95%, MUA), 4-mercaptobenzoic acid (99%, 4MBA), 2-mercaptobenzoic acid (97%, 2MBA), 3,4-difluorobenzenethiol (96%, DFBT), 2-(trifluoromethyl)benzenethiol (96%, TFMBT), 1-(4-hydroxyphenyl)-1H-tetrazole-5-thiol (97%, HPTZT), bovine serum albumin (≥98.0% , BSA), *N*-(3-dimethylaminopropyl)-*N*′-ethylcarbodiimide hydrochloride (BioXtra, EDC), sodium chloride (BioXtra, ≥99.5%, NaCl), Dulbecco's phosphate buffered saline (D8537, DPBS), and human blood (BCR634 FLUKA) were purchased from Sigma-Aldrich. All reactants were used without further purification. MilliQ water (18 MΩ cm^{-1}) was used in all aqueous solutions, and all the glassware and magnetic stirrers were cleaned with aqua regia and with a potassium hydroxide solution in isopropanol/water before all the experiments.

Antibodies selected for this study are the same that those used in the clinical practice for the immunological methods. *Escherichia coli* (ab30522, *E. coli*) and *Streptococcus agalactiae* (ab41203, *S. agalactiae*) antibodies were purchased from Abcam. *Pseudomonas aeruginosa* (MA1-83430, *P. aeruginosa*) and *Staphylococcus aureus* (MA1-83467, *S. aureus*) antibodies were purchased from Life Technologies. Enriched thioglycollate medium (221742, BBL) was purchased from BD (Becton, Dickinson and Company*)* and Columbia agar + 5% sheep blood plates (43 041) were purchased from bioMérieux. Bacterial samples were obtained from the Department of Clinical Microbiology, Hospital Clinic, Barcelona, Spain.

6.2.2 Synthesis of citrate-stabilized spherical silver nanoparticles of ~60 nm diameter

Spherical silver nanoparticles (Ag NPs) of approximately 62 nm in diameter were produced with a combination of previously reported approaches.[129,181,206,242] Briefly, 250 mL of MilliQ water were heated under vigorous stirring. A condenser was used to prevent solvent evaporation. Next, aqueous solutions of trisodium citrate (3.41 mL, 0.1 M) and ascorbic acid (0.25 mL, 0.1 M) were consecutively added into the boiling water. After 1 min, a premixed aqueous solution containing $AgNO_3$ (0.744 mL, 0.1 M) and $MgSO_4$ (0.56 mL 0.1 M), which was previously incubated at room temperature for 5 min, was rapidly injected into the reaction vessel under vigorous stirring. The color of the solution quickly changed from colorless to yellow and then gradually to dark orange. Boiling was continued for 1 h under stirring to ensure the completeness of the reaction. The silver concentration of the synthesized particles was 2×10^{-4} M (i.e., ~10^{10} NPs per mL).

6.2.3 Mercaptoundecanoic acid functionalization and codification of silver nanoparticles

After NP synthesis, MUA was used in order to provide colloidal stability to the Ag NPs during the encoding process and also, to use the carboxylic functionality for the coupling of the antibodies. Specifically, five aliquots (25 mL each) of the synthesized Ag NPs were cleaned with centrifugation (5400 rpm, 30 min) and redispersed via sonication (during 5 min) in a solution containing MilliQ water (3.27 mL) and EtOH (21.67 mL). Subsequently, the Ag NPs were functionalized with a small amount of MUA (2.4 molecules nm^{-2}) by rapidly adding a solution containing MUA (24.76 µL, 1.0×10^{-3} M in EtOH) and NH_4OH (30 µL, 29% aqueous solution) to each aliquot under vigorous stirring. Agitation was continued for 28 h to assure the complete MUA functionalization on the silver surface. Finally, the MUA functionalized Ag NPs aliquots were encoded with five different Raman labels (1.6 molecules nm^{-2} of 4MBA, 2MBA, DFBT, TFMBT, and HPTZT,

respectively). To this end, 16.51 µL of a 10^{-3} M stock solution of the five different SERS codes were added to the aliquots under strong magnetic stirring. Once again, stirring was continued for another 28 h. The encoded Ag NPs solutions were then centrifuged and redispersed twice in MilliQ water to remove the excess of NH_4OH, EtOH, and any unreacted Raman label prior to antibody coupling. The concentration of NPs was calculated for each aliquot using the Lambert-Beer law and an extinction coefficient of 7.79×10^{10} M^{-1} cm^{-1}, derived from the literature[182] and adjusted to 0.14 nM for all of them.

Additionally, another aliquot (25 mL) of the synthesized Ag NPs was cleaned with centrifugation (5400 rpm, 30 min) and redispersed in MilliQ water (25 mL). The Ag NPs were then functionalized with MUA by adding, under vigorous stirring, 24.76 µL (1.0×10^{-3} M in EtOH). Agitation was continued for 28 h to ensure the complete MUA functionalization on the silver surface. Finally, Ag NPs were further modified with BSA (41.26 µL, 1.0×10^{-3} M in MilliQ water) under magnetic stirring for 24 h, followed by one cleaning step centrifugation to remove excess BSA and any unreacted MUA molecules (5400 rpm, 30 min, redispersed in MilliQ water). The concentration of these NPs was calculated and adjusted to 0.034 nM.

6.2.4 Antibody conjugation to silver nanoparticles

200 µL of DPBS and EDC (39.2 µL, 250 nM in DPBS) were added over each codified Ag NPs solution (1 mL, 0.14 nM, Raman labels: 4MBA, 2MBA, DFBT, TFMBT, and HPTZT), the mixtures were shaken for 5 min at room temperature, and then the antibodies solutions were added (1.46 µL, ~6.67 µM, *E. coli*, BSA, *P. aeruginosa*, *S. agalactiae,* and *S. aureus,* respectively). The resulting mixtures were first shaken for 2 h at room temperature. Then, they were cleaned twice with centrifugation to remove the excess unreacted EDC and antibodies (3000 rpm, 10 min), and redispersed in DPBS/MilliQ water (1:3). The concentration of each Ab-modified Ag NPs solution was measured and adjusted to 0.14 nM. The resulting NP solutions were stored at 4 °C.

6.2.5 Characterization of the nanoparticles

UV-Vis spectroscopy (Lambda 19, PerkinElmer) and transmission electron microscopy (TEM, JEOL JEM-1011 operating at 100 kV) were used to characterize the optical response, structure, and size of the nanoparticles during the functionalization process. To characterize the codification process, SERS spectra were collected in backscattering geometry with a Renishaw Invia Reflex system equipped with a 2D-CCD detector. The spectrograph used a high resolution grating (1200 grooves cm^{-1}) with additional band-pass filter optics. A 785 nm diode laser was focused onto the colloidal solution ($[Ag^0]$ = 0.1 mM) with a long-working distance objective (0.17 NA, working distance 30 mm). The spectra were acquired with an exposure time of 100 ms (depending on Raman intensity saturation) and a laser power at the sample of ca. 300 mW.

6.2.6 Bacterial samples

Bacteria were inoculated in enriched thioglycollate medium (BBL), incubated at 37 °C for 18 h and then diluted with saline solution (NaCl 0.9%). Next, the required amount of bacterial solution, to reach the desired final concentration, was added into the corresponding fluid, a saline solution or human blood containing Ab-modified Ag NPs (1 mL of each encoded particle per mL of sample) and twice as many serum-albumin protected unlabeled Ag NPs as the total amount of codified Ag NPs. To verify the final bacterial concentration per sample, several aliquots of each solution were spread in agar-blood plates and incubated for 24-48 h at 37 °C. After this time, the number of colonies in each plate was counted in order to calculate their CFU concentration per mL. To further corroborate the interaction between the Ab-modified Ag NPs with the corresponding bacteria, equal volumes of Ag NPs (0.14 nM) and bacterial solution (~10^6 CFU mL^{-1}) were mixed, and incubated for 15 min at 37 °C. Small fractions (10 µL) of these mixtures were deposited on carbon coated copper grids and the samples were allowed to dry before performing the TEM analysis.

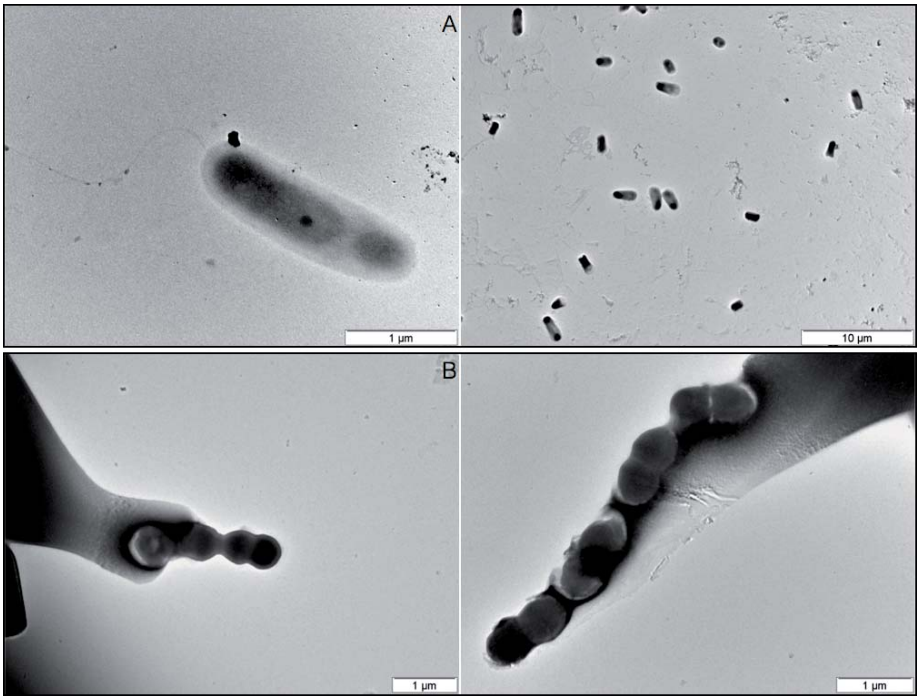

Figure 42. Transmission electron microscope images of incubated bacteria (A) *E. coli* and (B) *S. agalactiae*.

6.2.7 Microfluidic device manufacturing

The microfluidic device was fabricated with polydimethylsiloxane (PDMS) by replica molding using an aluminum master mold. PDMS (Sylgard 184, Dow Corning) was prepared by mixing pre-polymer and a curing agent at a standard 10:1 ratio. The mixture was poured onto the mold, degassed in vacuum, and cured at 80 °C. After one hour, PDMS was peeled off the mold and the fluidic access holes (inlet and outlet) were punched. The final device was obtained by bonding the PDMS layer to a slide cover (130-170 µm-thick) after oxygen plasma treatment (100 W, 3% O_2, 0.2 mbar, 40 s) (Plasma Flecto 10, Plasma technology GmbH). The microfluidic device consisted of a single channel with variable dimensions. The inlet channel had a width of 200 µm and a depth of 100 µm, which was enlarged to 400 µm-width and 2 mm-depth in the outlet channel (i.e., the optical detection section, see Figure 43).

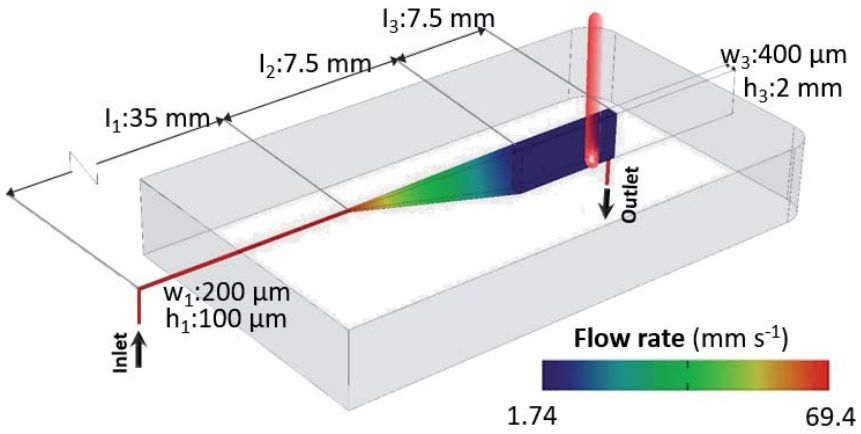

Figure 43. Detailed schematics of the detection region in the millifluidic chipset of Figure 44. The channel is divided into three sections: an initial narrow section used to increase pressure and reduce the flow to finely control the fluid discharge with the pump; a second segment of increasing larger section; and, a third wide segment (0.4 mm width, 2 mm depth), with suitable dimensions to continuously screen the sample at flow rates of 1.74 mm s^{-1}, at a spectral capture rate of 1.83 mm s^{-1}.

6.2.8 Measurement system setup

The microfluidic device was placed onto the stage of the system and appropriately aligned. Inlet and outlet were connected to a syringe and a waste container, respectively, via 0.8 mm-diameter polytetrafluoroethylene (PTFE) and 1.1 mm-diameter tygon tubes. The syringe was pre-charged with the sample and nanoparticles. A standard syringe pump (NE-1000, New Era Pump Systems, Inc.) was used to push the sample at a flow rate of 1.74 mm s^{-1}. SERS measurements were collected with a Renishaw Invia Reflex. The laser (785 nm, 300 mW) was focused with a macro-objective (6 mm aperture and -18 mm focal distance), providing an efficient spot of 0.5 mm. The scan collection time was set to 270 ms per spectrum to provide an acquisition speed of 1.83 mm s^{-1}, which results in an evaluation speed of 13.3 min per mL of sample, during which 3000 scans are obtained. Data deconvolution was carried out by principal component analysis and classical least squares using the Wire 4.1 software from Renishaw.

6.2.9 Electromagnetic simulations

The simulation of the electric near-field and SERS enhancements in Figure 56C, Figure 58 were carried out with a fully converged multiple elastic scattering of multipolar expansions (MESME) method.[243] In particular, the SERS enhancement at a given position was approximated as the product of the field enhancements calculated at that position for wavelengths corresponding to the incident and emitted light. Each of these field enhancements was averaged over incidence light directions and polarizations before multiplying them to yield the SERS enhancement. The field enhancement of Figure 57 was obtained using the boundary-element method (BEM).[244] The dielectric functions of silver used in these simulations were taken from tabulated measurements. The media inside and outside the bacteria were both assumed to have the permittivity of water, ε=1.77. These calculations were performed by the group of Prof. Javier García de Abajo.

6.2.10 Simulation of particle attachment

We simulated the process of NP attachment on the membrane of the targeted bacteria by implementing a Monte Carlo method in which particles landed on the microbe surface at random spots, following either randomly oriented trajectories (Figure 47B, and solid curves in Figure 57 left) or approaching it along the surface normal (dashed curves in Figure 57 left). Particles colliding with any previously stuck particle were disregarded. The probability distribution of random-incidence orientations was taken to be proportional to $\sin\theta \cos\theta$ as a function of incidence angle θ relative to the surface normal, where the cosine function reflects the average particle flux for a surface tilted by that angle, whereas the sine function comes from the Jacobian of spherical coordinates. Statistical analysis of the particle positions produced by these simulations is necessary to obtain the time-dependent particle density (Figure 56B) and the distribution of inter-particle gap distances. Each of the results here presented were averaged over 10^5 simulation runs for a square membrane

of large side compared with the particle diameter. Opposite sides of the square were identified (toroidal topology) to minimize edge effects. Convergence was achieved for a side length ~20 particle diameters.

In the resulting Figure 57 left, the time axis is expressed in units of the average interval between collisions over an area equal to the unit cell of a closed-packed arrangement of the NPs (i.e., a time unit is defined as the average time needed to have one particle colliding for each element of area equal to $3^{1/2}D^2/2$, where D=60 nm is the particle diameter). For the sake of readability, the time in Figure 56B is instead normalized to the average interval separating consecutive particle collisions on an area of 1 μm^2. Finally, for the comparison with experiment in Figure 56A, the theory curve is scaled to have 17.3 collisions per second per μm^2, as predicted by the impingement rate equation. $n\sqrt{\frac{k_B T}{2\pi M}}$, where n=10^9 NP/mL is the particle density (notice that the NP dispersion used to study the kinetics in Figure 56A was diluted with respect to the cocktail used for MODS analyses), T=300 K is the temperature, and M=2.2×10^{-18} kg is the NP mass corresponding to 60 nm silver spheres. These calculations were performed by the group of Prof. Javier García de Abajo.

6.2.11 Simulation of SERS enhancement produced by particle attachment

The temporal evolution of the SERS signal (Figure 56B) was obtained by combining the gap-mediated SERS enhancement (Figure 58B) and the time-dependent particle (Figure 56B) and gap densities. The SERS enhancement was calculated from the weighted contributions of both the individual NPs (Figure 58B, dashed lines) and the gaps formed between them (Figure 58B, solid curves). Incidentally, multiple inter-particle interactions beyond dimers formed by nearest neighbors have a relatively weak effect (Figure 56C and Figure 57), which should be further reduced when averaging over random NP arrangements and light incidence directions and polarizations. Consequently, the SERS enhancement at the gaps was approximated by simulating isolated dimers (Figure 58B). For

simplicity, a zero Raman shift was considered in the simulations (i.e., black solid curve of Figure 58B). The effect of finite Raman shift was marginal, as the particles were operating at an off-resonance wavelength ≥785 nm (see Figure 58A). Incidentally, the SERS enhancement of Figure 56B is normalized to the emission from an individual NP.

Simulation of the effective permittivity of the NP coating described as a metamaterial. In order to quickly assess the effect of the NP coating on the near-field at the large scale commensurate with the microbe, the NPs were assimilated to an equivalent homogeneous thin film with an effective dielectric function calculated in such a way that the film had the same normal-incidence reflection coefficient as a layer of randomly distributed particles (i.e., the layer was treated as a metamaterial). The effective dielectric function was estimated from the dipoles induced per gap and per particle, as obtained from electromagnetic simulations of the gap-size-dependent polarizability of NP dimers using MESME. The effective dielectric function was then expressed as $\varepsilon+(4\pi/t)\beta$, where β is the sum of NP and gap polarizabilities normalized per film-surface area, t is the equivalent film thickness, and $\varepsilon=1.77$ is the permittivity of the surrounding medium (water). The dependence on the choice of t was found to be very mild, and actually, the results obtained for the near-field distribution calculated with t=10 nm and t=20 nm were nearly indistinguishable on the scale of Figure 57 right. These calculations were performed by the group of Prof. Javier García de Abajo.

6.3 Results and discussion

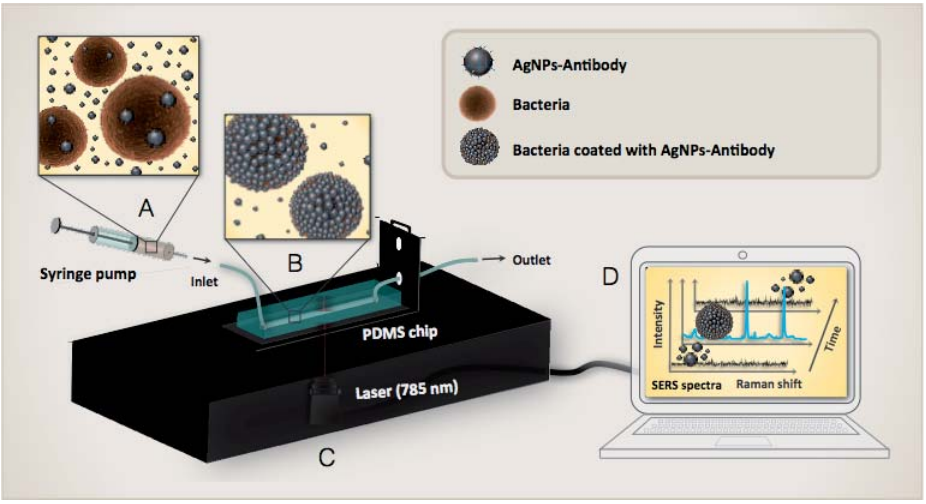

Figure 44. Conceptual view of Microorganism optical detection system (MODS) and its relevant components. (A) Silver nanoparticles are separately labeled with different Raman-active molecules and functionalized with bacteria-selective antibodies. Then, nanoparticle dispersion is mixed in a syringe (3 mL) with the sample fluid, possibly infected. (B) The presence of one of the targeted microorganisms induces aggregation of antibody-matching NPs on its membrane, rapidly evolving towards full random coverage. (C) The mixture is circulated through a microfluidic channel with a pump and passing through the focus of a 785 nm laser, which interrogates the sample in real time. (D) Targeted bacteria produce a large increase in SERS signal, whose spectral fingerprints allow for the identification of the specific pathogen.

Motivated by the need for an accessible, highly sensitive, and selective platform for the screening of pathogens in large samples of biological fluids (i.e., serum or blood) for PJI diagnosis, a detection device as described in Figure 44 was engineered. As already mentioned in section 5, this device relies on the use of plasmonic nanoparticles tagged with Raman-active molecules and functionalized with selective antibodies yielding final SERS tags. In contrast to previous demonstrations of *in vivo* imaging using silica or polymer coated nanoparticles,[245] the plasmonic colloids used in this section are uncoated in order to facilitate their plasmonic interaction (see section 4.3). In section 5, polystyrene beads were used as a bacteria model to simulate these plasmonic interactions when SERS tags specifically agglutinate onto a microorganism membrane

and we saw that silver nanospheres of 50-70 nm of diameter are good candidates for this purpose.

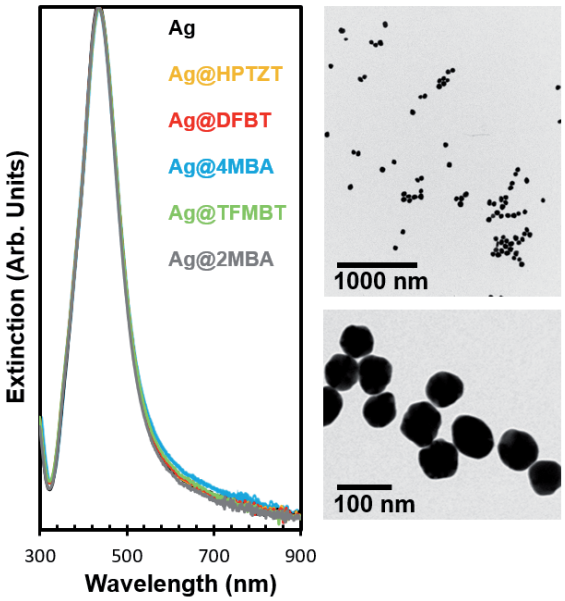

Figure 45. Optical and microscopy characterization of the NPs. Left: Optical extinction of functionalized Ag NPs in an aqueous solution, showing a prominent plasmon consistent with the nominal diameter of 62 nm, and indicating that the coating molecules have a minor effect on the optical response. Right: Representative TEM images of as prepared encoded nanoparticles.

Hence, for each targeted pathogen receptor, NPs (silver spheres, ~60 nm diameter) with a unique combination of Raman label and selective antibody were prepared. The NPs produce a relatively weak Raman signal when they are dispersed in a fluid. In contrast, the presence of one of the targeted pathogens triggers the accumulation of its partner NPs on the antigen-carrying membrane of the microorganism, rapidly reaching full random coverage.[147] Multiple gaps between NPs are then formed that act as optical hot-spots in which Raman scattering is enhanced by several orders of magnitude relative to the same number of noninteracting NPs.[171,246–248] The resulting surface-enhanced Raman scattering (SERS)[68] signal is sufficiently intense as to record pathogen-specific inelastic light spectra (Figure 46A) from the NP-covered bacteria (Figure 46B). By driving the sample through a millifluidic channel (0.4 mm x 2 mm section, using a

pump, see Figure 43), where a backscattered detecting laser (785 nm) continuously monitors the liquid stream (one spectrum every 270 ms over an illuminated volume of ~0.32 µL), quantification of multiple different types of bacteria at a rate of 13 minutes per mL of blood or serum was successfully achieved. Importantly, this method can be readily scaled to cope with many more pathogens including viruses or eukaryotic cells such as fungi or protozoa, in a single pass without increasing the sampling time by simply preparing NPs functionalized with more combinations of Raman labels and selective antibodies.

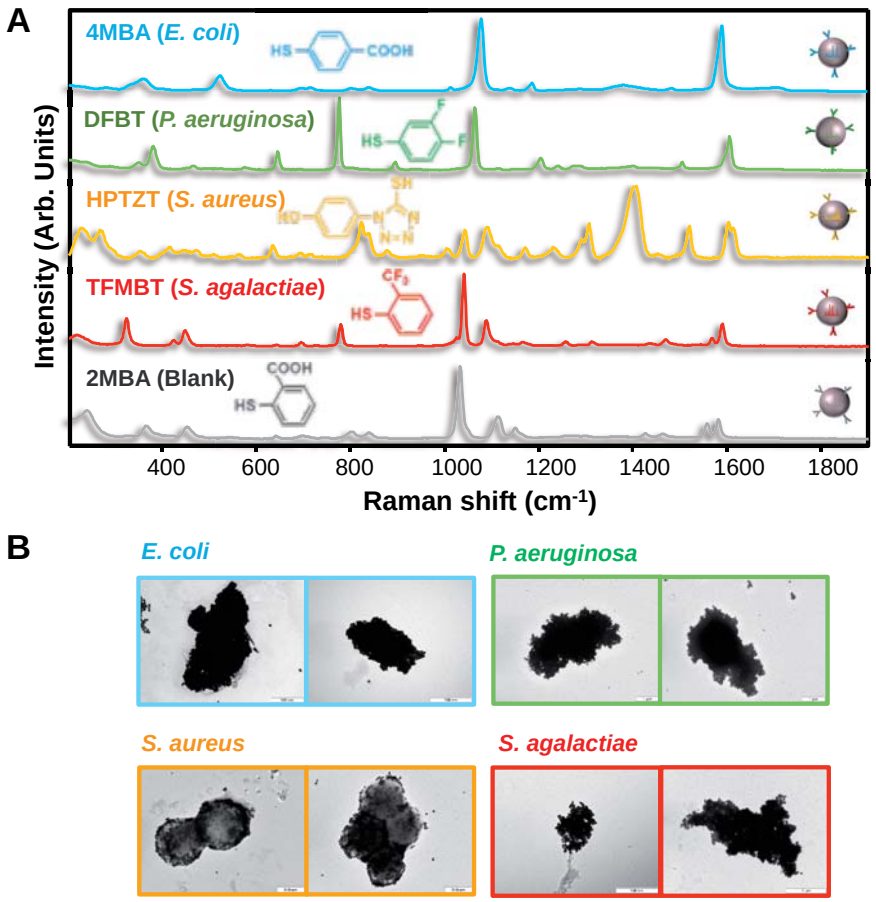

Figure 46. Encoded nanoparticles and their interaction with bacteria. (A) SERS spectra of the different encoded particles here used for each targeted pathogen, along with their corresponding labeling molecules. (B) Transmission electron microscope images of the targeted bacteria (*E. coli*, *P. aeruginosa*, *S. aureus*, and *S. agalactiae*) coated with their respective matching NPs.

To demonstrate bacteria detection, five dispersions of encoded NPs functionalized with a different thiolated aromatic molecule that yields a unique Raman spectrum (Figure 46A and Figure 45) were prepared. The different encoded NPs were subsequently and separately functionalized with the corresponding membrane-selective antibody, at low concentration, for recognition of gram-positive spheroidal coccus including *S. aureus* (the most causative microorganism of PJI) and *S. agalactiae*, as well as gram negative rod-like bacteria *E. coli* and *P. aeruginosa* were included. The fifth NP dispersion was functionalized with serum albumin and used as a blank. All five NP dispersions were then mixed in the syringe (Figure 44) at a concentration of ~10^7 NPs per mL per Raman code. It was found to be optimum for yielding fast NP-pathogen attachment with a minimum background SERS signal of unattached NPs (Figure 47).

Further, to limit the formation of spurious aggregates in the colloidal solution, which may lead to false positives, twice as many non-coded BSA-protected NPs were added to the mixture. As a first demonstration, serum contaminated with only one of the four aforementioned bacteria was added to the MODS mixing vessel, and a time series of SERS spectra were collected as the mixture was circulated through the laser focus (Figure 48A and Figure 49-52). The majority of the time steps only sampled dispersed NPs, which produced a weak or none SERS signal. Occasionally, a targeted CFU traversed the laser focus, giving rise to ~10^3 higher SERS signal due to the concentration of particles on the bacterial surface and the subsequent formation of NP gaps, as discussed above. Then, the correlation of the recorded spectra with the reference ones was calculated for each of the Raman codes (Figure 46A), and a clear identification of the added pathogen was obtained. The experiment was successfully repeated for samples containing mixtures of two bacteria (Figure 53). Significantly, no false identifications were observed in any of the analyses (i.e., no signatures from the bacteria types that were absent from the serum), and no positives were recorded from blank samples (Figure 48A and Figure 49-52). Incidentally, a significant dispersion in correlation was observed (i.e., absolute SERS intensity per recognition event), which is attributed to the

size of the detected CFUs, ranging from single cells to larger colonies (Figure 55). Remarkably, all of the obtained concentrations were consistent with those found using conventional cell culture. However, there was a considerably lower standard deviation (Figure 49-52).

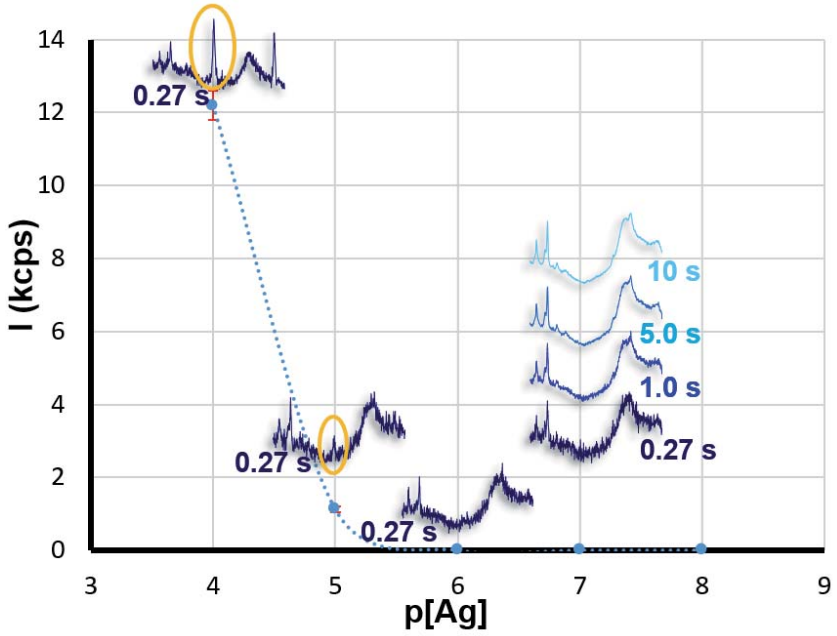

Figure 47. Optimization of the concentration of encoded NPs for background noise reduction. NP concentration was optimized to reduce the noise produced by the codes of dispersed NPs against the signal of decorated pathogens in the measurement area of the millifluidic chipset. SERS spectra of different dispersions of NPs arranged as a function of NP density (p is $-\log_{10}$ of the Ag molar concentration) are shown. A harmless, smooth, nearly constant background was produced by the chipset material. A SERS signal from the codes (circled features) can be clearly identified above 10^{-5} M in silver, but the spectrum disappears at 10^{-6} M. For that reason, a silver concentration of 10^{-7} M (~10^{7} NPs per mL) was used, for which no signal is achieved even after long acquisition times.

Selectivity and multiplexing of MODS are demonstrated in whole blood samples by contaminating blood simultaneously with *S. aureus*, *E. coli*, and *S. agalactiae* in different concentrations ranging from units to tens of CFUs per mL. It is important to note that blood samples spiked with microorganisms constitute a good model to emulate bacterial infection in actual patients. MODS analysis of this sample revealed all three pathogens (Figure 48A and Figure 54), while a statistical analysis of the results based

on three runs of the experiment (Figure 48C) determined their respective concentrations in excellent agreement with cellular cultures (Figure 48B and Figure 54). Incidentally, positive events varied in the degree of correlation, as expected from the bacterial diversity (Figure 55). Each MODS analysis took 13 min, which is a substantial reduction in time compared with cellular cultures (4-14 days).[15] These results further demonstrate the ability of MODS to accurately resolve pathogen concentrations in complex samples infected simultaneously with different pathogens at very different concentrations in a single pass, as illustrated in Figure 48 andFigure 54, where *E. coli* was present in a much lower density than *S. aureus* and *S. agalactiae.*

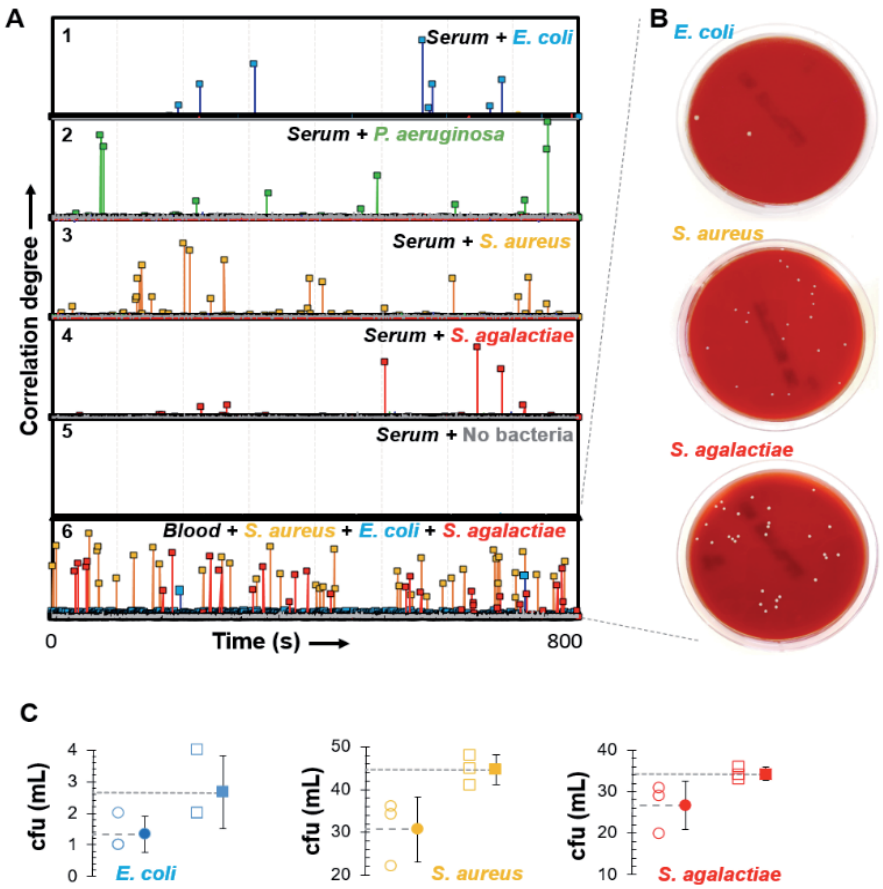

Figure 48. MODS performance for contaminated samples. (A) Correlation between a temporal series of spectra collected over 270 ms intervals and the SERS reference of the labeled NPs. The analyzed serum samples contain either one pathogen (1-4, see labels) or no pathogen (5, blank). Series 6 shows the result for a blood sample spiked with a combination of three different bacteria and concentrations (*S. aureus*, *E. coli*, and *S. agalactiae*). Large correlation values reveal the passage of an individual bacteria or CFU. (B) Cellular cultures (24-48 hours) for the microorganism inoculated in the blood samples (series 6). White spots correspond to CFUs. (C) Comparison of the bacteria concentrations (CFUs per mL) as determined by MODS (open squares) for the sample contaminated with three pathogens (series 6) versus traditional cultures (open circles). Averages over three runs of both MODS and culture experiments are shown by the corresponding solid symbols.

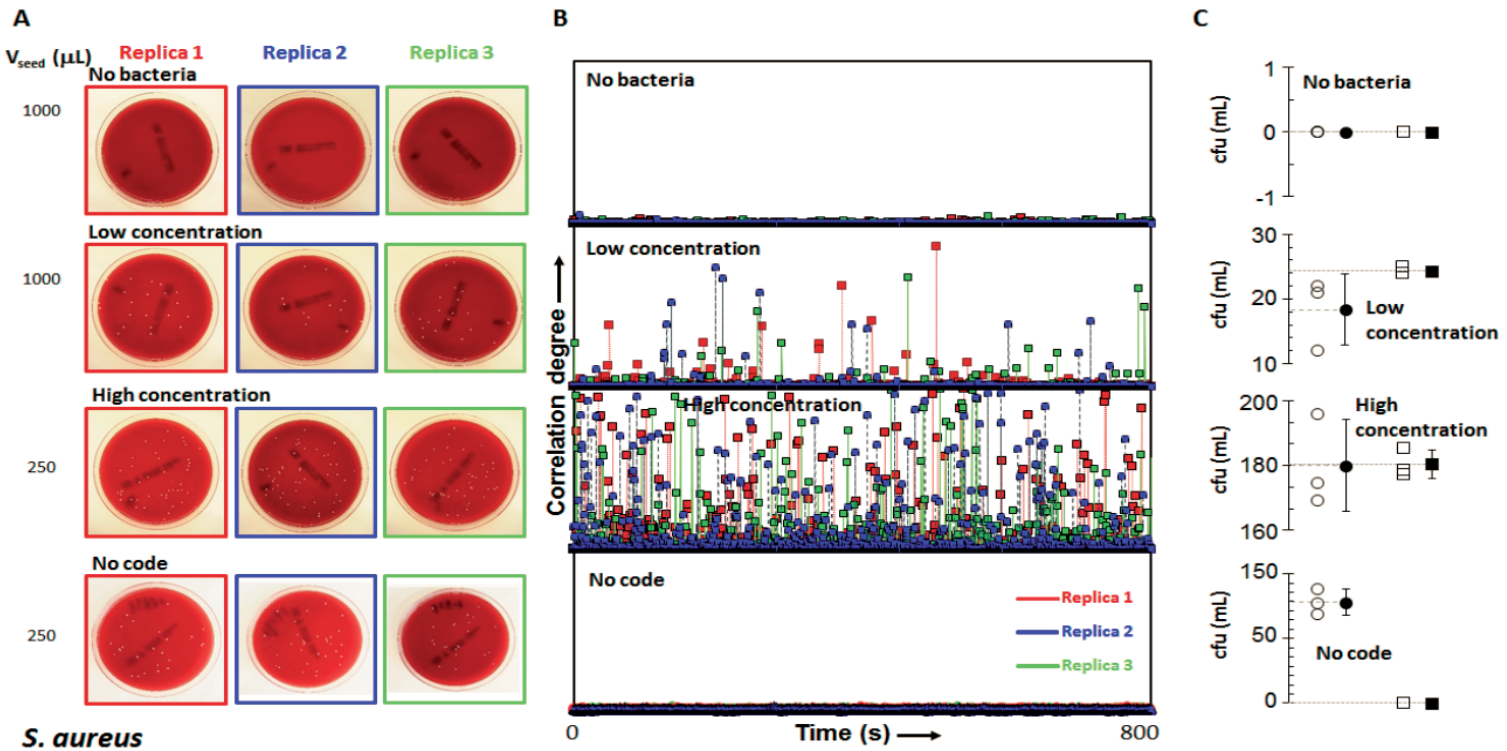

Figure 49. Results for serum sample spiked with *S. aureus* at different concentrations. (A) Cellular cultures. (B) Detection and quantification results obtained in the MODS device, from top to bottom: With no bacteria present, at low pathogen concentration, high concentration, and high concentration but without the encoded nanoparticle that identifies these bacteria. (C) Statistical comparison of bacteria concentrations (CFUs per mL) as determined by MODS (open squares) versus traditional cultures (open circles). Averages over three runs of both MODS and culture experiments are shown by the corresponding solid symbols.

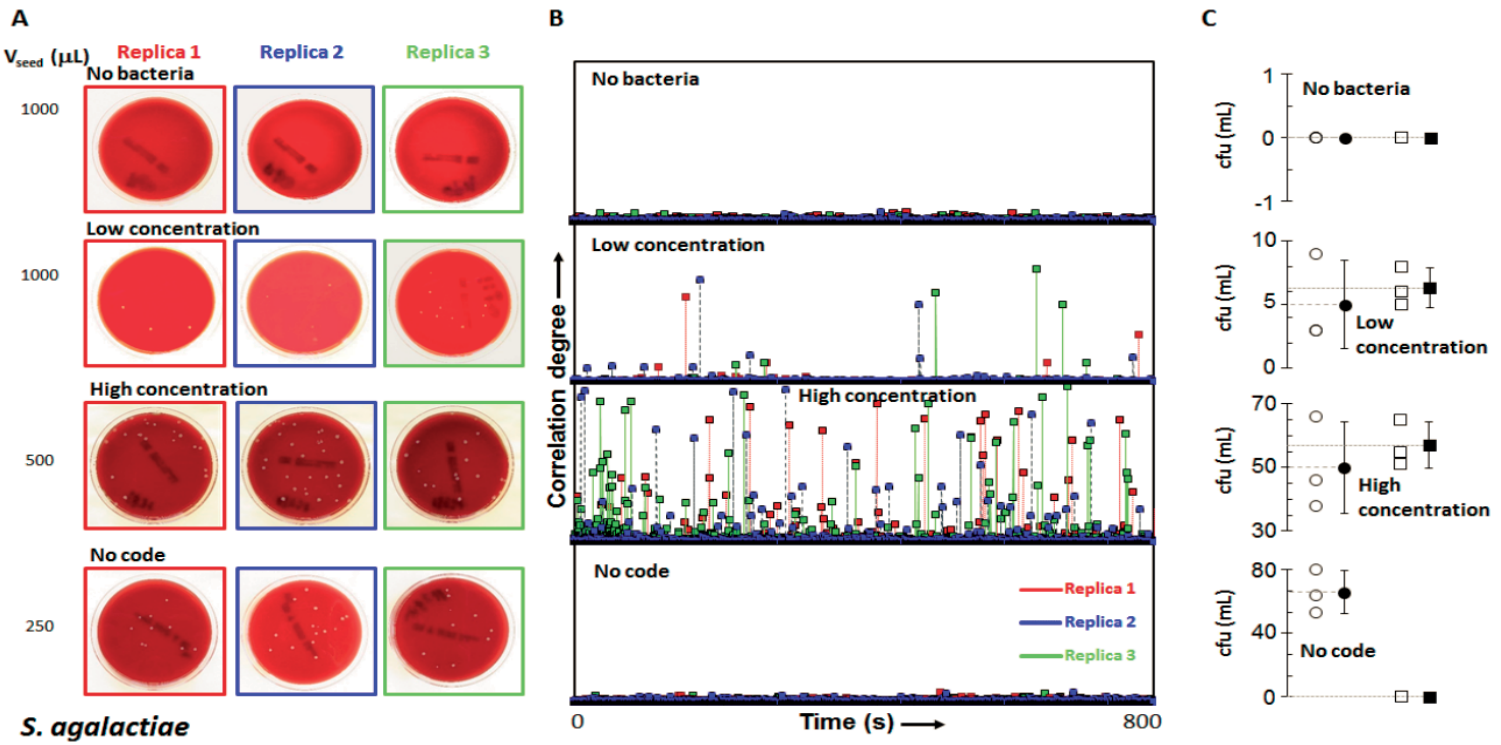

Figure 50. Results for serum sample spiked with *S. agalactiae* at different concentrations. (A) Cellular cultures. (B) Detection and quantification results obtained in the MODS device, from top to bottom: With no bacteria present, at low pathogen concentration, high concentration, and high concentration but without the encoded nanoparticle that identifies these bacteria. (C) Statistical comparison of bacteria concentrations (CFUs per mL) as determined by MODS (open squares) versus traditional cultures (open circles). Averages over three runs of both MODS and culture experiments are shown by the corresponding solid symbols.

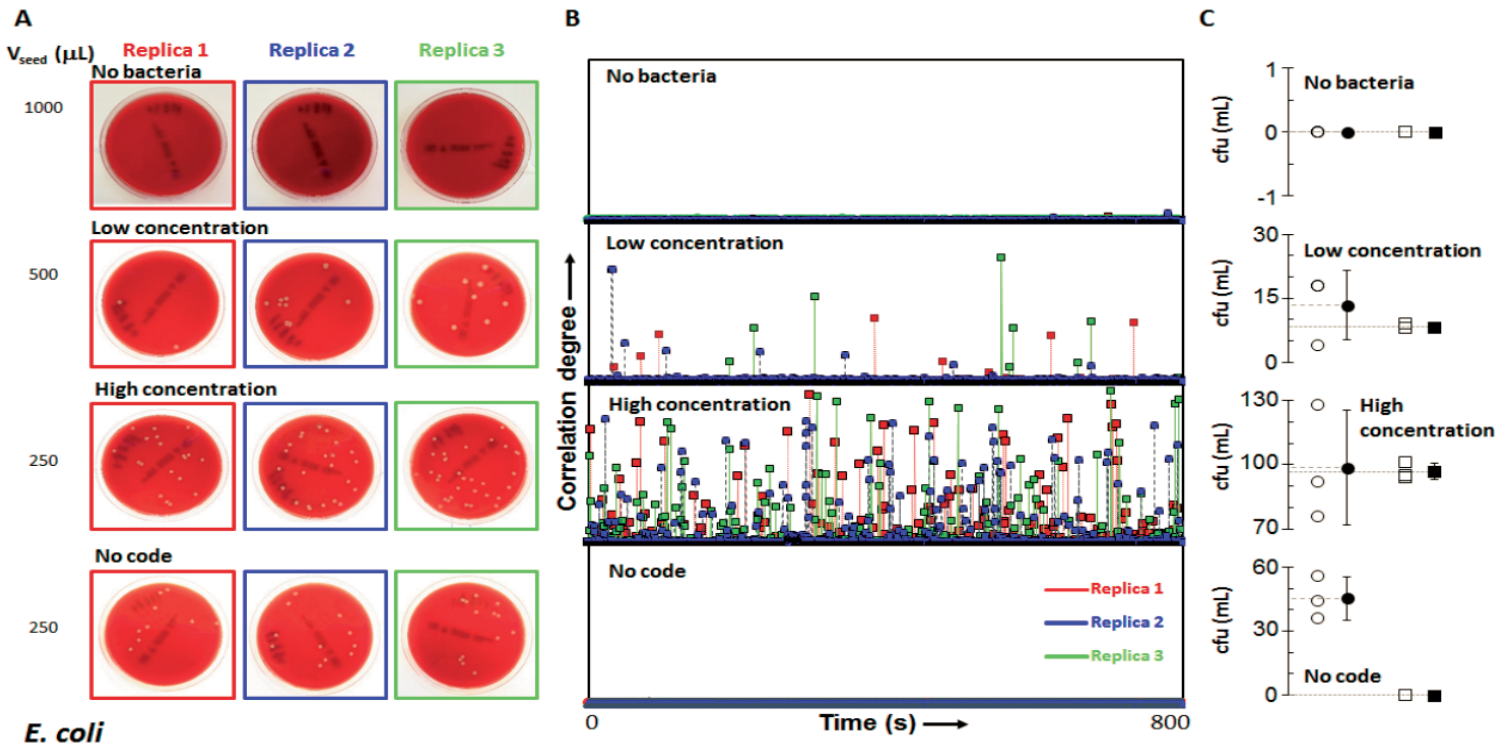

Figure 51. Results for serum sample spiked with *E. coli* at different concentrations. (A) Cellular cultures. (B) Detection and quantification results obtained in the MODS device, from top to bottom: With no bacteria present, at low pathogen concentration, high concentration, and high concentration but without the encoded nanoparticle that identifies these bacteria. (C) Statistical comparison of bacteria concentrations (CFUs per mL) as determined by MODS (open squares) versus traditional cultures (open circles). Averages over three runs of both MODS and culture experiments are shown by the corresponding solid symbols.

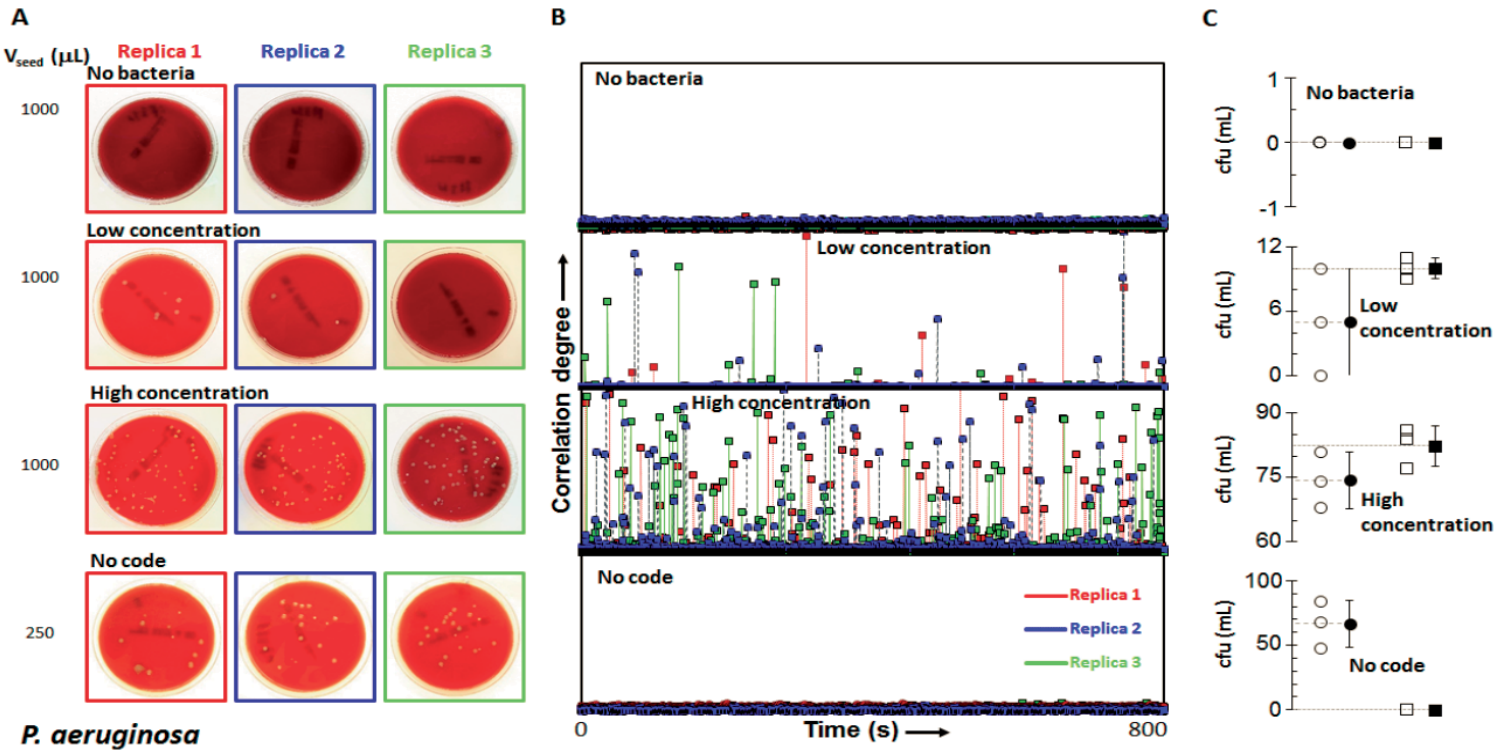

Figure 52. Results for serum sample spiked with *P. aeruginosa* at different concentrations. (A) Cellular cultures. (B) Detection and quantification results obtained in the MODS device, from top to bottom: With no bacteria present, at low pathogen concentration, high concentration, and high concentration but without the encoded nanoparticle that identifies these bacteria. (C) Statistical comparison of bacteria concentrations (CFUs per mL) as determined by MODS (open squares) versus traditional cultures (open circles). Averages over three runs of both MODS and culture experiments are shown by the corresponding solid symbols.

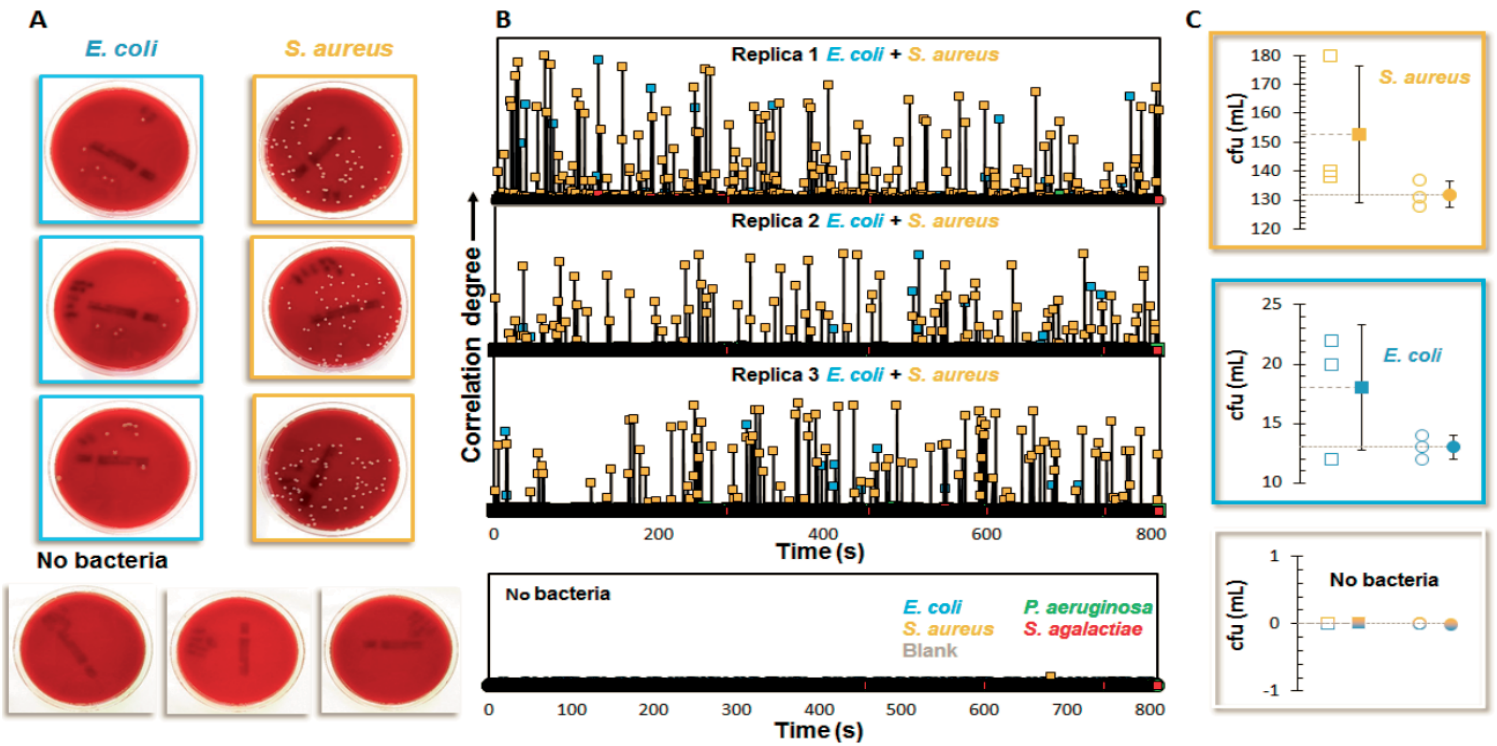

Figure 53. Results for serum sample spiked with both *E. coli* and *S. aureus*. (A) Cellular cultures for each bacterium (the volume seeded is 1 mL for *E. coli* and 0.5 mL for *S. aureus*). (B) Detection and quantification results obtained with MODS. (C) Statistical comparison of bacteria concentrations (CFUs per mL) as determined by MODS (open squares) versus traditional cultures (open circles). Averages over three runs of both MODS and culture experiments are shown by the corresponding solid symbols.

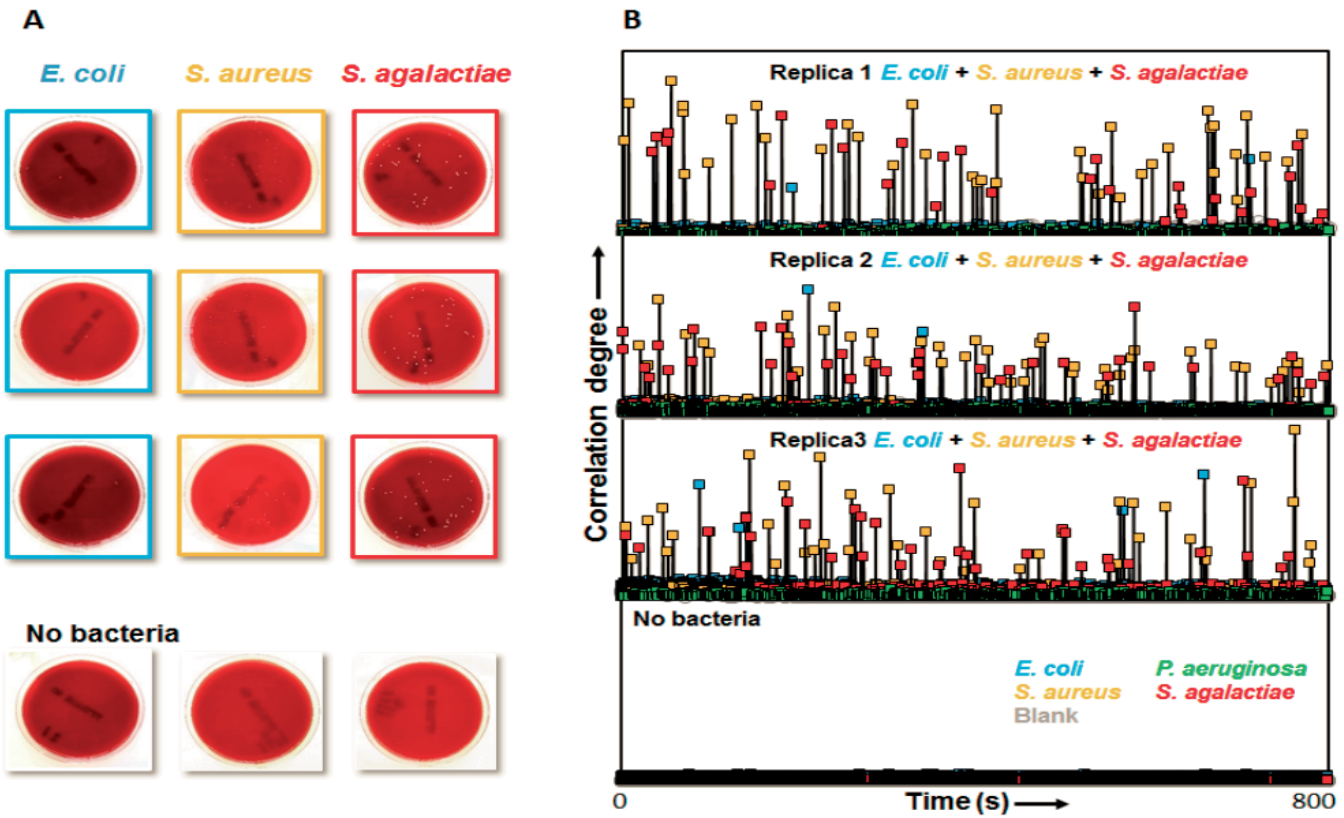

Figure 54. Blood sample spiked with *E. coli, S. agalactiae*, and *S. aureus*. (A) Cellular cultures for each bacterium (a volume 0.5 mL for *each*). (B) Detection and quantification results obtained in MODS. A statistical comparison of these results is presented in Figure 56C.

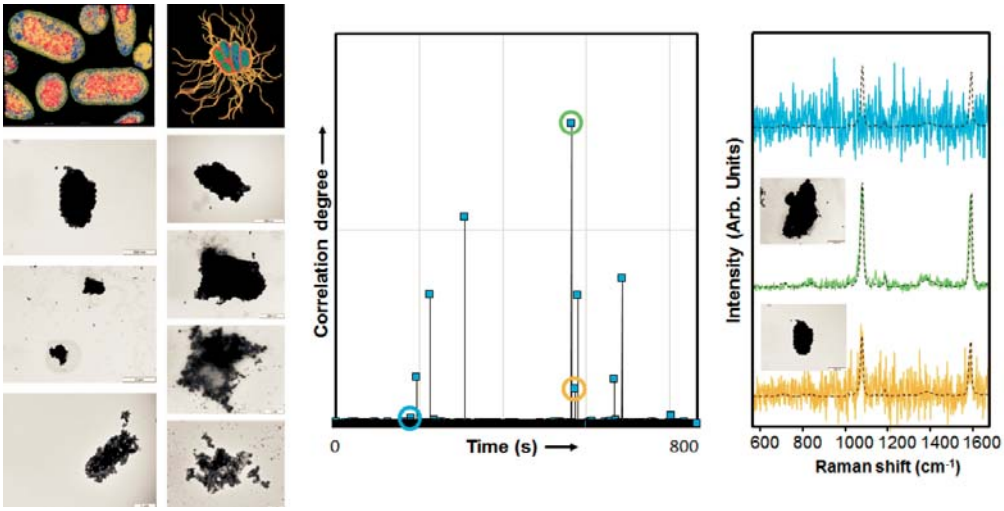

Figure 55. **Biodiversity of *E. coli*.** Left: TEM images of several single or clustered *E coli* CFU's coated with nanoparticles. Center: SERS detection results on the millifluidic MODS device for one of the samples of Figure 51 at low bacterial concentration. Right: Spectra corresponding to the events highlighted by circles in the previous plot, showing that the degree of correlation of the SERS spectra of the encoded particles strongly depends on the signal-to-noise ratio. Consequently, bigger clusters of bacteria give rise to a larger signal and higher correlation.

The kinetics of functionalized NP aggregation on the pathogen membrane is a key factor of MODS. As a representative example, after adding a large concentration of *E. coli* to the pool of five coded NPs (time 0), three distinct stages are found in the temporal evolution of the resulting SERS signal (Figure 56A). They are: (1) NP aggregation is initially very slow due to the relatively infrequent NP-bacteria encounters before sample and NPs fluids are fully intermixed, yielding just a slow increase in Raman signal; (2) diffusion eventually brings the NPs closer to the bacteria after ca. 300 s, resulting in more frequent encounters and a faster linear increase in SERS intensity; (3) the signal eventually reaches a plateau after ca. 700 s, consistent with previous literature,[249] indicating saturated coverage of the membrane. The latter stage is also affected by signal depletion produced by flocculation, as the increased weight of NP-covered CFUs pulls them away from the laser focus.

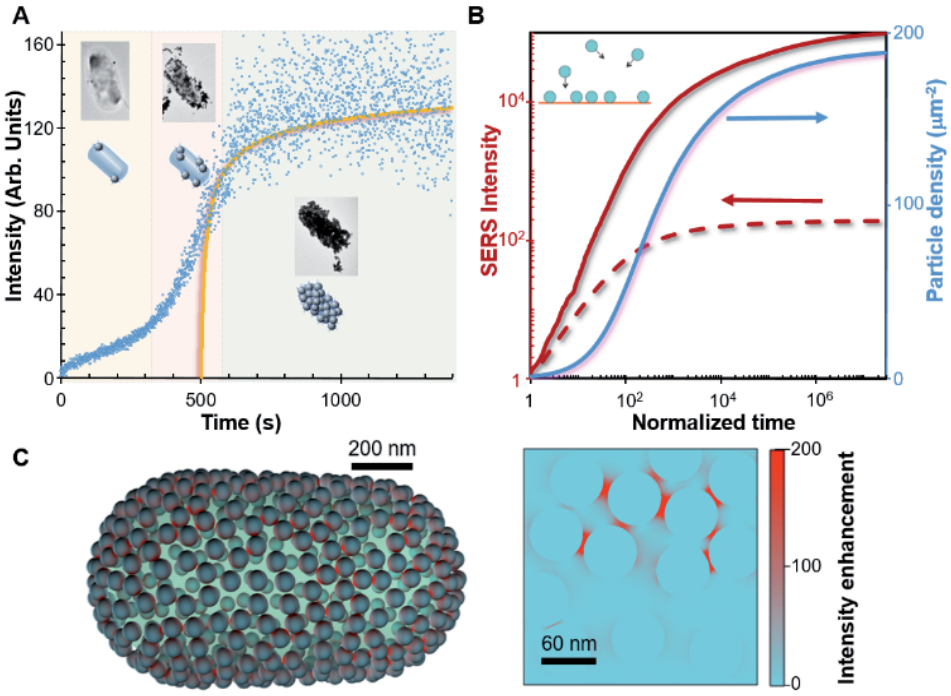

Figure 56. Kinetics of sensing enhancement through NP aggregation. (A) Kinetics of NP aggregation as measured through the time-dependent SERS signal (symbols) after adding *E. coli* to the mixture of encoded NPs. Solid curve: theory from (B). (B) Simulation of the temporal evolution of 60 nm Ag NP aggregation on the bacteria membrane produced by random NP-membrane encounters, resulting in a rapidly growing NP density (right scale) and SERS intensity (left scale, calculated per μm^2 of membrane area and normalized to the signal from an individual NP). The latter is given with (solid curve) and without (broken curve) inclusion of the effect of NP gap hot-spots. The time is normalized to the average delay interval between consecutive NP arrivals. The theory curve in A is scaled to 17.3 arrivals per second, as estimated from kinetic theory (see ESI). (C) Near-electric-field intensity in a rod-like individual *E. coli* covered with Ag NPs (top, intensity plotted on the NP surfaces) and detail of the array (bottom, intensity on a surface passing by the NP centers), revealing the formation of optical hots-pots. The intensity is averaged over light incidence directions and polarizations, the light wavelength is 785 nm, and the color scale is saturated to improve visibility.

Insight into these experimental results is provided by a Monte Carlo simulation of particle sticking (Figure 56B, right scale) that reveals a characteristic saturation at a NP random coverage ~60% of the maximum close-packed density.[147] A large occurrence of NP gaps takes place at high NP coverage. Although the laser wavelength is far from the NP plasmons (Figure 45 and Figure 58A), these gaps produce a dramatic enhancement

in the Raman signal (Figure 58B). Averaging over the gap distribution (Figure 57), an increase in SERS intensity by 3 orders of magnitude compared with non-interacting NPs was observed (cf. solid and broken red curves in Figure 56B, left scale). The signal resulting from positive CFU encounters was further amplified by the effect of attached NP accumulation. The modelled temporal evolution of the SERS signal agrees rather well with the measured kinetics (Figure 56A), without adjustable parameters other than the time after which the sample and NPs fluids were considered to be fully intermixed (~500 s).

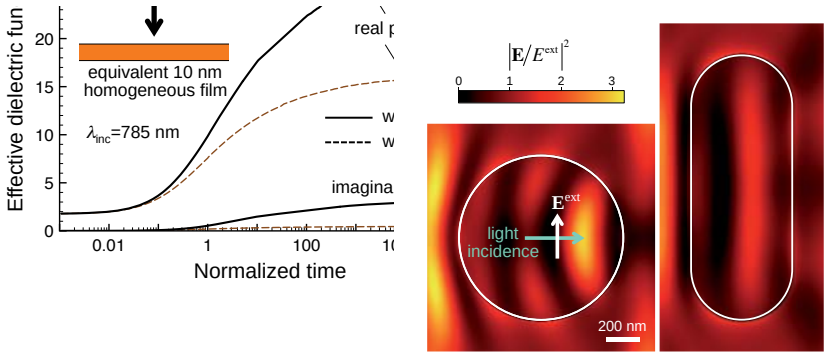

Figure 57. Near-field intensity in bacteria covered with nanoparticles**.** The NP coating was assimilated to a thin film with an effective dielectric function that is represented in the left plot. This dielectric function depends on the assumed film thickness (10 nm), but the calculated near field (right plot) is only mildly dependent on this parameter. The left plot shows that the dielectric function increases with the normalized time, as a result of the increase in particle density. Similar to the SERS enhancement (see Figure 56B), the gaps produce a large effect that create additional polarization that further increases the dielectric function. The near-field intensity shown on the right density plots is calculated by replacing the NPs with an equivalent homogeneous film that is conformably covering sphere-like and rod-like microbes, respectively, with the media inside and outside the film both described as water (Ɛ=1.77). The light wavelength is 785 nm. Based on the results of the left plot, the coating is modelled as a 10 nm thick layer with permittivity equal to 28 + 3i. The intensity is observed to undergo relatively weak variations due to the coating, and therefore, the bulk of the SERS enhancement is produced by hot-spots, as shown in Figure 56C.

Particle accumulation, gap formation, and the resulting SERS enhancement are thus pivotal to obtain intense signals from bacteria content well above the background of dispersed NPs. In support of this conclusion, the near-electric-field light intensity at 785 nm wavelength was

simulated for a rod-like structure mimicking an *E. coli* specimen (Figure 56C), which reveals large enhancements at the gaps between neighbouring NPs, accompanied by relatively weak modulations away from the gaps (Figure 57).

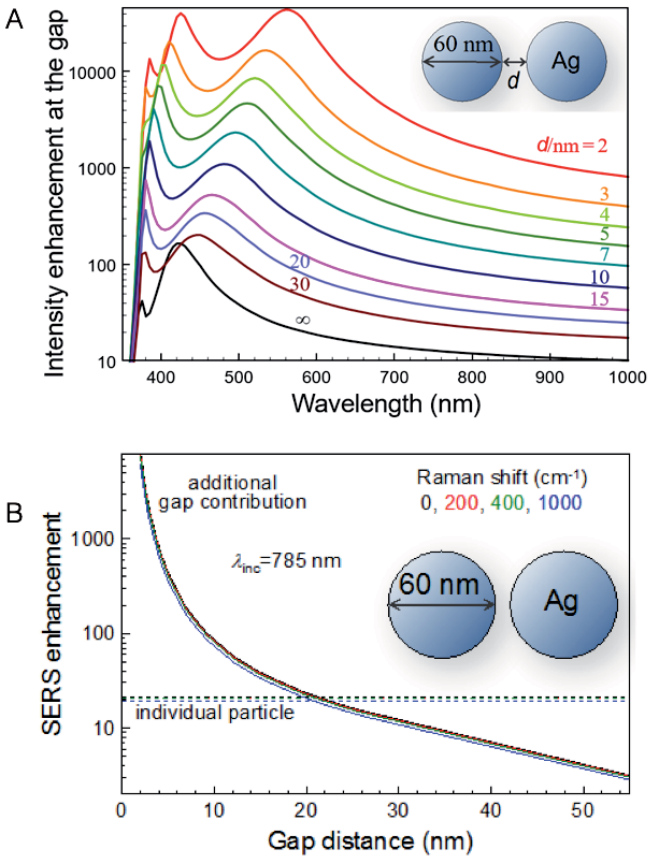

Figure 58. (A) Optical enhancement in Ag NP dimers. The electric field intensity enhancement |E/Eext|2 generated by a dimer of silver nanoparticles (60 nm diameter) embedded in water (ε=1.77) can be observed. The intensity is calculated at a distance of 1 nm from the surface of one of the particles in the gap region. Different surface-to-surface separations d are considered (see labels). A significant intensity enhancement of several orders of magnitude is still observable at the off-resonance light wavelength of 785 nm used throughout this work. (B) SERS enhancement produced by Ag NP dimers in aqueous solution. The increase in the SERS enhancement factor due to inter-particle interaction (solid curves) compared with the values for individual particles (dashed lines) as a function of gap distance is also shown. This quantity is averaged over randomly distributed sampling molecules placed 1 nm outside the metal surface. An average of over light polarizations and incidence directions is also carried out. The different Raman shifts under consideration (see labels) produce similar results because the incident light wavelength (785 nm) is not resonant with the particle plasmons (see A).

6.4 Conclusions

This work demonstrates the development of an infection diagnostic device (MODS) that can safely identify and quantify, with a sensitivity down to the single CFU, the presence of bacterial pathogens in biological fluids, specifically in serum and blood. The method can screen milliliters of liquid at a rate close to 0.1 mL/min. Although the concept was only confirmed with four bacterial agents, the detection method can be expanded to simultaneously identify many more of them by using the large number of available spectral codes and selective antibodies. Indeed, in section 4 we saw a method for the codification of nanoparticles with an extense library of molecules that shows an intense SERS signal.[206] Additionally, antibodies used in common clinical practice, such as those developed for immunology, can be readily incorporated in MODS. Furthermore, although MODS has been demonstrated here only with bacteria, the method has the potential to also analyze other microorganisms such as viruses, protozoa, fungus, and neoplastic cells in body fluids within minutes.

On the other hand, blood is one of the most complex biological fluids because it has a huge number of components. It can severely affect the physicochemical properties of the nanoparticles, perturb their colloidal stability,[250] as well as suppress the function of the surface biorecognition elements (antibodies).[251] Therefore, with the aim to prove the viability of the system, the microorganism detection optimization was performed using this medium (the worst case scenario). Accordingly, this detection method has the potential to be expanded to other biological fluids with great interest for PJI diagnosis, such as synovial fluid or liquified tissue.

Early diagnosis of PJI is a pressing clinical need. Even though MODS is not yet capable of discerning in between resistant and non-resistant microorganisms directly, it provides an accurate diagnosis in very short time as compared with all other currently available methods. Further, MODS cannot only guide in the choice of an accurate treatment for a given patient, but it can also monitor the effect of that treatment on the time evolution of the infection.

Late chronic infections in PJI are challenging to predict and typically caused by microorganisms that grow in biofilms.[11] Within biofilms, microorganisms are enclosed in a polymeric matrix, and organized in complex communities with structural and functional heterogeneity, resembling multicellular organisms.[12] In that case, microbes are protected from antimicrobial agents and host immune responses. Moreover, bacteria in biofilms are in a quiescence or dormancy state that may impact in their correct cell cultiring (producing false negatives). This problematic do not affect MODS because its methodology are not related with the cell replication.

With a growing population of patients at risk of developing PJI,[221] a highly sensitive and nonradioactive method for repeated monitoring should be clinically useful. Thus, joining a list of next-generation diagnostics (MALDI-TOF, lateral-flow, PCR), MODS aims to build toward early identification of infectious disease that may result in improved patient outcomes and decreased treatment toxicities.

7 Aptamers versus Antibodies: Diagnostics Optimization in Human Fluids

7.1 Introduction

In section 6 a translational alternative based on the use of SERS encoded plasmonic particles and microfluidics has been proposed for microorganism detection in biological fluids. In the discussed approach, the particles form a dense collection of electromagnetic hot-spots on the surface of the target bacteria allowing for an exponentially increase in SERS intensity as compared to the signal of free particles in solution. Quantification is achieved by passing the sample through a microfluidic device with a collection window where a laser interrogates and classifies each of the induced bacteria-nanoparticle aggregates in real time. The method was demonstrated using SERS encoded nanoparticles functionalized with antibodies as the chemoselective receptor to recognize bacteria in serum or blood. Although antibodies are an excellent option for the accurate recognition of specific targets, they are expensive to produce, delicate to handle, and rather large in size (a factor that limits the formation of active hot-spots). Over recent years, a new family of biomolecules (aptamers) has been developed as an efficient alternative to antibodies. Aptamers display similar or even larger target specificity[252] while providing key advantages in terms of stability, immunogenicity, facility of production, functionalization and reduced size.

Herein, the efficiency of the encoded nanoparticles upon funcionalization with either antibodies or aptamers against *S. aureus* was tested in order to improve bacteria recognition and quantification using MODS. *S. aureus* was choosen as the infectious agent because, apart from being the most causative microorganism of PJI, it is a common cause of community-acquired skin and soft tissue infections, osteomyelitis, endocarditis, pneumonia or bacteremia.[253] In addition, the experiments were performed in different human real samples (i.e., urine, blood, and pleural and ascites fluids) with the aim to confirm the colloidal stability and adequate identification.

7.2 Experimental section

7.2.1 Materials and methods

Dihydrated trisodium citrate (≥99.5%, $C_6H_5Na_3O_7{\cdot}2H_2O$), ethanol absolute (≥99.9%, EtOH), L-ascorbic acid (≥99.0%, AA), 4-mercaptobenzoic acid (≥99%, 4MBA), silver nitrate (≥99.9999%, $AgNO_3$), sodium hydroxide (≥98%, NaOH), *O*-(2-Mercaptoethyl)-*O*'-(2-carboxyethy) heptaethylene glycol (≥95.0%, HS-PEG-CO_2H), magnesium sulfate (≥98%, $MgSO_4$), *N*-(3-dimethylaminopropyl)-*N*'-ethylcarbodiimide hydrochloride (BioXtra, EDC), sodium chloride (BioXtra, ≥99.5%, NaCl), sodium docecyl sulfate (BioReagent, SDS), and Dulbecco's phosphate buffered saline (D8537, DPBS) were purchased from Sigma-Aldrich (Munich, Germany); 10X TBE buffer was acquired from Fisher Scientific; and *Staphylococcus aureus* antibody (MA1-10708, *S. aureus*), and thiol-modified *Staphylococcus aureus* aptamer[254] were purchased from Life Technologies. All reactants were used without further purification. Milli-Q water (18 MΩ cm^{-1}) was used in all aqueous solutions, and all glassware was cleaned with aqua regia before the experiments. *Staphylococcus aureus was* supplied by the Hospital Clínic y Provincial de Barcelona; the aseptic biological fluids (urine, blood, and pleural and ascites fluids) were supplied by the Hospital Univesitario Hm Madrid-Torrelodones. Personal and clinical data were recorded according to standard clinical procedures. All specimens were obtained with informed consent. The study was approved by the local Ethics and Clinical Research Committee.

7.2.2 Synthesis of citrate-stabilized spherical silver nanoparticles of ~60 nm diameter

Spherical silver nanoparticles (Ag NPs) of approximately 56 nm in diameter were produced by a modification of the previously reported protocol.[206] Briefly, 250 mL of Milli-Q water were heated to reflux under strong magnetic stirring. Once it boils energetically, a mixture containing ascorbic acid (250 µL, 0.1 M) and trisodium citrate (1.7 mL, 0.1 M) was

added. After 1 minute, a solution containing $AgNO_3$ (496 µL, 0.1 M) and $MgSO_4$ (392 µL, 0.1 M), previously incubated for 5 min at room temperature, was injected into the reaction vessel under vigorous stirring. Boiling and stirring were continued during 1 h to ensure the precursors reduction. During this time, the color of the solution quickly changed from colorless to yellow, and gradually into dark orange. Finally, NPs were cleaned with centrifugation (5400 r.p.m., 20 min) and redispersed in Milli-Q water, to a final $[Ag^0] = 5\times10^{-4}$ M.

7.2.3 Silver nanoparticles codification and antibody conjugation

In order to provide colloidal stability to Ag NPs during the encoding process and antibody conjugation, 15 mL of the as produced spherical silver nanoparticles were functionalized with a small amount of HS-PEG-CO_2H. To this end, a solution containing HS-PEG-CO_2H (7.5 mL, 1.83 µM in EtOH) and 4MBA (7.5 mL, 5.48 µM in EtOH) was prepared. This solution was then rapidly added to silver colloids ($[Ag^0] = 5\times10^{-4}$ M) and sonicated during 30 s (the number of molecules nm^{-2} was 1 for HS-PEG-CO_2H and 3 for 4MBA). Subsequently, NaOH (150 µL, 0.23 M) was added to the mixture under vigorous stirring and sonicated for 30 s. 1 h later, Ag NPs were cleaned twice by centrifugation (4.200 r.p.m., 12 min) and redispersed in Milli-Q water to achieve a final $[Ag^0] = 5\times10^{-4}$ M. Afterwards, DPBS (200 µL) and EDC (20.3 µL, 250 nM in DPBS) were added to the colloidal dispersion (1 mL, [NPs] = 92.8 pM) in order to conjugate the antibody to the nanoparticles, the mixture was shaken for 5 min at room temperature, and then the antibody solution was added (0.7 µL, ~ 7.3 µM). The resulting mixture was shaken for 2 h at room temperature, then cleaned twice with centrifugation to remove the excess of unreacted EDC and antibody (3000 rpm, 10 min), and redispersed in DPBS/Milli-Q water (1:3). The concentration of the Ab-modified Ag NPs solution was measured, adjusted to 18.6 pM ($[Ag^0] = 1\times10^{-4}$ M), and the solution was stored at 4 °C.

7.2.4 Silver nanoparticles codification and aptamer conjugation

5′-alkyl-thiol–modified *S. aureus* aptamer (1.5 mL, 3.1 nM) was added to a 92.8 pM Ag NPs solution (0.5 mL, $[Ag^0] = 5\times10^{-4}$ M), and the mixture was shaken overnight at room temperature. Then, 20 μL of 1% SDS and 50 μL of 10X TBE were added, and the resulting solution was shaken overnight at room temperature. The following morning, sodium chloride was added 5 times at 1 h intervals to a final concentration of 20, 40, 60, 80, and 100 mM. At 1 h after the last addition, 2.2 μL of a 100 μM 4MBA solution (0.4 molecules nm^{-2}) were added, and the mixture was shaken overnight at room temperature. Finally, the NPs were cleaned by centrifugation (3000 r.p.m., 10 min) and redispersed in Milli-Q water. The concentration of the aptamer-modified Ag NPs solution was measured, adjusted to 18.6 pM ($[Ag^0] = 1\times10^{-4}$ M), and the solution was stored at 4 °C.

7.2.5 Nanoparticle characterization

UV–vis spectra were recorded using a Thermo Scientific Evolution 201 UV–vis spectrophotometer. The silver concentration for Ag NPs colloids was calculated with the Lambert−Beer law using an extinction coefficient of 6.61×10^{10} M^{-1} cm^{-1}.[182,206] Electron micrographs were recorded with a transmission electron microscopy (JEOL JEM-1011 operating at 80 kV) and an environmental scanning electron microscopy (JEOL 6400) for the structural characterization of the samples. SERS spectra were collected in backscattering geometry with an in-house Raman system (Technospex, Singapur) equipped with a CCD detector and a macrolense. The spectrograph used a high resolution grating (1200 grooves cm^{-1}) with additional band pass filter optics. Excitation of the sample was carried out with a 785 nm diode laser line, with acquisition times of 0.4 s and power at the sample of 500 mW.

7.2.6 Microfluidic device manufacturing

The microfluidic device was fabricated following the same procedure as specified in section 6.2.7 (page 117). However, the dimensions of the microchannel were modified to 600 μm-width, 2 mm-depth, and 50 mm-length.

7.2.7 Bacterial samples

Bacteria were inoculated in enriched thioglycollate medium (BBL), incubated at 37 °C for 18 h, and then diluted with saline solution (0.9% NaCl). Next, the required volume of bacterial solution was diluted into serum or biological fluids in order to reach the desired final concentration. Then, the modified Ag NPs, with antibody or aptamer of *Staphylococcus aureus*, were added to the bacterial solutions at a concentration of 10 μL (10^{-4} M Ag^0)/mL of sample, in the case serum and 1 mL (2×10^{-6} M Ag^0)/mL of sample for the biological fluids. To verify the final bacterial concentration per sample, three replicates of each solution were spread in agar-blood plates and incubated for 24-48 h at 37 °C. After that time, the number of colonies in each plate was counted in order to calculate their concentration of CFUs per mL.

7.2.8 Measurement system setup

The microfluidic device was placed onto the stage of the system and appropriately aligned. Inlet and outlet were connected to a syringe and a waste container, respectively, via 0.8 mm-diameter polytetrafluoroethylene (PTFE) and 1.1 mm-diameter tygon tubes. The syringe was pre-charged with the sample and nanoparticles. A standard syringe pump (NE-1000, New Era Pump Systems, Inc.) was used to push the sample at a flow rate of 6 mL/h. The laser (785 nm, 500 mW) was focused with a macrolense providing an efficient spot of 0.6 mm. The scan collection time was set to 400 ms per spectrum, providing an acquisition speed of 1.5 mm/s (for a flow speed of 1.48 mm/s), which results in an evaluation speed of 10 min per mL of sample, during which 1500 scans are obtained. Data

deconvolution was carried out by principal component analysis and classical least squares using the Wire 4.1 software.

7.3 Results and discussion

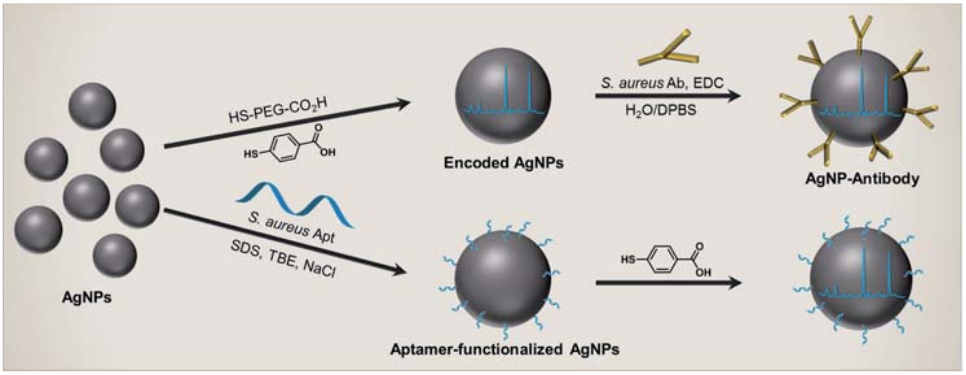

Figure 59. Schematic representation of the nanoparticle SERS encoding and functionalization with antibodies and aptamers.

Although antibodies and aptamers fulfill the same bio-recognition function, their chemical nature is significantly different. Thus, two different protocols were developed for preparing SERS tags for the efficiency comparison (Figure 59). First, silver nanoparticles were prepared following a modification of the previously reported protocol in section 6.2.3. In this case, the obtained silver nanoparticles were stabilized with a small amount of HS-PEG-CO_2H prior to the codification instead of using MUA as the stabilizing agent. This molecule, like MUA, provides particle stability with both a long chain (steric repulsion) and a final carboxylic group (electrostatic repulsion). However, HS-PEG-CO_2H has a longer chain than MUA and therefore provides higher nanoparticle stability (Figure 60A and B). In contrast to the HS-PEG_{5000} (commented on section 4), HS-PEG-CO_2H also allows for an easy diffusion of the Raman labels onto the metallic surface thanks to his not branched nature. Besides, HS-PEG-CO_2H was used to maximize the SERS signal (Figure 60C) because a less molecular ratio (1:3) between HS-PEG-CO_2H and the encoding agent (4MBA) was needed to still preserve the colloidal stability of the NPs in saline media. This stability of the colloidal systems in saline media was monitored by UV-

Vis-NIR spectroscopy (Figure 60A and B). NaCl concentration for this study was set to be similar to that of biological fluids like blood and serum. At [NaCl] = 145 mM the extinction spectra of Ag NPs@HS-PEG-CO_2H/4MBA exhibit the characteristic LSPR of monodisperse spherical silver nanoparticles in suspension (Figure 60A). On the other hand, a small shoulder at ca. 600 nm was observed for the Ag NPs synthesized via the MUA approach, indicating a minor formation of nanoparticle aggregates (Figure 60B).

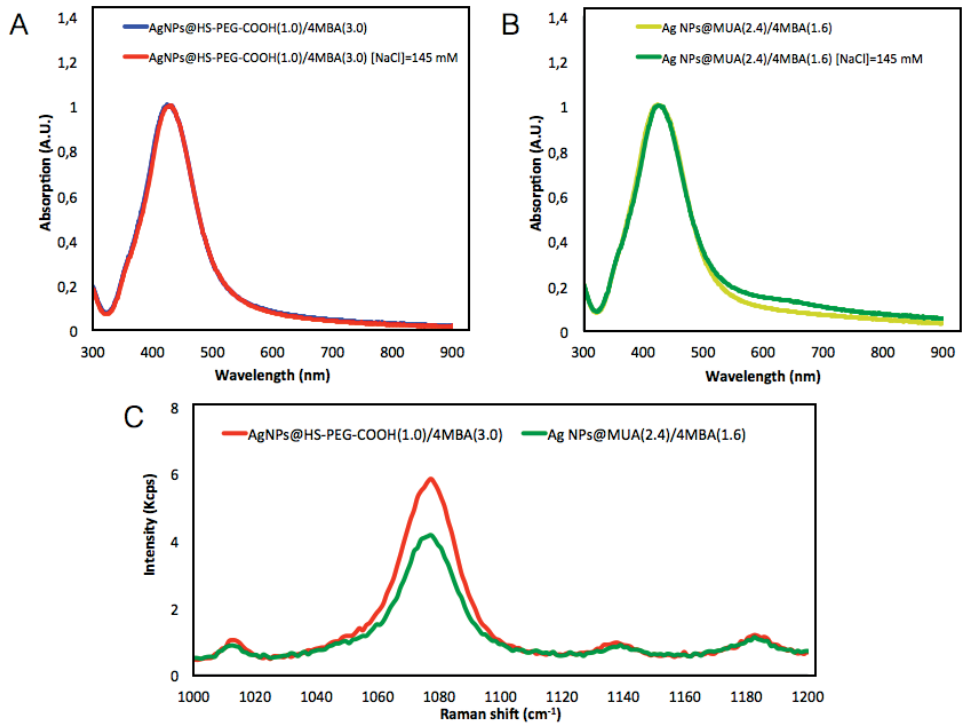

Figure 60. Nanoparticle stability in saline media. (A) Localized surface plasmon resonances of (blue line) Ag NPs stabilized with 1.0 molecules nm^{-2} of HS-PEG-CO_2H and encoded with 3.0 molecules of 4MBA in Milli Q water and (red line) Ag NPs stabilized with 1.0 molecules nm^{-2} of HS-PEG-CO_2H and encoded with 3.0 molecules of 4MBA in saline media ([NaCl] = 145 mM). (B) Localized surface plasmon resonances of (yellow line) Ag NPs stabilized with 2.4 molecules nm^{-2} of MUA and encoded with 1.6 molecules of 4MBA in Milli Q water and (green line) Ag NPs stabilized with 2.4 molecules nm^{-2} of MUA and encoded with 1.6 molecules of 4MBA in saline media ([NaCl] = 145 mM). All the UV-Vis spectra were acquired 2 h later the NaCl addition. (C) Comparison of the SERS efficiency of encoded nanoparticle suspensions synthesized via HS-PEG-CO_2H and MUA approaches ([Ag] = 0.1 mM). Ag NPs@HS-PEG-CO_2H/4MBA shows 40.3% more Raman Intensity than Ag NPs@MUA/4MBA.

Antibody coupling to the nanoparticles was also achieved using EDC as activating agent to form a peptide bond between the carboxylic group of the HS-PEG-CO_2H and an amine group of the antibody. In the case of the aptamer functionalized nanoparticles, a 5′-alkyl-thiol–modified *S. aureus* aptamer was first self-assembled onto the silver surfaces followed by the subsequent encoding with 4MBA. The concentration of 4MBA was set to be similar to that of the particles functionalized with antibodies. In this case, no extra stabilizing agents were necessary as the aptamer surface modification maintains the colloidal integrity of the particles. Figure 61 shows the localized surface plasmon resonance (LSPR), transmission electron microscopy (TEM) images, and SERS response of the particles encoded with 4MBA and functionalized with either antibodies or aptamers. Notably, both optical and physical characteristics of all the materials remain similar, without appreciable changes in between samples.

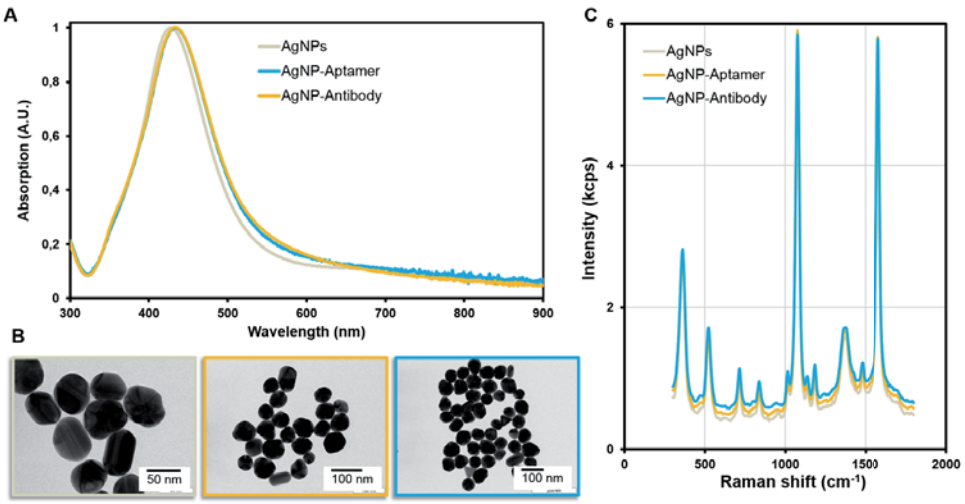

Figure 61. (A) Localized surface plasmon resonances, (B) representative TEM images, and (C) SERS response of the SERS encoded silver particles as prepared and after functionalization with either antibodies or aptamers.

To test the efficiency of antibodies vs aptamers functionalization, an experiment comprising a serum solution spiked with around 7×10^3 CFUs/mL of *S. aureus* (Figure 62A) was designed. This solution was mixed with the same volume (10 mL, 10^{-6} M Ag^0) of SERS encoded Ag NPs, either uncoated or functionalized with antibodies or aptamers. The resultant

solutions were passed through MODS (Figure 44). Figure 62B shows the results for the three materials. The 4MBA ring breathing feature at 1078 cm^{-1} was selected as a spectral marker to monitor the SERS intensity. First, the SERS encoded Ag NPs lack of surface biorecognition elements does not show any detectable SERS signal. Conversely, both antibody- and aptamer-functionalized particles yield intense SERS signals that increase with time up to ca. 800 s, when a plateau is reached. The comparison of aptamers with antibodies displays, however, notable differences. First, aptamers exhibit much larger affinity for bacteria than antibodies. Second the final SERS intensity registered for aptamers (at t = 800 s) is around 40% greater than that for antibodies. To understand this behavior, samples of bacteria with nanoparticles were studied with electronic microscopy at different incubation times (Figure 62C). At t = 0 s, both samples show low interaction with nanoparticles. At t = 400 s, the number of nanoparticles retained on the bacteria increases, but to a much larger extent in the case of aptamers, thus resulting in stronger SERS signals. Such a discrepancy can be attributed to a larger affinity constant of the overall ensemble of aptamer molecules bound to the metallic surface as compared with the antibody. Notwithstanding, aptamers can be easily functionalized/modified without any loss of their activity and, then, their conjugation on the nanoparticle surface can be directed to yield a conformation suitable for their efficient interaction with the target entity. In contrast, the functionalization of antibodies may affect their biological response and, further and more importantly, the coupling protocol always leads to a random orientation of the protein on the nanoparticle surface. As a result, a portion of the antibody molecules can be coupled through sensitive amino groups inactivating their binding site (i.e., paratope).[255] Finally, at t = 800 s, the TEM images show a similar coating of particles for both aptamers and antibodies, while aptamer-modified SERS encoded nanoparticles still yield a remarkable larger SERS intensity. This may be ascribed to the smaller aptamer size,[256] which allows the formation of smaller interparticle gaps at the bacterial surface, leading to an overall increase of the electromagnetic energy generated at the hot-spot.

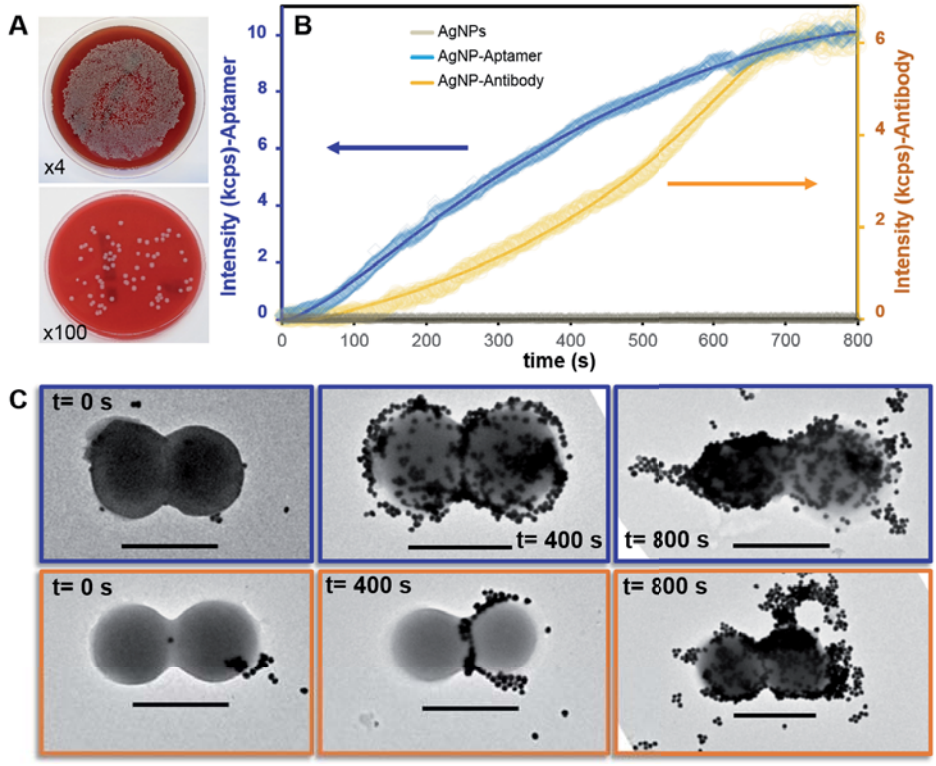

Figure 62**.** (A) Results for the bacterial culture of the *S. aureus* solution (250 µL, top, and 10 µL, bottom) used to test the efficiency of the interaction of the Ag NPs functionalized with antibodies or aptamers. (B) Comparison of the SERS intensity of the band at 1078 cm^{-1} (ring breathing of 4MBA) and (C) TEM images of *S. aureus* as a function of the incubation time with the SERS encoded silver particles functionalized with either aptamers (blue) or antibodies (orange). Scale bar: 1 µm.

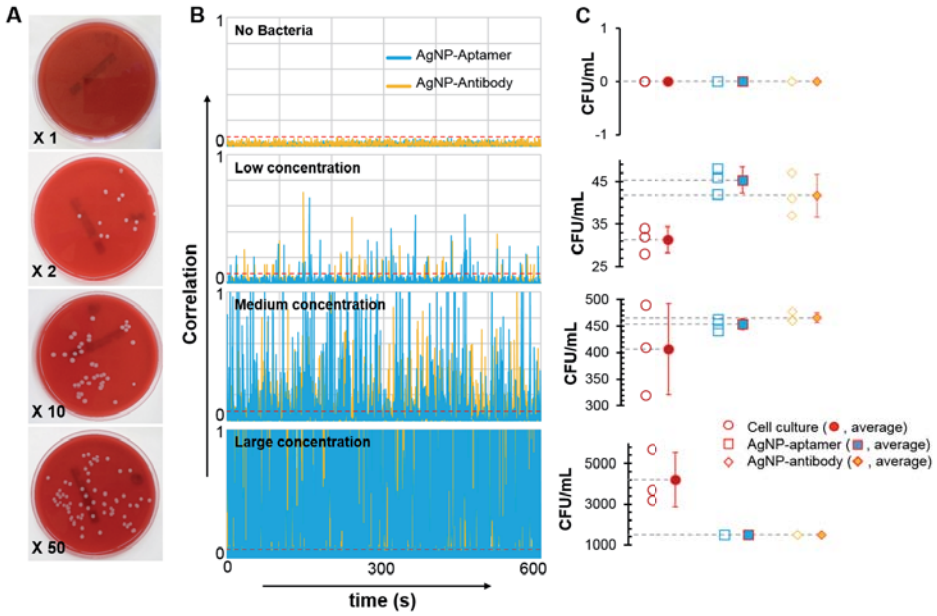

Figure 63. Quantification of *S. aureus* through (A) bacterial culture and (B) the microfluidic optical system. The number in the bacterial culture images indicates the volume of initial solution spread in the blood agar plates (×1, 1 mL; ×2, 500 μl; ×10, 100 μL; and ×50, 20 μL). Conditions for the microfluidic optical device were: flow speed 6 mL/h with acquisition times of 0.4 s. Y axis represents the similarity of the obtained SERS spectrum of the sample at a given time with the reference SERS spectrum of 4MBA obtained from a concentrated solution (10^{-3} M Ag^0) of 4MBA encoded nanoparticles. (C) Comparison of the bacteria concentrations (CFUs per mL) as determined by traditional cultures (open circles) and nanoparticles with aptamers (open squares) or antibodies (open diamonds). Averages over three cultures or runs are shown by the corresponding solid symbols.

Figure 63 shows the results obtained for serum samples infected with *S. aureus* at different concentrations, either measured with regular bacterial culture (48 h of incubation, Figure 63A) or via the optical system (Figure 63B). As in the previous case, 10 μL (10^{-4} M Ag^0) of nanoparticles per mL of the sample were added. After incubating the samples for 15 min, several milliliters of each solution were passed through the microfluidic optical device at a flow rate of 6 mL/h. Both, antibody and aptamer functionalized nanoparticles offer similar results (Figure 63C). When no bacteria were present, no detectable signal is registered. That is consistent with the outcome of the bacterial culture analysis. At low or moderate

concentrations of bacteria, both give rise to slightly larger quantification than bacterial cultures. This difference is not significant for the clinical diagnosis, as these values are in the same order of magnitude. In contrast, the optical-based device showed a continuous positive for high bacteria concentrations (Figure 63B) and the quantification was underestimated. That underestimation was probably due to the temporal resolution (1500 scans per sample). A possible solution for this inconvenience is the dilution of the sample to a bacterial concentration below the temporal resolution. This problem is also not significant for the clinical diagnosis because this concentration range is clearly pathological.

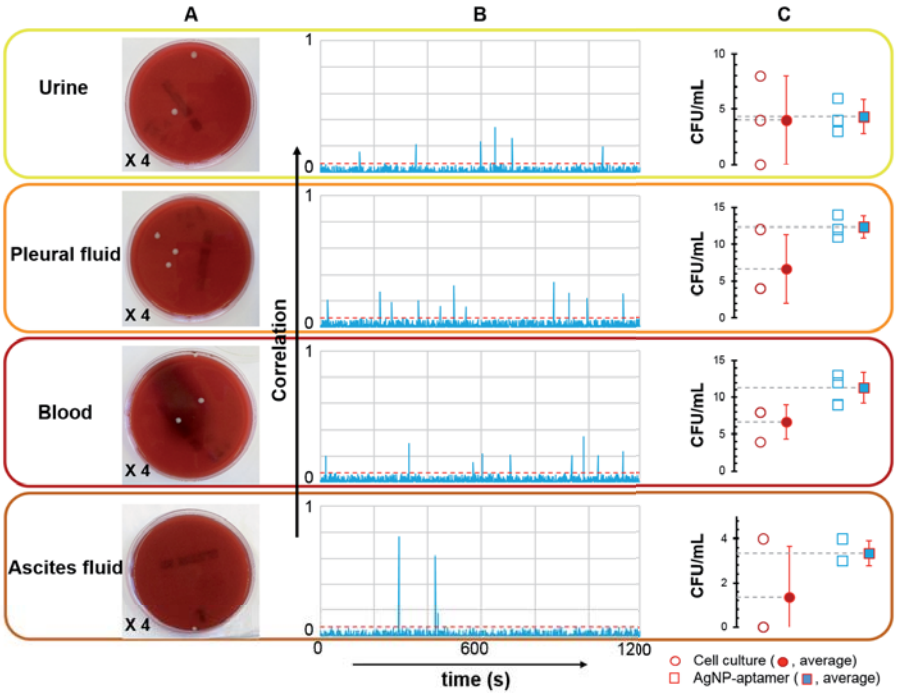

Figure 64. Quantification of *S. aureus* in different biofluids through (A) bacterial culturing and (B) our microfluidic optical system. The number in the bacterial culture images indicates the volume of initial solution spread in the blood agar plates (×4, 250 μL). Conditions for the microfluidic optical device were: flow speed 6 mL/h with acquisition times of 0.4 s. The Y axis represents the similarity of the obtained SERS spectrum of the sample at a given time with the reference SERS spectrum of 4MBA obtained from a concentrated solution (10^{-3} M Ag^0) of 4MBA encoded nanoparticles. (C) Comparison of the bacteria concentrations (CFUs per mL) as determined by traditional cultures (open circles) and nanoparticles with aptamers (open squares). Averages over three cultures or runs are shown by the corresponding solid symbols.

Taking into account the results described above, SERS encoded nanoparticles conjugated with aptamers as optimal substrates were selected for detecting *S. aureus* in several relevant human fluids. These fluids are aseptic in healthy conditions, and infection for most of them (i.e., blood, and pleural and ascites fluids) is defined by the presence of just one CFU per mL. Thus, the biological samples were spiked with a very low concentration of bacteria. Figure 64 shows the results obtained after infecting different human fluids with *S. aureus*. As in the case of serum, both bacterial culture and the optical system offered similar quantification results. However, there was a dramatic difference in detection time: 48 h for the bacterial culture vs 20 min for the microfluidic SERS-based device.

7.4 Conclusions

Herein, the advantages of using aptamers versus antibodies were demonstrated for the rapid ultrasensitive quantification of *S. aureus* using a microfluidic optical device. Interestingly, aptamers exhibit much greater affinity to bacteria than antibodies. Besides, the final SERS intensity registered for aptamer funcionalized encoded nanoparticles was also larger. This may be attributed to the easily funcionalization of the aptamers onto the metallic surface (without any loss of their activity), yielding a suitable conformation for an efficient interaction with the target microorganism. In contrast, the functionalization of antibodies may affect their biological response due to a random orientation of the protein on the nanoparticle surface, inactivating the binding site of a portion of antibodies.

On the other hand, the colloidal stability and the adequate identification of *S. aureus* were confirmed in different human real samples (i.e., urine, blood, and pleural and ascites fluids). In addition, similar approach can be applied for the determination of other microorganisms.

8 General conclusions

This work was mainly oriented towards achieving a detection and quantification method for bacteria in real time and in a multiplexed manner to improve the diagnosis of PJI. To conclude, the main goals of this work can be summarized as follows:

1. Highly efficient SERS encoded nanoparticles were obtained using an inexpensive and scalable synthetic protocol. The method relied on the functionalization of plasmonic nanoparticles with a submonolayer of MUA that provided high colloidal stability and a convenient surface chemistry for further antibody bioconjugation (using a carmodiimide crosslinking reaction). In addition, the presented synthetic strategy was successfully applicable to a wide variety of Raman codes and outstandingly scalable up to two liters without affecting the final properties of the encoded structures. The SERS efficiency of the so-fabricated encoded nanoparticles displayed a performance from 2 to 140 times greater than the corresponding particles prepared via the common methods.

2. Polystyrene micro-cores with a dense external layer of interacting nanoparticles were used as a bacteria model to simulate the SERS signal when a conjunction of SERS tags specifically agglutinate on a microorganism's membrane. In that situation, the SERS signal is dominated by the generation of interparticle-gap resonances. The results showed how the enhancing ability of the hybrid substrates is strongly determined by the size and composition of the individual nanoparticles, and the dependency to the selected excitation wavelength. Relative to the size of the nanoparticles, 50-70 nm in diameter resulted the best choice for 633 and 785 nm excitation wavelengths. On the other hand, the SERS performances of silver and gold

nanoparticles were similar under a 785 nm excitation wavelength (in the near-infrared spectral window that is normally used to avoid photochemical damage in biological samples).

3. In order to develop a fast, accurate, and inexpensive method for PJI diagnosis, a device based on antibody-modified plasmonic nanoparticles, microfluidic channels and SERS spectroscopy was designed. This device for can safely identify and quantify, with sensitivity down to the single CFU, the presence of bacterial pathogens in a wide spectrum of biological fluids (i.e., urine, blood, and pleural and ascites fluids). The concept was only confirmed with four bacterial agents, but the detection method can be expanded to simultaneously identify more pathogens by using the large number of available spectral codes and selective antibodies. Even though MODS is not yet capable of discerning directly in between resistant and non-resistant microorganisms, it provides an accurate diagnosis in very short time as compared with all other currently available methods (i.e., culturing, MALDI-TOF, PCR, ELISA). Additionally, it can monitor the effect of the treatment on the time evolution of the infection.

4. Although antibodies are an excellent option for the accurate recognition of specific targets, they are delicate to handle and large in size (a factor that limits the formation of active hot-spots). In this work, the advantages of using aptamers versus antibodies were demonstrated for the rapid ultrasensitive quantification of *S. aureus*. Aptamers provided key advantages in terms of stability, immunogenicity, facility of production, functionalization and reduced size. Accordingly, *S. aureus*-modified SERS encoded nanoparticles produced higher SERS signal than antibody-modified particles when they were attached to bacteria's membrane.

9 References

1. Romm, S. Arms by design: from antiquity to the Renaissance. *Plast. Reconstr. Surg.* **84,** 158–163 (1989).

2. History of Hanger Orthopedic Group, Inc. – FundingUniverse. Available at: http://www.fundinguniverse.com/company-histories/hanger-orthopedic-group-inc-history/. (Accessed: 7th July 2016).

3. Walk Like an Amputated Egyptian | DiscoverMagazine.com. Available at: http://discovermagazine.com/2001/apr/breakwalk/. (Accessed: 26th July 2016).

4. Hall, M. J. *et al.* National hospital discharge survey: 2007 summary. *Natl Health Stat Rep.* **29,** 1–20 (2010).

5. Robertsson, O. *et al.* Knee arthroplasty in Denmark, Norway and Sweden. A pilot study from the Nordic Arthroplasty Register Association. *Acta Orthop.* **81,** 82–89 (2010).

6. Havelin, L. I. *et al.* The Nordic Arthroplasty Register Association: a unique collaboration between 3 national hip arthroplasty registries with 280,201 THRs. *Acta Orthop.* **80,** 393–401 (2009).

7. Steckelberg, J. M. & Osmon, D. R. Prosthetic Joint Infections. 173–209 (2000). doi:10.1128/9781555818067.ch9.

8. Kurtz, S. M. *et al.* Infection burden for hip and knee arthroplasty in the United States. *J. Arthroplasty* **23,** 984–991 (2008).

9. NIH consensus conference: Total hip replacement. NIH Consensus Development Panel on Total Hip Replacement. *JAMA* **273,** 1950–1956 (1995).

10. Dale, H. *et al.* Increasing risk of prosthetic joint infection after total hip arthroplasty. *Acta Orthop.* **83,** 449–458 (2012).

11. Gristina, A. G. Biomaterial-centered infection: microbial adhesion versus tissue integration. *Science* **237,** 1588–1595 (1987).

12. Berbari, E. F. *et al.* Risk factors for prosthetic joint infection: case-control study. *Clin. Infect. Dis. Off. Publ. Infect. Dis. Soc. Am.* **27,** 1247–1254 (1998).

13. Meehan, A. M., Osmon, D. R., Duffy, M. C. T., Hanssen, A. D. & Keating, M. R. Outcome of Penicillin-Susceptible Streptococcal Prosthetic Joint Infection Treated with Debridement and Retention of the Prosthesis. *Clin. Infect. Dis.* **36,** 845–849 (2003).

14. Berbari, E. *et al.* Inflammatory blood laboratory levels as markers of prosthetic joint infection: a systematic review and meta-analysis. *J. Bone Joint Surg. Am.* **92,** 2102–2109 (2010).

15. Schwotzer, N., Wahl, P., Fracheboud, D., Gautier, E. & Chuard, C. Optimal Culture Incubation Time in Orthopedic Device-Associated Infections: a Retrospective Analysis of Prolonged 14-Day Incubation. *J. Clin. Microbiol.* **52,** 61–66 (2014).

16. Kamme, C. & Lindberg, L. Aerobic and anaerobic bacteria in deep infections after total hip arthroplasty: differential diagnosis between infectious and non-infectious loosening. *Clin. Orthop.* 201–207 (1981).

17. Atkins, B. L. *et al.* Prospective evaluation of criteria for microbiological diagnosis of prosthetic-joint infection at revision arthroplasty. The OSIRIS Collaborative Study Group. *J. Clin. Microbiol.* **36,** 2932–2939 (1998).

18. Zhang, Q. *et al.* Acceleration of emergence of bacterial antibiotic resistance in connected microenvironments. *Science* **333,** 1764–1767 (2011).

19. Stiles, P. L., Dieringer, J. A., Shah, N. C. & Van Duyne, R. P. Surface-enhanced Raman spectroscopy. *Annu. Rev. Anal. Chem. Palo Alto Calif* **1,** 601–626 (2008).

20. Moskovits, M. Surface-Enhanced Spectroscopy. *Rev. Mod. Phys.* **57,** 783–826 (1985).

21. Kneipp, J., Kneipp, H. & Kneipp, K. SERS--a single-molecule and nanoscale tool for bioanalytics. *Chem. Soc. Rev.* **37,** 1052–1060 (2008).

22. Qian, X.-M. & Nie, S. M. Single-molecule and single-nanoparticle SERS: from fundamental mechanisms to biomedical applications. *Chem. Soc. Rev.* **37,** 912–920 (2008).

23. Fenniri, H. & Alvarez-Puebla, R. High-throughput screening flows along. *Nat. Chem. Biol.* **3,** 247–249 (2007).

24. Chen, L. & Choo, J. Recent advances in surface-enhanced Raman scattering detection technology for microfluidic chips. *Electrophoresis* **29,** 1815–1828 (2008).

25. Manz, A. *et al.* Planar Chips Technology for Miniaturization and Integration of Separation Techniques into Monitoring Systems - Capillary Electrophoresis on a Chip. *J. Chromatogr.* **593,** 253–258 (1992).

26. Chrimes, A. F., Khoshmanesh, K., Stoddart, P. R., Mitchell, A. & Kalantar-Zadeh, K. Microfluidics and Raman microscopy: current applications and future challenges. *Chem. Soc. Rev.* **42,** 5880–5906 (2013).

27. Cockerill, F. R. *et al.* Optimal Testing Parameters for Blood Cultures. *Clin. Infect. Dis.* **38,** 1724–1730 (2004).

28. Parvizi, J. *et al.* New definition for periprosthetic joint infection: from the Workgroup of the Musculoskeletal Infection Society. *Clin. Orthop.* **469,** 2992–2994 (2011).

29. Maderazo, E. G., Judson, S. & Pasternak, H. Late infections of total joint prostheses. A review and recommendations for prevention. *Clin. Orthop.* 131–142 (1988).

30. Gallo, J., Kolár, M., Novotný, R., Riháková, P. & Tichá, V. Pathogenesis of prosthesis-related infection. *Biomed. Pap. Med. Fac. Univ. Palacký Olomouc Czechoslov.* **147,** 27–35 (2003).

31. Wisplinghoff, H. *et al.* Nosocomial bloodstream infections in US hospitals: analysis of 24,179 cases from a prospective nationwide surveillance study. *Clin. Infect. Dis. Off. Publ. Infect. Dis. Soc. Am.* **39,** 309–317 (2004).

32. Friedman, N. D. *et al.* Health care--associated bloodstream

infections in adults: a reason to change the accepted definition of community-acquired infections. *Ann. Intern. Med.* **137,** 791–797 (2002).

33. Jacobsson, G., Dashti, S., Wahlberg, T. & Andersson, R. The epidemiology of and risk factors for invasive Staphylococcus aureus infections in western Sweden. *Scand. J. Infect. Dis.* **39,** 6–13 (2007).

34. Fey, P. D. & Olson, M. E. Current concepts in biofilm formation of Staphylococcus epidermidis. *Future Microbiol.* **5,** 917–933 (2010).

35. Vuong, C. *et al.* Regulated expression of pathogen-associated molecular pattern molecules in Staphylococcus epidermidis: quorum-sensing determines pro-inflammatory capacity and production of phenol-soluble modulins. *Cell. Microbiol.* **6,** 753–759 (2004).

36. Diekema, D. J. *et al.* Survey of infections due to Staphylococcus species: frequency of occurrence and antimicrobial susceptibility of isolates collected in the United States, Canada, Latin America, Europe, and the Western Pacific region for the SENTRY Antimicrobial Surveillance Program, 1997-1999. *Clin. Infect. Dis. Off. Publ. Infect. Dis. Soc. Am.* **32 Suppl 2,** S114-132 (2001).

37. Emerton, M. E., Crook, D. W. & Cooke, P. H. Streptococcus bovis-infected total hip arthroplasty. *J. Arthroplasty* **10,** 554–555 (1995).

38. Coelho-Prabhu, N. *et al.* Increased risk of prosthetic joint infection associated with esophago-gastro-duodenoscopy with biopsy. *Acta Orthop.* **84,** 82–86 (2013).

39. Wollner, A., Gilon, D., Mattan, Y., Rubinow, A. & Pogrund, H. Pneumococcal infection of a prosthetic hip joint. *Int. Orthop.* **13,** 135–136 (1989).

40. Cobo, J. *et al.* Early prosthetic joint infection: outcomes with debridement and implant retention followed by antibiotic therapy. *Clin. Microbiol. Infect. Off. Publ. Eur. Soc. Clin. Microbiol. Infect. Dis.* **17,** 1632–1637 (2011).

41. Peel, T. N., Cheng, A. C., Choong, P. F. M. & Buising, K. L. Early onset prosthetic hip and knee joint infection: treatment and outcomes in

Victoria, Australia. *J. Hosp. Infect.* **82,** 248–253 (2012).

42. Aboltins, C. A. *et al.* Gram-negative prosthetic joint infection treated with debridement, prosthesis retention and antibiotic regimens including a fluoroquinolone. *Clin. Microbiol. Infect. Off. Publ. Eur. Soc. Clin. Microbiol. Infect. Dis.* **17,** 862–867 (2011).

43. Raut, V. V., Orth, M. S., Orth, M. C., Siney, P. D. & Wroblewski, B. M. One stage revision arthroplasty of the hip for deep gram negative infection. *Int. Orthop.* **20,** 12–14 (1996).

44. Hsieh, P.-H. *et al.* Gram-negative prosthetic joint infections: risk factors and outcome of treatment. *Clin. Infect. Dis. Off. Publ. Infect. Dis. Soc. Am.* **49,** 1036–1043 (2009).

45. Piper, K. E. *et al.* Microbiologic diagnosis of prosthetic shoulder infection by use of implant sonication. *J. Clin. Microbiol.* **47,** 1878–1884 (2009).

46. Butler-Wu, S. M. *et al.* Optimization of periprosthetic culture for diagnosis of Propionibacterium acnes prosthetic joint infection. *J. Clin. Microbiol.* **49,** 2490–2495 (2011).

47. Donlan, R. M. & Costerton, J. W. Biofilms: survival mechanisms of clinically relevant microorganisms. *Clin. Microbiol. Rev.* **15,** 167–193 (2002).

48. Molina-Manso, D. *et al.* In vitro susceptibility to antibiotics of staphylococci in biofilms isolated from orthopaedic infections. *Int. J. Antimicrob. Agents* **41,** 521–523 (2013).

49. del Pozo, J. L. & Patel, R. The challenge of treating biofilm-associated bacterial infections. *Clin. Pharmacol. Ther.* **82,** 204–209 (2007).

50. Osmon, D. R. *et al.* Diagnosis and management of prosthetic joint infection: clinical practice guidelines by the Infectious Diseases Society of America. *Clin. Infect. Dis. Off. Publ. Infect. Dis. Soc. Am.* **56,** e1–e25 (2013).

51. Parvizi, J., Gehrke, T. & Chen, A. F. Proceedings of the International Consensus on Periprosthetic Joint Infection. *Bone Jt. J.* **95-B,** 1450–1452

(2013).

52. Cyteval, C. *et al.* Painful infection at the site of hip prosthesis: CT imaging. *Radiology* **224,** 477–483 (2002).

53. Alvarez-Puebla, R. A. & Liz-Marzan, L. M. SERS-Based Diagnosis and Biodetection. *Small* **6,** 604–610 (2010).

54. Tsukayama, D. T., Wicklund, B. & Gustilo, R. B. Suppressive antibiotic therapy in chronic prosthetic joint infections. *Orthopedics* **14,** 841–844 (1991).

55. Byren, I. *et al.* One hundred and twelve infected arthroplasties treated with 'DAIR' (debridement, antibiotics and implant retention): antibiotic duration and outcome. *J. Antimicrob. Chemother.* **63,** 1264–1271 (2009).

56. Brandt, C. M. *et al.* Staphylococcus aureus prosthetic joint infection treated with debridement and prosthesis retention. *Clin. Infect. Dis. Off. Publ. Infect. Dis. Soc. Am.* **24,** 914–919 (1997).

57. Marculescu, C. E. *et al.* Outcome of prosthetic joint infections treated with debridement and retention of components. *Clin. Infect. Dis. Off. Publ. Infect. Dis. Soc. Am.* **42,** 471–478 (2006).

58. Widmer, A. F., Frei, R., Rajacic, Z. & Zimmerli, W. Correlation between in vivo and in vitro efficacy of antimicrobial agents against foreign body infections. *J. Infect. Dis.* **162,** 96–102 (1990).

59. Widmer, A. F., Wiestner, A., Frei, R. & Zimmerli, W. Killing of nongrowing and adherent Escherichia coli determines drug efficacy in device-related infections. *Antimicrob. Agents Chemother.* **35,** 741–746 (1991).

60. Anderl, J. N., Zahller, J., Roe, F. & Stewart, P. S. Role of nutrient limitation and stationary-phase existence in Klebsiella pneumoniae biofilm resistance to ampicillin and ciprofloxacin. *Antimicrob. Agents Chemother.* **47,** 1251–1256 (2003).

61. Zimmerli, W., Widmer, A. F., Blatter, M., Frei, R. & Ochsner, P. E.

Role of rifampin for treatment of orthopedic implant-related staphylococcal infections: a randomized controlled trial. Foreign-Body Infection (FBI) Study Group. *JAMA* **279,** 1537–1541 (1998).

62. Kadurugamuwa, J. L. *et al.* Noninvasive optical imaging method to evaluate postantibiotic effects on biofilm infection in vivo. *Antimicrob. Agents Chemother.* **48,** 2283–2287 (2004).

63. Smekal, A. Zur Quantentheorie der Dispersion. *Naturwissenschaften* **11,** 873–875

64. Raman, C. V. & Krishnan, K. S. A New Type of Secondary Radiation. *Nature* **121,** 501–502 (1928).

65. VoDinh, T., Velthorst, N. H., Moore, D. S. & Schrader, B. Nomenclature, symbols, units, and their usage in spectrochemical analysis .16. Laser-based molecular spectroscopy for chemical analysis - Luminescence. *Pure Appl. Chem.* **69,** 1435–1449 (1997).

66. Alvarez-Puebla, R. A. & Liz-Marzan, L. M. Traps and cages for universal SERS detection. *Chem. Soc. Rev.* **41,** 43–51 (2012).

67. Alvarez-Puebla, R. A. & Liz-Marzan, L. M. SERS Detection of Small Inorganic Molecules and Ions. *Angew. Chem.-Int. Ed.* **51,** 11214–11223 (2012).

68. Schluecker, S. Surface-Enhanced Raman Spectroscopy: Concepts and Chemical Applications. *Angew. Chem.-Int. Ed.* **53,** 4756–4795 (2014).

69. Wang, Y., Yan, B. & Chen, L. SERS Tags: Novel Optical Nanoprobes for Bioanalysis. *Chem. Rev.* **113,** 1391–1428 (2013).

70. Kim, H., Kosuda, K. M., Van Duyne, R. P. & Stair, P. C. Resonance Raman and surface- and tip-enhanced Raman spectroscopy methods to study solid catalysts and heterogeneous catalytic reactions. *Chem. Soc. Rev.* **39,** 4820–4844 (2010).

71. Golightly, R. S., Doering, W. E. & Natan, M. J. Surface-Enhanced Raman Spectroscopy and Homeland Security: A Perfect Match? *Acs Nano* **3,** 2859–2869 (2009).

72. Long, D. A. Raman Spectroscopy. *J. Mol. Struct.* **55,** 152 (1979).

73. Le Ru, E. C. & Etchegoin, P. G. Principles of Surface-Enhanced Raman Spectroscopy and related plasmonic effects Preface. *Princ. Surf.-Enhanc. Raman Spectrosc. Relat. Plasmonic Eff.* XVII-+ (2009). doi:10.1016/B978-0-444-52779-0.00005-2

74. Mulvaney, P. Surface plasmon spectroscopy of nanosized metal particles. *Langmuir* **12,** 788–800 (1996).

75. Bohren, C. & Nevitt, T. Absorption by a Sphere - a Simple Approximation. *Appl. Opt.* **22,** 774–775 (1983).

76. Turkevich, J., Stevenson, P. & Hillier, J. A Study of the Nucleation and Growth Processes in the Synthesis of Colloidal Gold. *Discuss. Faraday Soc.* 55–75 (1951). doi:10.1039/df9511100055

77. Enustun, B. & Turkevich, J. Coagulation of Colloidal Gold. *J. Am. Chem. Soc.* **85,** 3317–3328 (1963).

78. Mie, G. Articles on the optical characteristics of turbid tubes, especially colloidal metal solutions. *Ann. Phys.* **25,** 377–445 (1908).

79. Gans, R. The shape of ultra microscopic gold particles. *Ann. Phys.* **37,** 881–900 (1912).

80. Kreibig, U. Lattice-Defects in Small Metallic Particles and Their Influence on Size Effects. *Z. Phys. B-Condens. Matter* **31,** 39–47 (1978).

81. Kreibig, U. & Genzel, L. Optical absorption of small metallic particles. *Surf. Sci.* **156,** 678–700 (1985).

82. Lisiecki, I., Billoudet, F. & Pileni, M. P. Control of the shape and the size of copper metallic particles. *J. Phys. Chem.* **100,** 4160–4166 (1996).

83. Yu, Y. Y., Chang, S. S., Lee, C. L. & Wang, C. R. C. Gold nanorods: Electrochemical synthesis and optical properties. *J. Phys. Chem. B* **101,** 6661–6664 (1997).

84. Creighton, J. & Eadon, D. Ultraviolet Visible Absorption-Spectra of the Colloidal Metallic Elements. *J. Chem. Soc.-Faraday Trans.* **87,** 3881–3891 (1991).

85. Foss, C., Hornyak, G., Stockert, J. & Martin, C. Template-Synthesized Nanoscopic Gold Particles - Optical-Spectra and the Effects of Particle-Size and Shape. *J. Phys. Chem.* **98,** 2963–2971 (1994).

86. Link, S. & El-Sayed, M. A. Size and temperature dependence of the plasmon absorption of colloidal gold nanoparticles. *J. Phys. Chem. B* **103,** 4212–4217 (1999).

87. Underwood, S. & Mulvaney, P. Effect of the Solution Refractive-Index on the Color of Gold Colloids. *Langmuir* **10,** 3427–3430 (1994).

88. Liz-Marzan, L. M. & LadoTourino, I. Reduction and stabilization of silver nanoparticles in ethanol by nonionic surfactants. *Langmuir* **12,** 3585–3589 (1996).

89. Ung, T., Giersig, M., Dunstan, D. & Mulvaney, P. Spectroelectrochemistry of colloidal silver. *Langmuir* **13,** 1773–1782 (1997).

90. Linnert, T., Mulvaney, P. & Henglein, A. Surface-Chemistry of Colloidal Silver - Surface-Plasmon Damping by Chemisorbed I-, Sh-, and C6h5s-. *J. Phys. Chem.* **97,** 679–682 (1993).

91. Mulvaney, P., Linnert, T. & Henglein, A. Surface-Chemistry of Colloidal Silver in Aqueous-Solution - Observations. *J. Phys. Chem.* **95,** 7843–7846 (1991).

92. Mulvaney, P. Surface plasmon spectroscopy of nanosized metal particles. *Langmuir* **12,** 788–800 (1996).

93. Hostetler, M. J. *et al.* Alkanethiolate gold cluster molecules with core diameters from 1.5 to 5.2 nm: Core and monolayer properties as a function of core size. *Langmuir* **14,** 17–30 (1998).

94. Alvarez, M. M. *et al.* Optical absorption spectra of nanocrystal gold molecules. *J. Phys. Chem. B* **101,** 3706–3712 (1997).

95. Kreibig, U. Kramers Kronig Analysis of Optical Properties of Small Silver Particles. *Z. Phys.* **234,** 307–318 (1970).

96. Kreibig, U. & Vonfrags.c. Limitation of Electron Mean Free Path in

Small Silver Particles. *Z. Phys.* **224,** 307–323 (1969).

97. Kerker, M. Estimation of Surface-Enhanced Raman-Scattering from Surface-Averaged Electromagnetic Intensities. *J. Colloid Interface Sci.* **118,** 417–421 (1987).

98. Le Ru, E. C. & Etchegoin, P. G. Rigorous justification of the [E](4) enhancement factor in Surface Enhanced Raman Spectroscopy. *Chem. Phys. Lett.* **423,** 63–66 (2006).

99. Zeman, E. & Schatz, G. An Accurate Electromagnetic Theory Study of Surface Enhancement Factors for Ag, Au, Cu, Li, Na, Al, Ga, in, Zn, and Cd. *J. Phys. Chem.* **91,** 634–643 (1987).

100. Wang, D. & Kerker, M. Enhanced Raman-Scattering by Molecules Adsorbed at the Surface of Colloidal Spheroids. *Phys. Rev. B* **24,** 1777–1790 (1981).

101. Rodriguez-Lorenzo, L. *et al.* Zeptomol Detection Through Controlled Ultrasensitive Surface-Enhanced Raman Scattering. *J. Am. Chem. Soc.* **131,** 4616–4618 (2009).

102. Owen, J. F., Chen, T. T., Chang, R. K. & Laube, B. L. Irreversible loss of adatoms on Ag electrodes during potential cycling determined from surface enhanced raman intensities. *Surf. Sci.* **131,** 195–220 (1983).

103. Kneipp, K. *et al.* Detection and identification of a single DNA base molecule using surface-enhanced Raman scattering (SERS). *Phys. Rev. E* **57,** R6281–R6284 (1998).

104. Haynes, C. L., Yonzon, C. R., Zhang, X. Y. & Van Duyne, R. P. Surface-enhanced Raman sensors: early history and the development of sensors for quantitative biowarfare agent and glucose detection. *J. Raman Spectrosc.* **36,** 471–484 (2005).

105. Brus, L. Noble Metal Nanocrystals: Plasmon Electron Transfer Photochemistry and Single-Molecule Raman Spectroscopy. *Acc. Chem. Res.* **41,** 1742–1749 (2008).

106. Le Ru, E. C. & Etchegoin, P. G. Sub-wavelength localization of hot-

spots in SERS. *Chem. Phys. Lett.* **396,** 393–397 (2004).

107. Kneipp, K., Kneipp, H., Itzkan, I., Dasari, R. R. & Feld, M. S. Surface-enhanced Raman scattering and biophysics. *J. Phys.-Condens. Matter* **14,** R597–R624 (2002).

108. Prodan, E., Radloff, C., Halas, N. J. & Nordlander, P. A hybridization model for the plasmon response of complex nanostructures. *Science* **302,** 419–422 (2003).

109. Nordlander, P., Oubre, C., Prodan, E., Li, K. & Stockman, M. I. Plasmon hybridizaton in nanoparticle dimers. *Nano Lett.* **4,** 899–903 (2004).

110. Xu, H. X., Aizpurua, J., Kall, M. & Apell, P. Electromagnetic contributions to single-molecule sensitivity in surface-enhanced Raman scattering. *Phys. Rev. E* **62,** 4318–4324 (2000).

111. Hao, E. & Schatz, G. C. Electromagnetic fields around silver nanoparticles and dimers. *J. Chem. Phys.* **120,** 357–366 (2004).

112. Le Ru, E. C., Etchegoin, P. G. & Meyer, M. Enhancement factor distribution around a single surface-enhanced Raman scattering hot spot and its relation to single molecule detection. *J. Chem. Phys.* **125,** 204701 (2006).

113. Otto, A. Theory of first layer and single molecule surface enhanced Raman scattering (SERS). *Phys. Status Solidi -Appl. Res.* **188,** 1455–1470 (2001).

114. Mulvihill, M. J., Ling, X. Y., Henzie, J. & Yang, P. Anisotropic Etching of Silver Nanoparticles for Plasmonic Structures Capable of Single-Particle SERS. *J. Am. Chem. Soc.* **132,** 268–274 (2010).

115. Sau, T. K., Rogach, A. L., Jaeckel, F., Klar, T. A. & Feldmann, J. Properties and Applications of Colloidal Nonspherical Noble Metal Nanoparticles. *Adv. Mater.* **22,** 1805–1825 (2010).

116. Bailo, E. & Deckert, V. Tip-enhanced Raman scattering. *Chem. Soc. Rev.* **37,** 921–930 (2008).

117. de Abajo, F. J. G. Colloquium: Light scattering by particle and hole

arrays. *Rev. Mod. Phys.* **79,** 1267–1290 (2007).

118. Biswas, A. *et al.* Advances in top-down and bottom-up surface nanofabrication: Techniques, applications & future prospects. *Adv. Colloid Interface Sci.* **170,** 2–27 (2012).

119. Gaffet, E., Tachikart, M., ElKedim, O. & Rahouadj, R. Nanostructural materials formation by mechanical alloying: Morphologic analysis based on transmission and scanning electron microscopic observations. *Mater. Charact.* **36,** 185–190 (1996).

120. Frens, G. Controlled Nucleation for Regulation of Particle-Size in Monodisperse Gold Suspensions. *Nat.-Phys. Sci.* **241,** 20–22 (1973).

121. Freeman, R. *et al.* Self-Assembled Metal Colloid Monolayers - an Approach to Sers Substrates. *Science* **267,** 1629–1632 (1995).

122. Rodriguez-Fernandez, J., Perez-Juste, J., Mulvaney, P. & Liz-Marzan, L. M. Spatially-directed oxidation of gold nanoparticles by Au(III)-CTAB complexes. *J. Phys. Chem. B* **109,** 14257–14261 (2005).

123. Perez-Juste, J., Pastoriza-Santos, I., Liz-Marzan, L. M. & Mulvaney, P. Gold nanorods: Synthesis, characterization and applications. *Coord. Chem. Rev.* **249,** 1870–1901 (2005).

124. Liz-Marzan, L. M. Nanometals formation and color. *Mater. Today* **7,** 26–31 (2004).

125. Martin, C. R. Membrane-based synthesis of nanomaterials. *Chem. Mater.* **8,** 1739–1746 (1996).

126. Perez-Juste, J., Rodriguez-Gonzalez, B., Mulvaney, P. & Liz-Marzan, L. M. Optical control and patterning of gold-nanorod-poly(vinyl alcohol) nanocomposite films. *Adv. Funct. Mater.* **15,** 1065–1071 (2005).

127. Nikoobakht, B. & El-Sayed, M. A. Preparation and growth mechanism of gold nanorods (NRs) using seed-mediated growth method. *Chem. Mater.* **15,** 1957–1962 (2003).

128. Busbee, B. D., Obare, S. O. & Murphy, C. J. An improved synthesis of high-aspect-ratio gold nanorods. *Adv. Mater.* **15,** 414–416 (2003).

129. Lee, P. & Meisel, D. Adsorption and Surface-Enhanced Raman of Dyes on Silver and Gold Sols. *J. Phys. Chem.* **86,** 3391–3395 (1982).

130. Creighton, J., Blatchford, C. & Albrecht, M. Plasma Resonance Enhancement of Raman-Scattering by Pyridine Adsorbed on Silver or Gold Sol Particles of Size Comparable to the Excitation Wavelength. *J. Chem. Soc.-Faraday Trans. Ii* **75,** 790–798 (1979).

131. Abalde-Cela, S. *et al.* Surface-enhanced Raman scattering biomedical applications of plasmonic colloidal particles. *J. R. Soc. Interface* **7,** S435–S450 (2010).

132. Senthil Kumar, P., Pastoriza-Santos, I., Rodriguez-Gonzalez, B., Garcia de Abajo, F. J. & Liz-Marzan, L. M. High-yield synthesis and optical response of gold nanostars. *Nanotechnology* **19,** 15606 (2008).

133. Perez-Juste, J., Liz-Marzan, L. M., Carnie, S., Chan, D. Y. C. & Mulvaney, P. Electric-field-directed growth of gold nanorods in aqueous surfactant solutions. *Adv. Funct. Mater.* **14,** 571–579 (2004).

134. Fievet, F., Fievetvincent, F., Lagier, J., Dumont, B. & Figlarz, M. Controlled Nucleation and Growth of Micrometer-Size Copper Particles Prepared by the Polyol Process. *J. Mater. Chem.* **3,** 627–632 (1993).

135. Chang, C.-C., Wu, H.-L., Kuo, C.-H. & Huang, M. H. Hydrothermal Synthesis of Monodispersed Octahedral Gold Nanocrystals with Five Different Size Ranges and Their Self-Assembled Structures. *Chem. Mater.* **20,** 7570–7574 (2008).

136. Gu, C. & Zhang, T.-Y. Electrochemical Synthesis of Silver Polyhedrons and Dendritic Films with Superhydrophobic Surfaces. *Langmuir* **24,** 12010–12016 (2008).

137. Meng, G. *et al.* A General Synthetic Approach to Interconnected Nanowire/Nanotube and Nanotube/Nanowire/Nanotube Heterojunctions with Branched Topology. *Angew. Chem.-Int. Ed.* **48,** 7166–7170 (2009).

138. Henry, A.-I. *et al.* Correlated Structure and Optical Property Studies of Plasmonic Nanoparticles. *J. Phys. Chem. C* **115,** 9291–9305 (2011).

139. Industrial Applications of Malvern Instruments Products and Services. Available at: http://www.malvern.com/en/industry-applications/default.aspx. (Accessed: 27th June 2016)

140. Stern, O. The theory of the electrolytic double shift. *Z. Elektrochem. Angew. Phys. Chem.* **30,** 508–516 (1924).

141. Landau, L. On the theory of secondary showers. *J. Phys.-Ussr* **4,** 375–376 (1941).

142. Verwey, E. Theory of the Stability of Lyophobic Colloids. *J. Phys. Colloid Chem.* **51,** 631–636 (1947).

143. Grubisha, D. S., Lipert, R. J., Park, H. Y., Driskell, J. & Porter, M. D. Femtomolar detection of prostate-specific antigen: An immunoassay based on surface-enhanced Raman scattering and immunogold labels. *Anal. Chem.* **75,** 5936–5943 (2003).

144. Lin, H.-Y. *et al.* On-line SERS Detection of Single Bacterium Using Novel SERS Nanoprobes and A Microfluidic Dielectrophoresis Device. *Small* **10,** 4700–4710 (2014).

145. Alvarez-Puebla, R. A. *et al.* Gold nanorods 3D-supercrystals as surface enhanced Raman scattering spectroscopy substrates for the rapid detection of scrambled prions. *Proc. Natl. Acad. Sci. U. S. A.* **108,** 8157–8161 (2011).

146. Rodriguez-Lorenzo, L., Fabris, L. & Alvarez-Puebla, R. A. Multiplex optical sensing with surface-enhanced Raman scattering: A critical review. *Anal. Chim. Acta* **745,** 10–23 (2012).

147. Evans, J. Random and Cooperative Sequential Adsorption. *Rev. Mod. Phys.* **65,** 1281–1329 (1993).

148. Doerr, A. Multiplexing to the max. *Nat. Methods* **4,** 381–381 (2007).

149. Wilson, R., Cossins, A. R. & Spiller, D. G. Encoded microcarriers for high-throughput multiplexed detection. *Angew. Chem.-Int. Ed.* **45,** 6104–6117 (2006).

150. Shtengel, G. *et al.* Interferometric fluorescent super-resolution

microscopy resolves 3D cellular ultrastructure. *Proc. Natl. Acad. Sci. U. S. A.* **106,** 3125–3130 (2009).

151. Doering, W. E., Piotti, M. E., Natan, M. J. & Freeman, R. G. SERS as a foundation for nanoscale, optically detected biological labels. *Adv. Mater.* **19,** 3100–3108 (2007).

152. Sha, M. Y. *et al.* Multiplexed SNP genotyping using nanobarcode particle technology. *Anal. Bioanal. Chem.* **384,** 658–666 (2006).

153. Bake, K. D. & Walt, D. R. in *Annual Review of Analytical Chemistry* **1,** 515–547 (Annual Reviews, 2008).

154. Freeman, R. G. *et al.* Use of nanobarcodes (R) particles in bioassays. *Nanobiotechnology Protoc.* **303,** 73–83 (2005).

155. Braeckmans, K. & De Smedt, S. C. COLOUR-CODED MICROCARRIERS Made to move. *Nat. Mater.* **9,** 697–698 (2010).

156. Braeckmans, K. *et al.* Encoding microcarriers by spatial selective photobleaching. *Nat. Mater.* **2,** 169–173 (2003).

157. Finkel, N. H., Lou, X. H., Wang, C. Y. & He, L. Barcoding the microworld. *Anal. Chem.* **76,** 353A–359A (2004).

158. Cunin, F. *et al.* Biomolecular screening with encoded porous-silicon photonic crystals. *Nat. Mater.* **1,** 39–41 (2002).

159. Pregibon, D. C., Toner, M. & Doyle, P. S. Multifunctional encoded particles for high-throughput biomolecule analysis. *Science* **315,** 1393–1396 (2007).

160. Vaino, A. R. & Janda, K. D. Euclidean shape-encoded combinatorial chemical libraries. *Proc. Natl. Acad. Sci. U. S. A.* **97,** 7692–7696 (2000).

161. Fenniri, H., Ding, L. H., Ribbe, A. E. & Zyrianov, Y. Barcoded resins: A new concept for polymer-supported combinatorial library self-deconvolution. *J. Am. Chem. Soc.* **123,** 8151–8152 (2001).

162. Raez, J. *et al.* Spectroscopically encoded microspheres for antigen biosensing. *Langmuir* **23,** 6482–6485 (2007).

163. Lee, J. *et al.* Universal process-inert encoding architecture for polymer microparticles. *Nat. Mater.* **13,** 524–529 (2014).

164. Bruchez, M., Moronne, M., Gin, P., Weiss, S. & Alivisatos, A. P. Semiconductor nanocrystals as fluorescent biological labels. *Science* **281,** 2013–2016 (1998).

165. Sanles-Sobrido, M. *et al.* Design of SERS-Encoded, Submicron, Hollow Particles Through Confined Growth of Encapsulated Metal Nanoparticles. *J. Am. Chem. Soc.* **131,** 2699–2705 (2009).

166. Goddard, G. *et al.* High-Resolution Spectral Analysis of Individual SERS-Active Nanoparticles in Flow. *J. Am. Chem. Soc.* **132,** 6081–6090 (2010).

167. Howarth, M. *et al.* Monovalent, reduced-size quantum dots for imaging receptors on living cells. *Nat. Methods* **5,** 397–399 (2008).

168. Serge, A., Bertaux, N., Rigneault, H. & Marguet, D. Dynamic multiple-target tracing to probe spatiotemporal cartography of cell membranes. *Nat. Methods* **5,** 687–694 (2008).

169. Qian, X. *et al.* In vivo tumor targeting and spectroscopic detection with surface-enhanced Raman nanoparticle tags. *Nat. Biotechnol.* **26,** 83–90 (2008).

170. Rivera Gil, P. *et al.* Plasmonic nanoprobes for real-time optical monitoring of nitric oxide inside living cells. *Angew. Chem. Int. Ed Engl.* **52,** 13694–13698 (2013).

171. Pazos-Perez, N. *et al.* Organized Plasmonic Clusters with High Coordination Number and Extraordinary Enhancement in Surface-Enhanced Raman Scattering (SERS). *Angew. Chem.-Int. Ed.* **51,** 12688–12693 (2012).

172. Song, J., Zhou, J. & Duan, H. Self-Assembled Plasmonic Vesicles of SERS-Encoded Amphiphilic Gold Nanoparticles for Cancer Cell Targeting and Traceable Intracellular Drug Delivery. *J. Am. Chem. Soc.* **134,** 13458–13469 (2012).

173. Guerrero-Martinez, A., Perez-Juste, J. & Liz-Marzan, L. M. Recent Progress on Silica Coating of Nanoparticles and Related Nanomaterials. *Adv. Mater.* **22,** 1182–1195 (2010).

174. Song, J. *et al.* SERS-Encoded Nanogapped Plasmonic Nanoparticles: Growth of Metallic Nanoshell by Templating Redox-Active Polymer Brushes. *J. Am. Chem. Soc.* **136,** 6838–6841 (2014).

175. Lim, D.-K. *et al.* Highly uniform and reproducible surface-enhanced Raman scattering from DNA-tailorable nanoparticles with 1-nm interior gap. *Nat. Nanotechnol.* **6,** 452–460 (2011).

176. Alba, M. *et al.* Macroscale Plasmonic Substrates for Highly Sensitive Surface-Enhanced Raman Scattering. *Angew. Chem.-Int. Ed.* **52,** 6459–6463 (2013).

177. Su, X. *et al.* Composite organic-inorganic nanoparticles (COINs) with chemically encoded optical signatures. *Nano Lett.* **5,** 49–54 (2005).

178. Sun, L. *et al.* Composite organic-inorganic nanoparticles as Raman labels for tissue analysis. *Nano Lett.* **7,** 351–356 (2007).

179. Fernandez-Lopez, C. *et al.* Highly Controlled Silica Coating of PEG-Capped Metal Nanoparticles and Preparation of SERS-Encoded Particles. *Langmuir* **25,** 13894–13899 (2009).

180. Ghosh, P., Han, G., De, M., Kim, C. K. & Rotello, V. M. Gold nanoparticles in delivery applications. *Adv. Drug Deliv. Rev.* **60,** 1307–1315 (2008).

181. Li, H., Xia, H., Wang, D. & Tao, X. Simple Synthesis of Monodisperse, Quasi-spherical, Citrate-Stabilized Silver Nanocrystals in Water. *Langmuir* **29,** 5074–5079 (2013).

182. Paramelle, D. *et al.* A rapid method to estimate the concentration of citrate capped silver nanoparticles from UV-visible light spectra. *Analyst* **139,** 4855–4861 (2014).

183. Pazos-Perez, N., Garcia de Abajo, F. J., Fery, A. & Alvarez-Puebla, R. A. From Nano to Micro: Synthesis and Optical Properties of Homogeneous

Spheroidal Gold Particles and Their Superlattices. *Langmuir* **28,** 8909–8914 (2012).

184. Yguerabide, J. & Yguerabide, E. E. Light-scattering submicroscopic particles as highly fluorescent analogs and their use as tracer labels in clinical and biological applications - I. Theory. *Anal. Biochem.* **262,** 137–156 (1998).

185. Barbosa, S. *et al.* Tuning Size and Sensing Properties in Colloidal Gold Nanostars. *Langmuir* **26,** 14943–14950 (2010).

186. Goulet, P. J. G. & Aroca, R. F. Distinguishing individual vibrational fingerprints: Single-molecule surface-enhanced resonance raman scattering from one-to-one binary mixtures in Langmuir-Blodgett monolayers. *Anal. Chem.* **79,** 2728–2734 (2007).

187. Goulet, P. J. G., Pieczonka, N. P. W. & Aroca, R. F. Overtones and combinations in single-molecule surface. enhanced resonance Raman scattering spectra. *Anal. Chem.* **75,** 1918–1923 (2003).

188. Hiramatsu, H. & Osterloh, F. E. pH-controlled assembly and disassembly of electrostatically linked CdSe-SiO2 and Au-SiO2 nanoparticle clusters. *Langmuir* **19,** 7003–7011 (2003).

189. Bryant, M. & Pemberton, J. Surface Raman-Scattering of Self-Assembled Monolayers Formed from 1-Alkanethiols at Ag. *J. Am. Chem. Soc.* **113,** 3629–3637 (1991).

190. Guerrini, L., Izquierdo-Lorenzo, I., Garcia-Ramos, J. V., Domingo, C. & Sanchez-Cortes, S. Self-assembly of alpha,omega-aliphatic diamines on Ag nanoparticles as an effective localized surface plasmon nanosensor based in interparticle hot spots. *Phys. Chem. Chem. Phys.* **11,** 7363–7371 (2009).

191. Stober, W., Fink, A. & Bohn, E. Controlled Growth of Monodisperse Silica Spheres in Micron Size Range. *J. Colloid Interface Sci.* **26,** 62–69 (1968).

192. Xue, C., Chen, X., Hurst, S. J. & Mirkin, C. A. Self-assembled monolayer mediated silica coating of silver triangular nanoprisms. *Adv.*

Mater. **19,** 4071–4074 (2007).

193. Chen, T., Chen, G., Xing, S., Wu, T. & Chen, H. Scalable Routes to Janus Au-SiO2 and Ternary Ag-Au-SiO2 Nanoparticles. *Chem. Mater.* **22,** 3826–3828 (2010).

194. Wallace, A. F., DeYoreo, J. J. & Dove, P. M. Kinetics of Silica Nucleation on Carboxyl- and Amine-Terminated Surfaces: Insights for Biomineralization. *J. Am. Chem. Soc.* **131,** 5244–5250 (2009).

195. Wong, Y. J. *et al.* Revisiting the Stober Method: In homogeneity in Silica Shells. *J. Am. Chem. Soc.* **133,** 11422–11425 (2011).

196. Rodriguez-Lorenzo, L. *et al.* Intracellular mapping with SERS-encoded gold nanostars. *Integr. Biol.* **3,** 922–926 (2011).

197. Simakova, P., Gautier, J., Prochazka, M., Herve-Aubert, K. & Chourpa, I. Polyethylene-glycol-Stabilized Ag Nanoparticles for Surface-Enhanced Raman Scattering Spectroscopy: Ag Surface Accessibility Studied Using Metalation of Free-Base Porphyrins. *J. Phys. Chem. C* **118,** 7690–7697 (2014).

198. Murphy, C. J. *et al.* Gold Nanoparticles in Biology: Beyond Toxicity to Cellular Imaging. *Acc. Chem. Res.* **41,** 1721–1730 (2008).

199. Fleischmann, M., Hendra, P. & Mcquilla.aj. Raman-Spectra of Pyridine Adsorbed at a Silver Electrode. *Chem. Phys. Lett.* **26,** 163–166 (1974).

200. Ko, H., Singamaneni, S. & Tsukruk, V. V. Nanostructured Surfaces and Assemblies as SERS Media. *Small* **4,** 1576–1599 (2008).

201. Spuch-Calvar, M., Rodriguez-Lorenzo, L., Morales, M. P., Alvarez-Puebla, R. A. & Liz-Marzan, L. M. Bifunctional Nanocomposites with Long-Term Stability as SERS Optical Accumulators for Ultrasensitive Analysis. *J. Phys. Chem. C* **113,** 3373–3377 (2009).

202. Abalde-Cela, S. *et al.* SERS Chiral Recognition and Quantification of Enantiomers through Cyclodextrin Supramolecular Complexation. *Chemphyschem* **12,** 1529–1535 (2011).

203. Lange, H. *et al.* Tunable Plasmon Coupling in Distance-Controlled Gold Nanoparticles. *Langmuir* **28,** 8862–8866 (2012).

204. Guerrini, L. *et al.* Chemical speciation of heavy metals by surface-enhanced Raman scattering spectroscopy: identification and quantification of inorganic- and methyl-mercury in water. *Nanoscale* **6,** 8368–8375 (2014).

205. Tsoutsi, D. *et al.* Quantitative Surface-Enhanced Raman Scattering Ultradetection of Atomic Inorganic Ions: The Case of Chloride. *Acs Nano* **5,** 7539–7546 (2011).

206. Mir-Simon, B., Reche-Perez, I., Guerrini, L., Pazos-Perez, N. & Alvarez-Puebla, R. A. Universal One-Pot and Scalable Synthesis of SERS Encoded Nanoparticles. *Chem. Mater.* **27,** 950–958 (2015).

207. Bastus, N. G., Comenge, J. & Puntes, V. Kinetically Controlled Seeded Growth Synthesis of Citrate-Stabilized Gold Nanoparticles of up to 200 nm: Size Focusing versus Ostwald Ripening. *Langmuir* **27,** 11098–11105 (2011).

208. Decher, G. Fuzzy nanoassemblies: Toward layered polymeric multicomposites. *Science* **277,** 1232–1237 (1997).

209. Ahijado-Guzman, R., Gomez-Puertas, P., Alvarez-Puebla, R. A., Rivas, G. & Liz-Marzan, L. M. Surface-Enhanced Raman Scattering-Based Detection of the Interactions between the Essential Cell Division FtsZ Protein and Bacterial Membrane Elements. *Acs Nano* **6,** 7514–7520 (2012).

210. Guerrini, L. *et al.* Effect of Metal-Liquid Interface Composition on the Adsorption of a Cyanine Dye onto Gold Nanoparticles. *Langmuir* **29,** 1139–1147 (2013).

211. LeRu, E. C. & Etchegoin, P. G. *Principles of Surface-Enhanced Raman Spectroscopy: And Related Plasmonic Effects*. (Elsevier Science Bv, 2009).

212. Myroshnychenko, V. *et al.* Modelling the optical response of gold nanoparticles. *Chem. Soc. Rev.* **37,** 1792–1805 (2008).

213. Rodriguez-Fernandez, J., Perez-Juste, J., Javier Garcia de Abajo, F.

& Liz-Marzan, L. M. Seeded growth of submicron Au colloids with quadrupole plasmon resonance modes. *Langmuir* **22,** 7007–7010 (2006).

214. Hurst, S. J., Lytton-Jean, A. K. R. & Mirkin, C. A. Maximizing DNA loading on a range of gold nanoparticle sizes. *Anal. Chem.* **78,** 8313–8318 (2006).

215. Krpetic, Z. *et al.* Directed Assembly of DNA-Functionalized Gold Nanoparticles Using Pyrrole-Imidazole Polyamides. *J. Am. Chem. Soc.* **134,** 8356–8359 (2012).

216. Jung, H. Y., Park, Y.-K., Park, S. & Kim, S. K. Surface enhanced Raman scattering from layered assemblies of close-packed gold nanopardicles. *Anal. Chim. Acta* **602,** 236–243 (2007).

217. Le Ru, E. C., Galloway, C. & Etchegoin, P. G. On the connection between optical absorption/extinction and SERS enhancements. *Phys. Chem. Chem. Phys.* **8,** 3083–3087 (2006).

218. Kleinman, S. L. *et al.* Structure Enhancement Factor Relationships in Single Gold Nanoantennas by Surface-Enhanced Raman Excitation Spectroscopy. *J. Am. Chem. Soc.* **135,** 301–308 (2013).

219. Njoki, P. N. *et al.* Size correlation of optical and spectroscopic properties for gold nanoparticles. *J. Phys. Chem. C* **111,** 14664–14669 (2007).

220. Kurtz, S. M., Lau, E., Watson, H., Schmier, J. K. & Parvizi, J. Economic burden of periprosthetic joint infection in the United States. *J. Arthroplasty* **27,** 61–65.e1 (2012).

221. Kurtz, S., Ong, K., Lau, E., Mowat, F. & Halpern, M. Projections of primary and revision hip and knee arthroplasty in the United States from 2005 to 2030. *J. Bone Joint Surg. Am.* **89,** 780–785 (2007).

222. Fournier, P.-E. *et al.* Modern clinical microbiology: new challenges and solutions. *Nat. Rev. Microbiol.* **11,** 574–585 (2013).

223. de Wildt, R. M. T., Mundy, C. R., Gorick, B. D. & Tomlinson, I. M. Antibody arrays for high-throughput screening of antibody-antigen

interactions. *Nat. Biotechnol.* **18,** 989–994 (2000).

224. Ottesen, E. A., Hong, J. W., Quake, S. R. & Leadbetter, J. R. Microfluidic digital PCR enables multigene analysis of individual environmental bacteria. *Science* **314,** 1464–1467 (2006).

225. Maier, T. & Kostrzewa, M. Fast and reliable MALDI-TOF MS-based microorganism identification. *Chim. Oggi-Chem. Today* **25,** 68–71 (2007).

226. Perros, M. A sustainable model for antibiotics. *Science* **347,** 1062–1064 (2015).

227. Zimmerli, W., Trampuz, A. & Ochsner, P. E. Prosthetic-joint infections. *N. Engl. J. Med.* **351,** 1645–1654 (2004).

228. Kanthor, R. DIAGNOSTICS Detection drives defence. *Nature* **509,** S14–S15 (2014).

229. Zumla, A. *et al.* Rapid point of care diagnostic tests for viral and bacterial respiratory tract infections-needs, advances, and future prospects. *Lancet Infect. Dis.* **14,** 1123–1135 (2014).

230. Howes, P. D., Chandrawati, R. & Stevens, M. M. Colloidal nanoparticles as advanced biological sensors. *Science* **346,** 53–62 (2014).

231. Rodrigo, D. *et al.* Mid-infrared plasmonic biosensing with graphene. *Science* **349,** 165–168 (2015).

232. Pelaz, B. *et al.* The State of Nanoparticle-Based Nanoscience and Biotechnology: Progress, Promises, and Challenges. *Acs Nano* **6,** 8468–8483 (2012).

233. Piorek, B. D. *et al.* Free-surface microfluidic control of surface-enhanced Raman spectroscopy for the optimized detection of airborne molecules. *Proc. Natl. Acad. Sci. U. S. A.* **104,** 18898–18901 (2007).

234. Cheng, I.-F., Chang, H.-C., Chen, T.-Y., Hu, C. & Yang, F.-L. Rapid (<5 min) identification of pathogen in human blood by electrokinetic concentration and surface-enhanced Raman spectroscopy. *Sci. Rep.* **3,** 2365 (2013).

235. Hol, F. J. H. & Dekker, C. Zooming in to see the bigger picture:

Microfluidic and nanofabrication tools to study bacteria. *Science* **346,** 438–447 (2014).

236. Kang, D.-K. *et al.* Rapid detection of single bacteria in unprocessed blood using Integrated Comprehensive Droplet Digital Detection. *Nat. Commun.* **5,** 5427 (2014).

237. Chen, W. *et al.* Identification of Bacteria in Water by a Fluorescent Array. *Angew. Chem.-Int. Ed.* **53,** 13734–13739 (2014).

238. Gracie, K. *et al.* Simultaneous detection and quantification of three bacterial meningitis pathogens by SERS. *Chem. Sci.* **5,** 1030–1040 (2014).

239. Wang, H. *et al.* Simultaneous Capture, Detection, and Inactivation of Bacteria as Enabled by a Surface-Enhanced Raman Scattering Multifunctional Chip. *Angew. Chem.-Int. Ed.* **54,** 5132–5136 (2015).

240. Dellinger, R. P., Levy, M. M. & Rhodes, A. Surviving Sepsis Campaign: International Guidelines for Management of Severe Sepsis and Septic Shock: 2012 (vol 41, pg 580, 2013). *Crit. Care Med.* **42,** E88–E88 (2014).

241. Choi, S. W. *et al.* Rapid in vivo detection of isoniazid-sensitive Mycobacterium tuberculosis by breath test. *Nat. Commun.* **5,** 4989 (2014).

242. Li, H. *et al.* Synthesis of Monodisperse, Quasi-Spherical Silver Nanoparticles with Sizes Defined by the Nature of Silver Precursors. *Langmuir* **30,** 2498–2504 (2014).

243. de Abajo, F. J. G. Multiple scattering of radiation in clusters of dielectrics. *Phys. Rev. B* **60,** 6086–6102 (1999).

244. de Abajo, F. J. G. & Howie, A. Retarded field calculation of electron energy loss in inhomogeneous dielectrics. *Phys. Rev. B* **65,** 115418 (2002).

245. Zavaleta, C. L. *et al.* Multiplexed imaging of surface enhanced Raman scattering nanotags in living mice using noninvasive Raman spectroscopy. *Proc. Natl. Acad. Sci. U. S. A.* **106,** 13511–13516 (2009).

246. Svedberg, F., Li, Z., Xu, H. & Kall, M. Creating hot nanoparticle pairs for surface-enhanced Raman spectroscopy through optical manipulation.

Nano Lett. **6,** 2639–2641 (2006).

247. Cang, H. *et al.* Probing the electromagnetic field of a 15-nanometre hotspot by single molecule imaging. *Nature* **469,** 385–388 (2011).

248. Liu, Z. *et al.* Revealing the molecular structure of single-molecule junctions in different conductance states by fishing-mode tip-enhanced Raman spectroscopy. *Nat. Commun.* **2,** 305 (2011).

249. Singhal, A., Haynes, C. A. & Hansen, C. L. Microfluidic Measurement of Antibody-Antigen Binding Kinetics from Low-Abundance Samples and Single Cells. *Anal. Chem.* **82,** 8671–8679 (2010).

250. Pfeiffer, C. *et al.* Interaction of colloidal nanoparticles with their local environment: the (ionic) nanoenvironment around nanoparticles is different from bulk and determines the physico-chemical properties of the nanoparticles. *J. R. Soc. Interface* **11,** 20130931 (2014).

251. Maiolo, D., Del Pino, P., Metrangolo, P., Parak, W. J. & Bombelli, F. B. Nanomedicine delivery: does protein corona route to the target or off road? *Nanomed.* **10,** 3231–3247 (2015).

252. Bunka, D. H. J. & Stockley, P. G. Aptamers come of age - at last. *Nat. Rev. Microbiol.* **4,** 588–596 (2006).

253. Tong, S. Y. C., Davis, J. S., Eichenberger, E., Holland, T. L. & Fowler, V. G. Staphylococcus aureus Infections: Epidemiology, Pathophysiology, Clinical Manifestations, and Management. *Clin. Microbiol. Rev.* **28,** 603–661 (2015).

254. Cao, X. *et al.* Combining use of a panel of ssDNA aptamers in the detection of Staphylococcus aureus. *Nucleic Acids Res.* **37,** 4621–4628 (2009).

255. Gordon, M. R. *et al.* Field Guide to Challenges and Opportunities in Antibody Drug Conjugates for Chemists. *Bioconjug. Chem.* **26,** 2198–2215 (2015).

256. Lee, J.-O. *et al.* Aptamers as molecular recognition elements for electrical nanobiosensors. *Anal. Bioanal. Chem.* **390,** 1023–1032 (2008).

List of Publications

- Mir-Simon, B., Reche-Perez, I., Guerrini, L., Pazos-Perez, N. & Alvarez-Puebla, R. A. Universal One-Pot and Scalable Synthesis of SERS Encoded Nanoparticles. *Chem. Mater.* **27,** 950–958 (2015).

- Mir-Simon, B., Morla-Folch, J., Gisbert-Quilis, P., Pazos-Perez, N., Xie, H., Bastus, N., Puntes, V. & Alvarez-Puebla, R.A. SERS efficiencies of micrometric polystyrene beads coated with gold and silver nanoparticles: the effect of nanoparticle size. *J. Opt.* **17,** 114012 (2015).

- Pazos-Perez, N. Pazos, E., Catala, C., Mir-Simon, B., Gomez-de Pedro, S., Sagalés, J., Villanueva, C., Vila, J., Soriano, A., García de Abajo, F.J. & Alvarez-Puebla, R.A. Ultrasensitive multiplex optical quantification of bacteria in large samples of biofluids. *Sci. Rep.* **6,** 29014 (2016).

- Catala, C., Mir-Simon, B., Feng, X., Cardozo, C., Pazos-Perez, N., Pazos, E., Gómez-de Pedro, S., Guerrini, L., Soriano, A., Vila, J., Marco, F., García-Rico, E. & Alvarez-Puebla, R. A. Online SERS quantification of Staphylococcus aureus and the application to diagnostics in human fluids. *Adv. Mater. Tech.* **1**, 1600163 (2016).